Frequency preference and reliability of signal integration: the role of intrinsic conductances

D I S S E R T A T I O N

zur Erlangung des akademischen Grades
doctor rerum naturalium
(dr. rer. nat.)
im Fach Biophysik

eingereicht an der
Mathematisch-Naturwissenschaftlichen Fakultät I
Humboldt-Universität zu Berlin

von
Frau Dipl.-Biophys. Susanne Schreiber
geboren am 26.02.1976 in Königs Wusterhausen

Präsident der Humboldt-Universität zu Berlin:
Prof. Dr. Jürgen Mlynek

Dekan der Mathematisch-Naturwissenschaftlichen Fakultät I:
Prof. Thomas Buckhout, PhD

Gutachter:

1. Prof. Dr. Andreas V. M. Herz
2. Prof. Dr. Uwe Heinemann
3. Prof. Dr. Thomas Höfer

eingereicht am: 14. Mai 2004
Tag der mündlichen Prüfung: 07. Juli 2004

Acknowledgments

Many people have influenced my thinking during my PhD, the more so, because the work was done in two different places, the Institute of Theoretical Biology at the Humboldt-Universität zu Berlin (ITB) and The Salk Institute of Biological Studies in La Jolla, USA.

Foremost, I would like to warmly thank my advisor Andreas Herz for his continuous support and encouragement, as well as the the opportunity to combine the work in his group with an extended experience abroad. I am grateful that he was always open to my research interests and I have truly enjoyed the exciting research environment that he created at the institute.

I am also greatly indebted to Terry Sejnowski at the Salk Institute. He let me join his group and provided an inspiring research environment, where I could profit from the rich scientific life and the expertise in temporal coding in particular.

The value of a theoretical work multiplies, if the results can be confirmed in experiments. It has been a pleasure to work with Irina Erchova at the ITB and Jean-Marc Fellous at The Salk Institute. They performed the experimental work presented in this thesis, but also discussed many other aspects of the thesis with me.

I am extremely happy that I was given the chance to work with Inés Samengo (ITB) and Paul Tiesinga (The Salk Institute), with whom I had many stimulating discussions about the theoretical part of this work. With Inés, in particular, I enjoyed a lively scientific exchange in a warm and personal working atmosphere. Tim Gollisch did not only contribute to this atmosphere, but he also proved a steady source of knowledge, from which I benefited many times.

I have been inspired by many other people at the ITB and I would especially like to thank Roberto Fernández Galán, Richard Kempter, Christian Leibold, Hartmut Schütze, and Martin Stemmler who always had time for my questions and interesting discussions. Jan Benda and Uwe Heinemann provided fruitful feedback on the subthreshold resonance project.

Of the people at the Salk Institute, I will gladly remember Tom Albright and Margaret Mitchell (the good spirit of the Sloan center), who supported me throughout my stay, as well as Jutta Kretzberg, Martina Wicklein, Rachel Kalmar, and Alex Koulakov with whom I shared many scientific discussions and many happy hours. I am also grateful to Arthur Houweling who helped me with the programming in NEURON and who shared his views on spike timing reliability with me.

I have enjoyed working with two students, Wiebke Krambeck (ITB) and Diane Whitmer (The Salk Institute), whose projects have inspired my work. Raphael Ritz I would like to thank for helpful comments on the thesis, but also for his constant readiness to transport my luggage across the Atlantic (in both directions!). My special thanks go to Arndt Telschow and Sabine Becker-Weimann for relaxing tea times as well as to all the other people who helped create
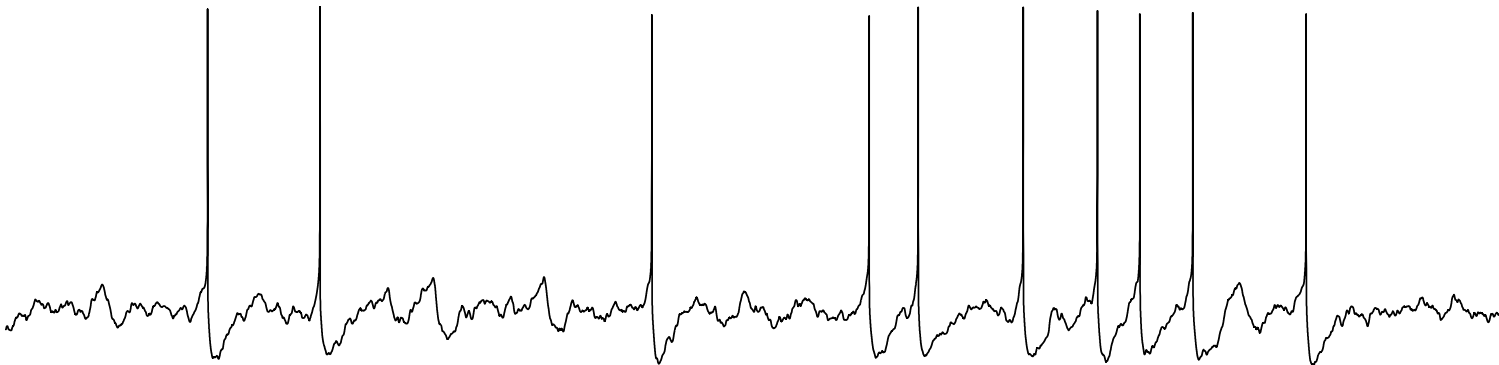
the friendly and welcoming atmosphere in both institutes!

Susanne Schreiber
Berlin, May 2004

"Men ought to know that from the human brain and from the brain only arise our pleasures, joys, laughter, and jests as well as our sorrows, pains, griefs and tears ... With it we think and understand, see and hear and we discriminate between the ugly and the beautiful, between what is pleasant and what is unpleasant and between good and evil."

Hippocrates (460 – 377 B.C.)

Contents

Chapter 1

Introduction

1.1 Overture

As the last measures of the winter music in Vivaldi's "Four Seasons" trail away in the beaming lights of the festive concert hall, a few moments of almost contemplative silence ensue, whereupon the euphoric audience greets the violinist and the orchestra with tremendous applause. Within a couple of seconds the applause transforms into waves of synchronous rhythmic clapping, as a sign of utmost appreciation, punctuated by occasional bravos and the audience rising to its feet.

Whether it was a classical concert, a soccer match, or the stirring speech of a beloved political party leader that roused our emotions – a perfectly synchronous, rhythmic response in light of a wonderful performance is far from innate. Take, for example, a group of small children, perhaps in the audience of a puppet show in the nursery rather than in a classical concert, and it is immediately obvious that we cannot expect the same reaction. Although they may appreciate the performance as much as the adults did the concert, their expression of pleasure will be reflected in their laughter and the overall movement and noise, but not in synchronized clapping. While some among them may try clapping, too, it is not easy to maintain a rhythm of a specific frequency that matches that of the others.

1.2 From the rhythms in the brain ...

Synchronous applause in concert halls bears many similarities to processes that commonly take place in our brain. Networks of neurons "clap" in unison – they fire synchronous action potentials – and hence produce rhythms detectable as a sum of electric potentials of thousands of neurons in electro-encephalographic (EEG) recordings. The frequency and amplitude of these rhythms are characteristic of localized brain regions, but also vary in time. Thus rhythms in awake and attentive states (such as in the beta and gamma frequency band of 20–80 Hz) are different from the rhythms appearing during sleep (as for example delta waves of 1–4 Hz). Some rhythms also depend on our behavior, such as alpha rhythms (8–12 Hz) in the occipital cortex, which appear during aroused states and diminish with eyes opened (Berger, 1929), or the theta rhythm in the hippocampus, which has been associated with explorative behavior (Vanderwolf, 1969; O'Keefe and Nadel, 1978).

The achievement of synchrony of thousands of neurons is a complex phenomenon[1], and depends on many factors, such as the network architecture and the synaptic strength of the connections. Analogous to the clapping after a performance, however, synchronous electrical activity in the brain also relies on special abilities of the individual neuron, regardless how trivial these abilities may seem in view of the relatively small efforts required by an adult in order to join the synchronous clapping. From the point of view of a single neuron, the ability to maintain synchronous firing is strongly influenced by the ability to phase-lock its response to the input – an ability, which the small children in the clapping analogy do not have acquired yet.

1.3   ... to reliability and frequency selectivity

While the synchronous firing of networks of neurons is not analyzed explicitly in the thesis at hand, the topics discussed herein bear importance for the emergence of rhythms because they focus on two closely related aspects on the level of individual neurons: the spike timing reliability[2] and the frequency selectivity of signal integration. The first reflects the ability of an individual neuron to couple to its input, the second relates to the ability of a neuron to participate in a rhythm of distinct frequency content. Our approach is two-fold and seeks to emphasize the role of intrinsic neuronal properties:

- First, we identify the fundamental cell-intrinsic mechanisms that determine spike timing reliability and frequency selectivity.

- Second, we aim at understanding how properties of individual neurons, specifically their ionic conductances, can serve to modulate these mechanisms in order to optimize signal integration.

We find that in order to elucidate the mechanisms underlying spike timing reliability and frequency selectivity, two distinct operating modes have to be distinguished. These depend on the mean level of depolarization and thus separate a regime of a stimulus mean below threshold from a regime of a stimulus mean above threshold. In both regimes, spike timing reliability is tightly connected to frequency selectivity. Specific ionic conductances can adjust the frequency selectivity and thus also determine spike timing reliability. Intriguingly, they can also directly influence spike timing reliability through an additional effect – the modification of a cell's sensitivity to noise. The latter arises from cell-intrinsic or cell-extrinsic sources and usually tends to compromise reliability. Our findings suggest an important role for dynamic neuromodulation of ion channels with regard to signal integration within individual cells and within neural networks.

---

[1]So is clapping, as a study published recently shows (Néda et al., 2000).

[2]Spike timing reliability as considered here is characterized by both the probability of the occurrence of spikes as well as their temporal precision. In principle, the terms spike reliability and reproducibility of neural responses could have been equally used in this thesis.

1.4   Overview

Before we begin the exploration of signal integration in individual neurons, let us briefly look at the structure of this work. Chapter 2 lays the foundations for the fundamental concepts, embracing the functioning of ion channels, the effect of subthreshold resonance, and spike timing reliability. The subsequent chapters are arranged according to the mean level of neuronal depolarization. In other words, when progressing from one chapter to the next, we will move gradually from the subthreshold nonspiking regime towards the suprathreshold spiking regime.

Chapter 3 starts out with the analysis of frequency selectivity for inputs resulting in graded nonspiking responses. The influence of subthreshold resonances on the integration of signals in cells of the entorhinal cortex is investigated. Here, we will examine whether the integration of periodic and nonperiodic inputs is governed by the same mechanism.

In chapter 4 we begin the analysis of spike timing reliability, for stimuli with subthreshold mean, which is extended in chapter 5 for stimuli with a mean above firing threshold. In these chapters the topics of spike timing reliability and frequency selectivity overlap. Chapter 4 elucidates the mechanism that leads to frequency preference of spike reliability and establishes a connection to the mechanism of subthreshold resonance. Chapter 5 reviews the resonance mechanism of spike timing reliability described previously and focusses on the influence of ionic conductances on the tuning of frequency preference. Chapter 6 discusses the results obtained for both sub- and suprathreshold regimes.

Chapter 7 is also devoted to the analysis of spike timing reliability for stimuli of suprathreshold mean. Here, the influence of the ion channels on the sensitivity to noise beyond frequency preference is presented.

Last but not least, Chapter 8 provides a summary and discussion of the results, as well as an outline of future research directions. The Appendices A to D contain additional material concerning the measure of spike timing reliability as well as all technical modeling details, which have been excluded from the main text for the purpose of readability.

Chapter 2

General concepts

To start the investigation of frequency selectivity and spike timing reliability in single neurons, we first need to acquaint ourselves with some of the fundamental concepts. This chapter therefore covers in large steps three different topics, including frequency selectivity and the reliability of spiking responses. We begin with a brief look at the functioning and modeling of ion channels.

> *"Ion channels are macromolecular pores in cell membranes. When they evolved and what role they may have played in the earliest forms of life we still do not know, but today ion channels are most obvious as the fundamental excitable elements in the membranes of excitable cells."*
>
> *Bertil Hille, 2001*

2.1   Ion channels

Ion channels are ubiquitous in nature. They are integral components of the most complicated and the most simple nervous systems, but can also be found in plants and bacteria. Hundreds of ion channels exist, they come in various shapes and flavors, though many of them share similar structural principles.

2.1.1   A multitude of ion channels

For the generation of efficient neural signals, such as *graded* changes in membrane potential as well as *action potentials* or *spikes*, in principle two voltage-gated ion channel types are sufficient: sodium and potassium. Evolution chose, however, to create many different and highly specific types of ion channels. Thus we can find today channels differing in principal carrier, voltage dependence, time scale of activation and potentially inactivation, dependence on internal calcium, as well as a vast zoo of regulatory mechanisms including neuromodulators and

cell-intrinsic messengers. The operation of ion channels is costly[1], in addition, their composition changes constantly and is highly regulated. The intrinsic membrane currents determined by the properties of ion channels have been found to contribute to electrical responses and to memory mechanisms in an activity-dependent way (Turrigiano et al., 1994; Marder et al., 1996; Goldman et al., 2001; Destexhe and Sejnowski, 2003). To elucidate the role of individual ionic conductances for specific areas of signal integration is one of the major aims of this thesis.

Ion channels function by stochastic opening and closing of a transmembrane pore to selected ions. The macroscopically measured currents arise from populations of individual ion channels. The macroscopic behavior can be captured on the basis of kinetic models that characterize transitions between conformational states. The first quantitative description of signal integration with ion channels is a cornerstone of modern neurobiology – the model of action potential initiation by Hodgkin and Huxley (1952). Derived for the squid giant axon, it still forms the basis for the most commonly used characterization today: conductance-based models. To date, many ion channels of the nervous system have been characterized in great detail. To a good approximation, most of them can be modeled according to the principles introduced by Hodgkin and Huxley.

Also in the present work, conductance-based model neurons form the basis of theoretical investigation. Therefore, we will briefly review the basic principles underlying these models. For a more detailed description we refer the reader to standard textbooks, such as (Koch, 1999; Kandel et al., 2000).

2.1.2   The principles underlying conductance-based neuron models

The generation of voltage responses involves changes in ionic conductance. In the example of the classical Hodgkin-Huxley model, two major voltage-dependent channels are responsible for the generation of action potentials: sodium (Na) and potassium (K). In addition, a small conductance that does not depend on voltage – the so-called leak conductance (L) – is present. Although the cells used in this study are equipped with a number of additional channels, the Hodgkin-Huxley channels are representative for the functioning of conductance-based model cells. These follow a few general principles:

(1) The net current flowing across the membrane is zero, so that the current-balance equation holds:

$$C_{\mathrm{m}}\frac{dV}{dt} \quad = \quad -I_{\mathrm{Na}} - I_{\mathrm{K}} - I_{\mathrm{L}} + I_{\mathrm{ext}}, \tag{2.1}$$

where V denotes the potential across the membrane, C_{m} the membrane capacitance, and I_{Na}, I_{K}, and I_{L} the corresponding ionic currents. I_{ext} characterizes the external current (either a synaptic current or the current injected via an electrode). The input to conductance-based model cells is presented via I_{ext}.

---

[1]Interestingly, the largest cost does not arise from the maintenance of the channels themselves, but from the active pumping of ions that passed the channels in order to stabilize the ionic concentration gradients (Attwell and Laughlin, 2001).

(2) In the model, ionic currents are linearly related to the time- and voltage-dependent ionic conductances (g_{Na}, g_{K}, and g_{L}) and the difference between voltage and reversal potentials (E_{Na}, E_{K}, and E_{L}):

$$C_{\mathrm{m}}\frac{dV}{dt} = -g_{\mathrm{Na}}(V - E_{\mathrm{Na}}) - g_{\mathrm{K}}(V - E_{\mathrm{K}}) - g_{\mathrm{L}}(V - E_{\mathrm{L}}) + I_{\mathrm{ext}}. \tag{2.2}$$

The reversal potential for each ion type can be derived from Nernst's equation and is assumed to be constant. The latter approximation is usually valid if large fluctuations of ionic concentrations on either side of the membrane can be excluded.

(3) Ionic conductances depend on the conformational state of the ion channels. The conductances can be expressed as the product of a peak conductance and the fraction of open channels.[2] The fraction of open channels in turn depends on the state of so-called activation and inactivation gating particles, which all have to be in the correct state to permit ion flow. Each ion channel may have several independent gating particles, whose open probability multiply to give the fraction of open channels. In the case of the classical Hodgkin-Huxley Na channel three activation particles and one inactivating particle are assumed, with open probabilities denoted as m and h, respectively. Thus the sodium conductance, g_{Na} equals

$$g_{\mathrm{Na}} = \bar{g}_{\mathrm{Na}}m^3 h. \tag{2.3}$$

(4) The transition of gating particles from the open to the closed state is governed by a kinetic reaction scheme, such as

$$m \underset{\beta_m}{\overset{\alpha_m}{\rightleftharpoons}} 1 - m, \tag{2.4}$$

which mathematically corresponds to a first order differential equation with the voltage-dependent transition constants $\alpha_m(V)$ and $\beta_m(V)$:

$$\frac{dm}{dt} = \alpha_m(V)(1 - m) - \beta_m(V)m. \tag{2.5}$$

An equivalent but more common way to express the gating kinetics, exemplified for the activation particle of the Na channel, is the following:

$$\tau_m(V)\frac{dm}{dt} = m_\infty(V) - m, \tag{2.6}$$

where $\tau_m = 1/(\alpha_m(V) + \beta_m(V))$ specifies the voltage-dependent time constant and $m_\infty = \alpha_m/(\alpha_m + \beta_m)$ the voltage-dependent steady state value of a gating process. In contrast to the steady state values, the time constants depend on the absolute size of the transition rates α_m and β_m. Thus time constants change, for example, with temperature.

---

[2] Usually, only the value of the peak conductance is specified. It is derived from the total number of ion channels of a given type and the single-channel conductance.

Altogether, the original Hodgkin-Huxley equations represent a nonlinear system of four differential equations, where the kinetics of three types of gating particles (m, h, and a variable n for potassium) are coupled to the voltage, V. In general, the full solution of such a system can only be achieved numerically.

While the equations 2.1, 2.2, and 2.6 form the core of all conductance-based models, simplifications are possible depending on the characteristics of ion channel types. In the following, some ion channels are used in their full description, such as for example the Na channel. Other channels are described by only one gating particle, such as the muscarinic potassium channel, M. The slow potassium channel, $\mathrm{K_s}$, relies on a simplified kinetic scheme where the voltage-dependence of the time constant is approximated by a constant value, τ_{Ks}. The simplicity of the $\mathrm{K_s}$ channel, for example, has the advantage to represent a more general class of noninactivating potassium channels, here used with kinetics slower than the action potential time scale. Ligand-gated ion channels can also be incorporated according to the principles described above. For them, the concentration of the ligand has to be included as a variable in the system of differential equations, usually assuming first-order kinetics.

Throughout this work, one-compartmental conductance-based model neurons on the basis of Hodgkin-Huxley type sodium conductances (Na), delayed rectifier potassium conductances ($\mathrm{K_{dr}}$), and leak conductances (L), are employed. The model cells can also contain a persistent sodium conductance, $\mathrm{Na_P}$, an H conductance, and one of three slow potassium conductances ($\mathrm{K_s}$, M, and $\mathrm{K_{ca}}$). The presence of the ionic conductances is discussed in the corresponding chapters, a complete overview is given in Appendix B. In addition to these conductance-based model neurons, a reduced two-dimensional system introduced by Morris and Lecar (1981) is analyzed (see Appendix C).

Having gathered the basic principles how ionic conductances determine the generation of voltage signals in neurons, we now turn to the first mechanism that leads to frequency selectivity: subthreshold resonance.

2.2   Subthreshold resonance

Subthreshold resonance is a phenomenon observed for graded (nonspiking) responses. Properties of the membrane determine the amplitude of subthreshold responses to sine wave stimuli in a frequency-dependent way. Many cells exhibit low-pass-filter characteristics, i.e. the response amplitude is largest for constant (0 Hz) stimuli and falls off with increasing frequency. A large number of cells, however, show a maximal response amplitude at non-zero frequencies. They exhibit a subthreshold resonance.

Subthreshold resonances have been described in a number of excitable cell types (Cole, 1968; Mauro et al., 1970; Nelson and Lux, 1970; Fishman et al., 1977; Gimbarzevsky et al., 1984; Moore and Christensen, 1985; Jansen and Karnup, 1994), including muscle cells (Falk and Fatt, 1964), cardiac cells (DeFelice, 1981), hair cells of the inner ear (Hudspeth and Lewis, 1988), cells of the hippocampus and amygdala (Leung and Yu, 1998; Pape and Driesang, 1998; Pike et al., 2000; Hu et al., 2002), in various cortices (Alonso and Llinás, 1989; Gutfreund et al., 1995; Hutcheon et al., 1996b; Schmitz et al., 1998; Haas and White, 2002), the thalamus

(Puil et al., 1994; Hutcheon et al., 1994), as well as olivary neurons (Lampl and Yarom, 1997).

2.2.1 Importance of subthreshold resonance

There is analytical and experimental evidence that the resonance properties play an important role in tuning neurons to inputs in particular frequency bands (Izhikevich, 2001; Haas and White, 2002; Richardson et al., 2003). Resonance may thus provide a key mechanism to establish a frequency-dependent information flow between cortical areas (Chrobak and Buzsaki, 1998; Gloveli et al., 1997; Dickson et al., 2000b). For example, cells in the entorhinal cortex that provide input to the hippocampus show a pronounced subthreshold resonance in the same frequency band as the theta rhythm, an electroencephalographic (EEG) rhythm in the hippocampal region associated with conditions like active exploration (Alonso and Klink, 1993; Bland and Colom, 1993; Hasselmo et al., 2000). The resonance may enable these cells to directly contribute to the theta rhythm, it may, on the other hand, also promote synchrony (Hutcheon and Yarom, 2000) of such neurons if coupled in a network. A closer look at the influence of subthreshold resonance on signal integration in these cells will be taken in Chapter 3. In addition, subthreshold resonance is associated with the occurrence of intrinsic subthreshold oscillations of the membrane potential, see for example (Richardson et al., 2003; Erchova et al., 2004). These oscillations, however, are not investigated in this work.

2.2.2 Measurement of subthreshold resonance

It is common to use one of two ways to measure subthreshold resonance: either by analysis of the response amplitude or by quantification in terms of the electrical impedance. In the first case, response amplitudes are directly obtained by stimulation with sine waves of different frequencies. One stimulus per frequency has to be utilized. In the second case, often so-called ZAP (impedance(Z)-Amplitude-Profile) stimuli are employed. These are sine waves with time-dependent frequencies, for example with a linear increase in frequency as used throughout this work: $I_{\mathrm{ZAP}}(t) = I_0 \sin[2\pi f(t)t]$, with $f(t) = f_m t/2T$. I_0 represents the amplitude of the ZAP stimulus, f_m is the maximum frequency, and T the stimulus length. An example of a ZAP stimulus with frequencies increasing from 0 to 20 Hz is shown in Fig. 2.1A.

Testing a whole range of frequencies within one stimulus presentation, these types of stimuli allow a more efficient characterization of subthreshold resonance. With varying frequency also the "local" response amplitudes vary and thus reflect frequency-selectivity, as can be seen in Fig. 2.1B. The frequency-dependent electrical impedance is obtained as the Fourier transform of the time-dependent response to a ZAP input divided by the Fourier transform of the ZAP current, $Z(f) = FFT[V_{\mathrm{ZAP}}(t)]/FFT[I_{\mathrm{ZAP}}(t)]$ (Gimbarzevsky et al., 1984; Puil et al., 1986; Puil et al., 1988). Fig. 2.1C shows the impedance corresponding to the stimulus and response shown in panels A and B. In order to avoid large transient responses due to fast changes in the stimulus frequency, ZAP currents usually extend over several tens of seconds. For an increase from 0 to 20 Hz we use a duration of 30 seconds throughout this thesis. It was checked that ZAP currents of double and half duration gave similar estimates for the investigated neurons and model cells.
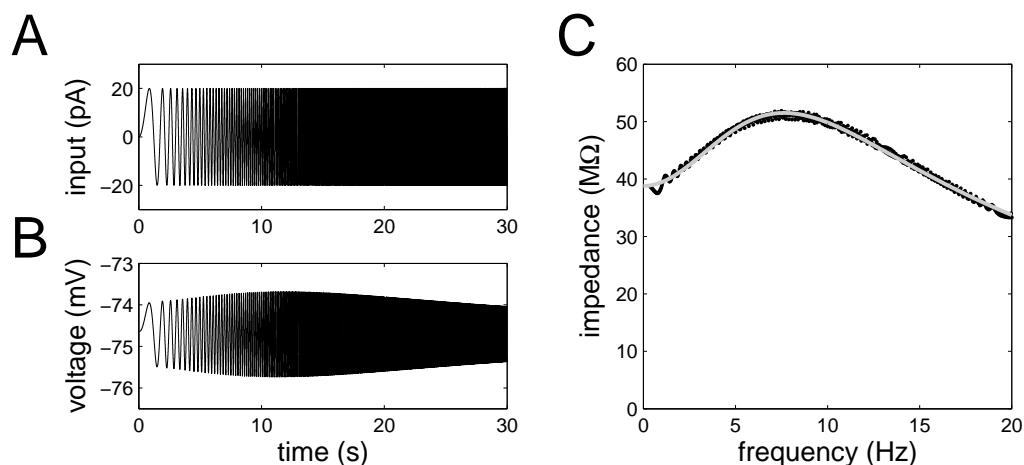
Figure 2.1:   Measurement of subthreshold resonance. **A** *A ZAP stimulus with a linear increase in frequency from 0 to 20 Hz. For frequencies larger than 5 Hz the variation in the stimulus cannot be resolved graphically in this representation.* **B** *The response of a model cell to the stimulus in A. The "local" amplitudes depend on the stimulus frequency. The amplitudes are largest in between 10 and 15 seconds after stimulus onset.* **C** *The electrical impedance calculated on the basis of the stimulus and response shown in A and B (thin black line) and the corresponding fit with the electrical circuit model (thick gray line). The model cells shows a clear resonance at 7.5 Hz with a Q-value of 1.35.*

The resonance frequency is given by the frequency at the impedance peak. In the following, we denote a resonance frequency of 0 Hz if the impedance is monotonically decreasing and has a maximum at 0 Hz (although a cell with this profile would be called nonresonant). As an estimate of the strength of the resonance, the Q-value is given as the ratio of the impedance at the resonance frequency and the impedance at 0 Hz; the Q-value is larger than 1 for cells with subthreshold resonance and equals 1 for cells with low-pass-filter characteristics. As the presence of noise may lead to Q-values larger than 1 even for cells without subthreshold resonance, it is useful to raise the Q-value that separates resonant from nonresonant behavior in experiments to a slightly larger value, such as 1.2.

2.2.3   Fitting of impedance profiles

Impedance curves can be fitted with a two-dimensional electrical circuit model with four fit parameters, designed to account for the resonance properties of neuronal membranes. Electrical circuit models are equivalent to models of linearized voltage-dependent currents, as suggested by Mauro *et al.* (1970). Interpreted as an electrical circuit (see also Koch, 1999), the model consists of two parallel branches (Fig. 2.2). The first branch is characterized by a resistance (R_m) in parallel with a capacitance (C) and mimics the integrative properties of a leaky-integrator. The second branch consists of another resistance (R_L) in series with an inductance (L) and captures the response properties of a delayed rectifying current. Due to its simplicity, this model has been used in various mathematical investigations of subthreshold phenomena (Mauro et al., 1970; Hutcheon and Yarom, 2000; Izhikevich, 2001; Richardson et al., 2003;

Erchova et al., 2004).
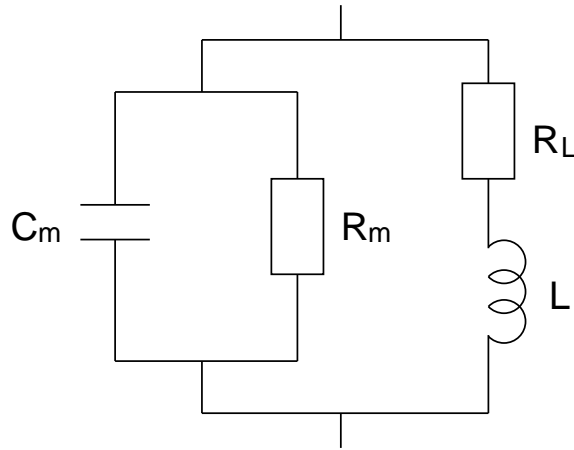
Figure 2.2: The electrical circuit model upon which the fit of the impedance curves is based.

2.2.4   How ion channels determine the resonance

Extensive investigation in the last decade has revealed many of the principles underlying sub-threshold resonance. It has been shown that resonance arises from the interplay between passive and active membrane properties. In order to shape a subthreshold resonance, mechanisms that lead to the attenuation of signals at high and low frequencies are needed, so that only signals in between can pass efficiently. For an extensive review of these mechanisms we refer the reader to Hutcheon and Yarom (2000).

Based on the results summarized in their review, we know how the combination of different ion channels can lead to subthreshold resonance: First, leak channels in the membrane and the membrane capacitance cause the attenuation of high-frequency responses. Second, voltage-gated ion channels act as high-pass filters, diminishing the responses to low frequencies. Not all voltage-gated ion channels are suitable, because ion channels leading to resonance must fulfill two conditions: (1) They have to oppose changes in membrane potential, such as do potassium channels or H channels. This includes all channels whose reversal potential falls near the base of their activation curve. (2) The channels must activate slowly relative to the membrane time constant to oppose slow changes in voltage and act as high-pass filters. Two of the most effective ion channel types are slow potassium channels and H channels with time constants on the order of several tens of ms. Slow potassium channels mainly activate with depolarization and counteract depolarizing changes in membrane potential. H channels activate upon hyperpolarization and oppose hyperpolarizing changes in membrane potential (see also Fig. 2.4). In addition, other conductances, such as the noninactivating persistent sodium conductance, can help to amplify the resonance (Gutfreund et al., 1995; Hutcheon and Yarom, 2000).

2.2.5 Slow potassium and H channels are major players

Indeed, both slow potassium channels as well as H channels can produce subthreshold resonance, as impedance curves measured for three conductance-based model neurons confirm. The neurons are equipped with Na, K_{dr}, L, and Na_P channels, in addition they also contain different amounts of muscarinic potassium channels, M, and, H channels. No noise is present. Without M and H channels, the neurons show low-pass-filter impedance profiles (data not shown). If H or M are present, however, subthreshold resonances can be found:
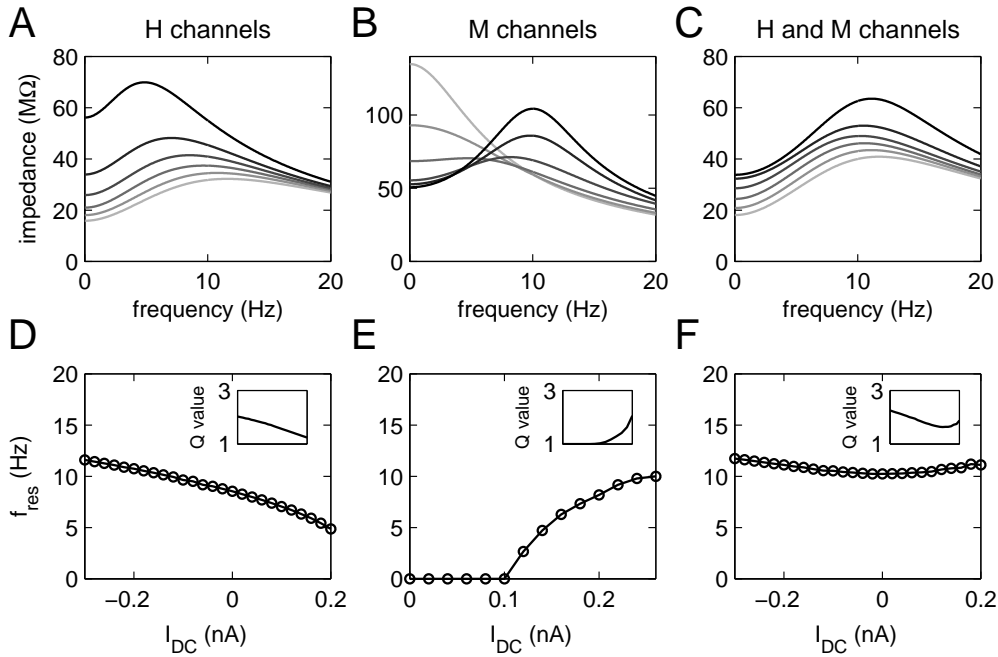
Figure 2.3: Influence of H and M channels on subthreshold resonance. **A** Impedance curves at different DC levels (-0.3 nA to +0.2 nA in steps of 0.1 nA, light to dark curves) for a cell with H channels (g_H=0.2 mS/cm^2). **B** Impedance curves for a cell with M channels g_M=0.4 mS/cm^2 (at DC levels 0.02, 0.08, 0.14, 0.2, 0.24, and 0.26 nA, light to dark curves). **C** Impedance curves for a cell with both, H and M, channels (g_H=0.2 mS/cm^2, g_M=0.4 mS/cm^2) at different DC levels (-0.3 nA to +0.2 nA in steps of 0.1 nA, light to dark curves). **D-F** Resonance frequency and Q-value (in the insets) as a function of the DC level for the three cells shown in the panels above. The range of I_{DC} values on the x-axis corresponds to voltages from -73 to -61 mV (D and F) and -81 to -60 mV (E). The combination of H and M channels can stabilize the resonance frequency over a broad range of DC levels.

With H channels: Subthreshold resonance is observed. Resonance frequency and Q-value depend on the level of the membrane potential (determined by the DC component of the stimulus). Fig. 2.3A shows the impedance profile for various levels of membrane potential. The darker the curves, the larger the DC and consequently the larger the membrane potential. For hyperpolarized membrane potentials (lighter curves) the resonance is strong with Q-values

around 2 and a resonance frequency around 12 Hz (Fig. 2.3D). With increasing depolarization (darker curves Fig. 2.3A) the overall impedance values rise, however, the resonance weakens, as is reflected in a decreasing Q-value, and the resonance frequency decreases.

The reason for the dependence of the resonance on the DC level is the voltage-dependence of the H activation curve. H is mainly activated in the hyperpolarizing regime, see Fig. 2.4, characterized by a half activation voltage of -82 mV in the model. The H conductance is less active in more depolarized regimes, which shows in the impedance curve.
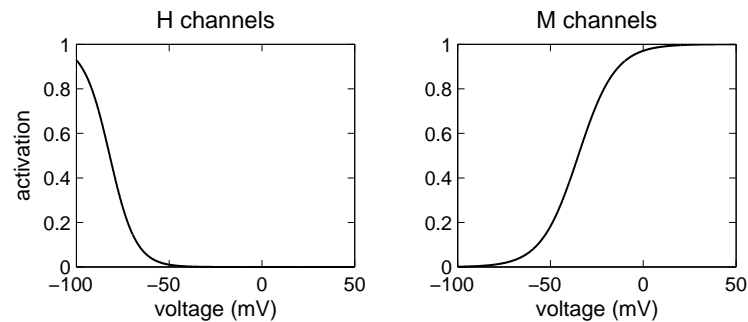
Figure 2.4: Steady state activation of H and M model channels as a function of voltage. An activation value of 1 characterizes a state where all channels are open.

With M channels: M channels are activated at depolarized levels of membrane potential (Fig. 2.4). The half activation voltage in the model is -35 mV. Thus cells that do not contain H channels, but a significant M conductance exhibit no resonance at hyperpolarized levels of membrane potential (lighter curves in Fig. 2.3B), but a pronounced resonance closer to threshold (darker curves). Resonance frequency and Q-value increase towards threshold, as Fig. 2.3E indicates.

Characteristic of both cells above (with H and with M) is a strong dependence of the resonance frequency on the DC. For some cell types, as for examples stellate cells in layer II of the entorhinal cortex and CA1 pyramidal cells in hippocampus, however, the resonance frequency is relatively stable over a wide range of membrane potentials (Erchova et al., 2004). We hypothesize that for stabilization of the resonance frequency over a broad range of membrane potentials several resonating currents with activation ranges at different voltages (such as H and M) have to be combined:

With H and M channels: Resonances caused by each channel type complement one another and the two peak conductances of both channels can even be tuned to result in a resonance whose frequency is independent of the DC (Fig. 2.3C and 2.3F). Although the absolute values of impedance increase with DC, the overall shape of the resonance is similar and the resonance frequency is relatively stable. In the case of the CA1 hippocampal pyramidal cells both, H and M currents, have been shown to be involved in the res-

onance (Hu et al., 2002). For entorhinal stellate cells, which will be discussed in more detail in Chapter 3, the presence of H currents has been proven (Dickson et al., 2000a; Richter et al., 2000), and there is indirect evidence in support of the presence of M currents, because they are affected by retigabine (Hetka et al., 1999). The latter was recently shown to act on muscarinic potassium channels (Rundfeldt and Netzer, 2000; Main et al., 2000). In addition, subunits of muscarinic potassium channels (in the KCNQ family) have been found to be expressed in layer II of the entorhinal cortex (Saganich et al., 2001).

2.2.6 Neuron type and subthreshold resonance

When discussing subthreshold resonance, it should be mentioned that for two-dimensional neuron models it is possible to establish a relation between the existence of a subthreshold resonance at threshold and two types of neuronal dynamic, the so-called type I and type II dynamics. This relation will be discussed in Chapter 6. The different dynamics are reflected in different basic properties of neuronal signal integration. It has been known for long, see for example (Hodgkin, 1948), that neurons can be classified either as one type or the other according to their responses to constant currents. Accordingly, one obvious difference between the two types is the firing rate in response to constant stimuli directly above threshold. While type I neurons can exhibit arbitrarily low firing rates, type II neurons have a minimum firing rate distinct from zero (Fig. 2.5). In case of the classical Hodgkin-Huxley model this onset firing rate is on the order of 50 Hz. The reason for the different behavior of these neuron types is the type of bifurcation that occurs at the threshold. Either the fixed point (i.e. the steady state voltage) in the subthreshold regime loses stability in a saddle-node bifurcation (type I) or in a Hopf bifurcation (type II), see for example (Hansel et al., 1995; Ermentrout, 1996; Rinzel and Ermentrout, 1998). For further details on the bifurcation types we refer the reader to the literature on nonlinear dynamics, such as (Strogatz, 1994).
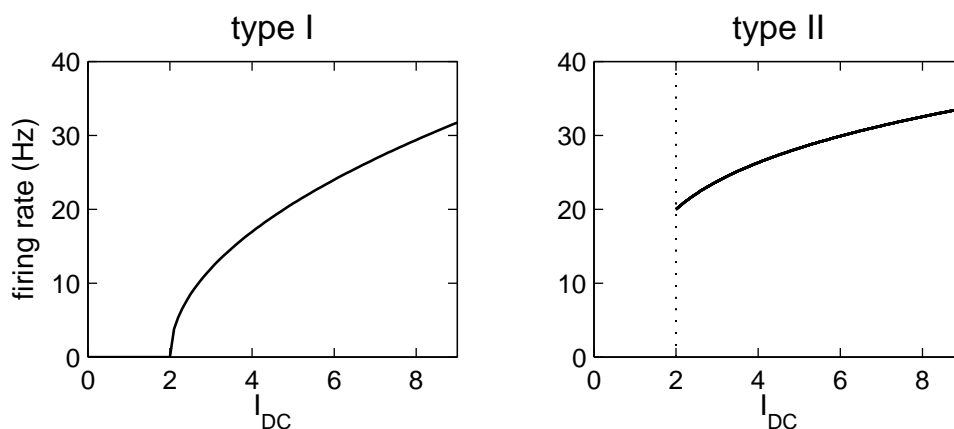

Figure 2.5: Schematic representation of the firing rate as a function of the input current, I_{DC}, for type I and type II dynamics. For type I the firing rate increases continuously, whereas for type II the firing rate jumps to large values directly at threshold.

In general, the effects of subthreshold resonance are not limited to subthreshold responses, they can also influence the generation of spiking responses. The analysis of the relation between subthreshold resonance and the firing rate of spikes as well as spike timing reliability plays a major role in Chapters 3 and 4. Therefore basic facts on spike timing reliability are introduced in the last section of this chapter.

2.3 Spike timing reliability

From what we know today, spikes constitute the inter-neuronal signals of choice in the central nervous system.[3] Because of the all-or-none nature of their generation, they are very robust and can transmit information efficiently over long distances (Attwell and Laughlin, 2001). Their fast onset allows to amplify fast transients and can thus sharpen the temporal structure of neuronal signals (Kretzberg et al., 2001).

2.3.1 Firing rate versus the timing of spikes

Spiking responses consist of a series of pulses in time. It is not straightforward to assign a unique decoding strategy to recover the information represented by a spike train (Rieke et al., 1997; Theunissen and Miller, 1995; Salinas and Abbott, 1994). The current research reflects a lively debate about the time window relevant for decoding: In one extreme, the neuronal firing rate, defined for example by the number of spikes averaged over a time window of several tens to hundreds of milliseconds, could contain all information (we also speak of a rate code). This view underlies many studies, in which neuronal responses are evaluated in terms of firing rate, see for example (Adrian, 1928; Britten et al., 1992; Shadlen and Newsome, 1994). In the other extreme, the very position of each individual spike in time could matter and code information about the signal (spike timing code). In principle, such a spike timing code can achieve higher rates of information transmission, because the exact position of spikes opens an additional coding dimension (Bair and Koch, 1996; Rieke et al., 1997).

The prerequisite for a timing-based code is the capability of neurons to reliably produce spikes with high temporal precision. To date, many studies have provided evidence for high reliability of the spike initiation process in various parts of nervous systems, comprising for example retina and LGN (Berry et al., 1997; Reich et al., 1997; Reinagel and Reid, 2000; Reinagel and Reid, 2002), the electrosensory system of electric fish (Kreiman et al., 2000), hippocampus and cortex (Mainen and Sejnowski, 1995; Fricker and Miles, 2001; Fellous et al., 2001; Maccaferri and Dingledine, 2002; Haas and White, 2002; Wehr and Zador, 2003; Axmacher and Miles, 2004), insect motion detection (de Ruyter van Steveninck et al., 1997; Warzecha et al., 1998), insect auditory receptors (Machens et al., 2001; Machens et al., 2003), locust olfaction (Wehr and Laurent, 1996), zebra finch forebrain (Chi and Margoliash, 2001), and various other sensory and cortical systems, for reviews see (Bair, 1999;

---

[3]It should be noted, however, that much of the signal processing happens in a graded signal regime, as for examples in the dendrites, and that direct graded signaling between cells through dendro-dendritic electrical synapses not involving spikes could play a more important role than currently believed.

Lestienne, 2001). Furthermore, highly synchronized states of many neurons have been observed in local field potential recordings and EEG, see for example (Buzsaki et al., 1983; Gray et al., 1989). Additional evidence for the important role of temporal precision is provided by the emerging rules of spike-timing-dependent plasticity, where the strengthening or weakening of synaptic connections is decided by a temporal difference of a few milliseconds in spike timing (Markram et al., 1997; Bi and Poo, 1998).

During the last years is has become increasingly evident that the exclusive alternative between a firing rate code and a temporal (spike timing) code is ill-phrased. It is more likely that – depending on the specific system and task – spikes can be read out at various time scales, opening a broad spectrum between a rather static firing rate and individual spike timing (Softky and Koch, 1993; Rieke et al., 1997; Koch, 1999; deCharmes and Zador, 2000). In addition, it is not only the time of individual spikes that matters, but information can also be carried by complex relationships between spikes, as for example by the inter-spike intervals or higher-order correlations in the spikes of groups of neurons (Abeles, 1991; Dayan and Abbott, 2001; Ikegaya et al., 2004). At the same time, situations where the individual timing of spikes matters have been confirmed experimentally, so that the ability of neurons to give phase-locked responses is of immediate interest for the understanding of the nervous system.

Consequently, the experimental studies have been accompanied by a multitude of theoretical investigations, trying to elucidate the reliability of spike generation. Thus various aspects of spike timing reliability have been analyzed on the basis of integrate-and-fire models, conductance-based model neurons, and stochastic models, as for example in (Pei et al., 1996; Schneidman et al., 1998; Hunter et al., 1998; Cecchi et al., 2000; Beierholm et al., 2001; Van Rossum, 2001; Tiesinga, 2002; Tiesinga et al., 2002; Manwani et al., 2002; Brette and Guigon, 2003; Hunter and Milton, 2003; Gutkin et al., 2003; Svirskis and Rinzel, 2003). Both experimental and theoretical analysis rely on the definition of a measure of spike timing reliability. In the following, we introduce a correlation-based approach.

2.3.2   The correlation measure of spike timing reliability

A timing-based code could be achieved by reproducible neuronal responses that readily phase-lock to the stimulus. Individual neurons, however, are subject to intrinsic and extrinsic noise, as caused by the stochastic nature of channel opening, or by synaptic noise due to external stimulus-uncorrelated inputs. For a review of the individual noise sources see for example (Manwani and Koch, 1999). The presence of noise decreases the reproducibility of responses to identical stimuli, it lowers the reliability.

Reduced reproducibility manifests itself in two ways. First, the number of spikes in response to a stimulus can be variable - spikes are missing or additional spikes occur. Second, temporal jitter in the timing of individual spikes is observed. Fig. 2.6 illustrates an input to a model cell and 20 responses to the same stimulus in the presence of noise. Obviously both, variation in spike number (mainly missing spikes) and timing jitter occur and thus decrease reliability.

How can spike timing reliability be quantified? Although a multitude of different measures have been used for the analysis of spike timing reliability, we introduce a simple correlation-

stimulus:

responses:
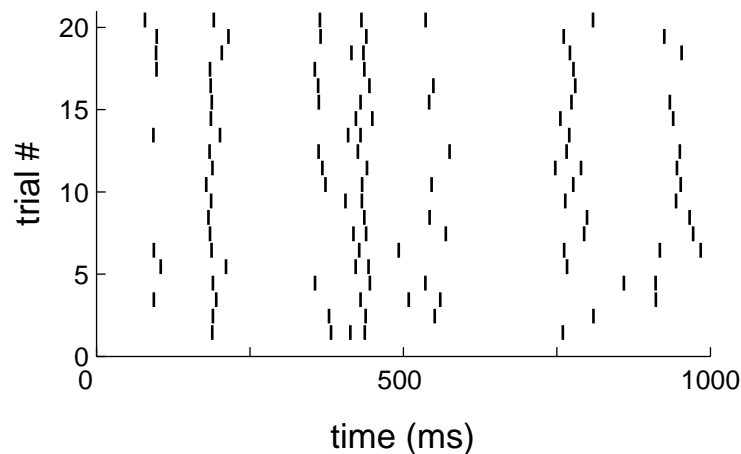
Figure 2.6: Spike timing reliability. **A** *A noise stimulus and 20 spike trains elicited in responses to repeated presentation of this particular stimulus (with a different realization of intrinsic neuronal noise for each stimulation). The data are obtained from a conductance-based model cell. Reliability can be decreased because of missing and additional spikes (as for the spikes around 500 ms) or because of timing jitter (as for example at 200 ms).*

based approach, that captures both sources of unreliability. In contrast to many other measures, it relies on the structure of individual responses and does not require the definition of *a posteriori* events. It also offers the advantage that it has only a single, intuitive parameter, that determines the influence that timing jitter has compared to missing or additional spikes. The measure will be applied to both experimental and modeling data. For a comparison of this measure to histogram-based measures see Appendix A.

Practically, spike trains have to be obtained from N repeated presentations of the same stimulus. They are convolved with a Gaussian of standard deviation σ_t (the only parameter of the measure, also referred to as filter width) resulting in filtered spike trains, which we denote $\vec{s_i}$ for notational simplicity ($i = 1, ..., N$). The convolution smoothes the spikes and allows for temporal overlap between spikes in different responses. The allowed temporal jitter is thus directly determined by the parameter σ_t. Smoothed spike trains are pairwise correlated (Fig. 2.7) and the normalized value of this correlation is averaged over all combinations of

pairs. The correlation measure, R, is therefore given by

$$R = \frac{2}{N(N-1)} \sum_{i=1}^{N} \sum_{j=i+1}^{N} \frac{\vec{s}_i \cdot \vec{s}_j}{|\vec{s}_i||\vec{s}_j|}.$$

The normalization guarantees that $R \in [0; 1]$. $R{=}1$ indicates highest reliability (when all spike trains are identical) and $R{=}0$ lowest. For most model cells studied, σ_t equals 1.8 ms; exceptions and values of σ_t for experimental data are indicated in the text. Generally, the value of the filter width σ_t is chosen such that, given the noise level, reliability values exploit the possible range of values [0;1], allowing for better discrimination between reliable and unreliable spike timing. All evaluation of model and experimental data (beyond obtaining spike times) has been performed in Matlab.
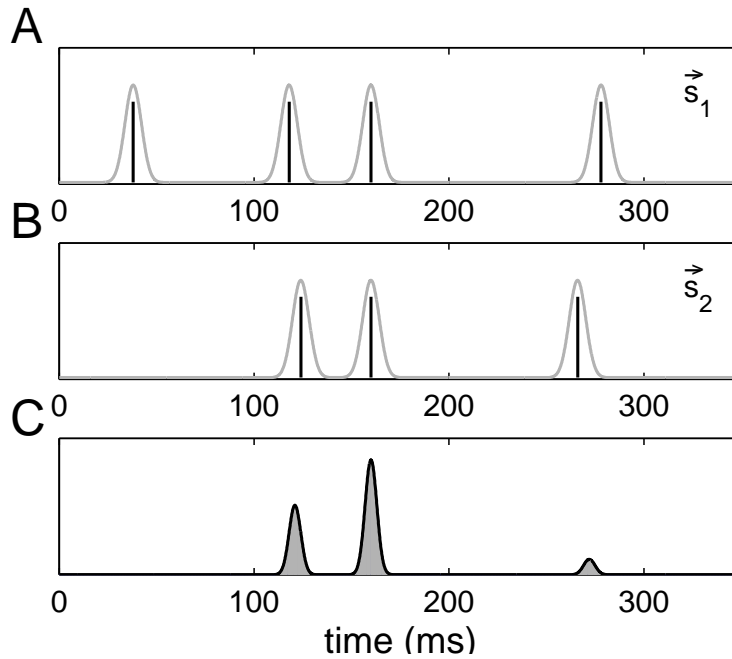
Figure 2.7: Illustration of the correlation-based measure. **A** A raw spike train with four spikes (vertical black lines) and the same spike train filtered with a Gaussian (gray line, $\vec{s}_1$). **B** Another spike train and its smoothed version ($\vec{s}_2$) in response to the same stimulus. Obviously, the first spike is missing. The last spike shows a high temporal jitter. **C** The element-wise multiplication of the two spike trains in A and B. The gray area under the curve equals the scalar product $\vec{s}_1 \cdot \vec{s}_2$ and indicates the (unnormalized) contribution of this pair of spike trains to the reliability estimate, R. The missing first spike in $\vec{s}_2$ as well as the large temporal jitter between the last spike in $\vec{s}_1$ and $\vec{s}_2$ strongly reduce R.

2.3.3 Stimulus statistics

For the analysis of the mechanisms that set the reliability of responses three major aspects have to be taken into account.

First, intrinsic properties of a neuron play an important role. On the one hand intrinsic noise sources directly influence reliability (see, for example, Schneidman et al., 1998). On the other hand the intrinsic neuronal dynamics that shape the responses to a given input can also be expected to influence reliability (Fricker and Miles, 2000; Magee, 2002; Franz and Ronacher, 2002; Svirskis and Rinzel, 2003; Axmacher and Miles, 2004). Many questions, however, remain open: What are the mechanisms that would allow ion channels to influence reliability? Which ion channels are decisive? How do intrinsic properties interact with external properties?

Second, in addition to intrinsic mechanisms also extrinsic influences – the most obvious being external neuronal noise sources – determine spike timing reliability. The work of Hunter et al. (2003) shows for example an influence of additional synaptic input through modification of the neuronal firing rate. Others discuss the modification of timing precision due to well timed inhibitory or excitatory input (Mehta et al., 2002).

Third, features of the stimulus are as important as the intrinsic and extrinsic properties set by the nervous system. Thus a neuron may respond reliably to stimulus A, but unreliably to stimulus B. For spike timing the two most relevant stimulus properties are the variance and the frequency content. Mainen and Sejnowski were the first to show that reliability improves with larger stimulus variance. Many following studies have provided evidence that also the frequency content matters (Nowak et al., 1997; Hunter et al., 1998; Jensen, 1998; Fellous et al., 2001; Tiesinga, 2002; Haas and White, 2002; Hunter and Milton, 2003). While the mechanisms responsible for frequency selectivity of spike timing reliability have been described for some stimulus regimes, see for example (Hunter et al., 1998; Hunter and Milton, 2003), the picture is not yet complete. One major aim of this work is therefore to provide a systematic analysis of frequency preference of spike timing reliability.

As indicated, the factors determining spike timing reliability are complex. In the following, we will concentrate on the interplay between the first and the third aspect. Four chapters of this thesis are devoted to the analysis of reliability. We can separate three topics: A systematic investigation of frequency preference of spike timing reliability and the mechanisms that shape it. The influence of intrinsic parameters on the tuning of frequency preference. Finally, the influence of ion channels on spike timing reliability beyond frequency preference.

Summary

Ion channels are stochastic devices that determine the voltage across the cell membrane through selective gating of ions. Their effect on the membrane potential can be described by conductance-based models, first introduced by Hodgkin and Huxley (1952). The existence of many different ion channel types and many different regulation mechanisms suggests that the differential properties of ion channels play specific roles in the integration of signals in single neurons.

A specific mechanism that influences the translation of signals into voltage responses is

subthreshold resonance. For nonspiking responses to sinusoidal stimuli, this resonance leads to maximal response amplitudes at non-zero frequencies. Subthreshold resonance can be characterized in terms of the electrical impedance, which is conveniently estimated on the basis of so-called ZAP stimuli. The composition of ion channels in a neuron determines which frequencies lead to the largest responses.

One important property of spiking responses is the reliability of the timing of spikes. Although various neural noise sources impair the reproducibility of responses to the same stimulus, spike timing reliability has been found to be very high in a large number of cell types. Reduced reliability is characterized by temporal jitter in the timing of individual spikes as well as in the absence of some spikes or the occurrence of additional, noise-triggered spikes. Reliability can be assessed on the basis of a correlation measure. For the analysis of reliability two aspects are fundamental: properties of the stimulus and intrinsic properties of the cell, such as the composition of ion channels. A large part of this study is devoted to the investigation of the mechanisms that lead to frequency preference of spike timing reliability.

Chapter 3

The integration of subthreshold signals

With this chapter we begin the investigation of frequency-selectivity in the subthreshold regime. While a large part of the thesis analyzes spiking responses, we here start with purely subthreshold responses.[1]

3.1 The questions

As we have discussed in the previous chapter, the electrical impedance is frequency-dependent and thus also determines the frequency-dependence of response amplitudes. The impedance profile, however, is estimated on the basis of periodic (sinusoidal) stimuli or ZAP-stimuli, which for small time windows resemble sinusoidal stimuli. It has been questioned recently, whether the findings based on these approaches also extend to more general stimuli, such as randomly fluctuating inputs. One study, in particular, implies that subthreshold responses to noise stimuli are strongly nonlinear and nonresonant, and suggests distinctive input-output relations under subthreshold and suprathreshold conditions (Haas and White, 2002). While they describe a subthreshold resonance on the basis of periodic stimuli, they do not observe frequency-dependence in the integration of subthreshold nonperiodic noise stimuli.

Because response properties that strongly depend on stimulus characteristics would have far-reaching consequences for our basic understanding of neural dynamics and information processing, we repeated some of the experiments in the same system: the superficial layers II and III of the entorhinal cortex. These neurons show two types of resonance behavior: Stellate cells in layer II exhibit a prominent peak in the impedance at stimulus frequencies of 5–16 Hz. Pyramidal cells in layer III show only a small impedance peak at low frequencies (1–5 Hz) or a maximum at 0 Hz followed by a monotonic decrease of the impedance. Both cell classes vary strongly in their dynamical characteristics so that generic properties of subthreshold input-output relations can be identified. We ask whether frequency-selectivity observed for periodic stimuli also extends to nonperiodic stimuli, specifically colored noise stimuli of different cutoff frequencies, or whether a separate mechanism has to be assumed for nonperiodic stimuli. In addition we want to find out whether the effects found in the subthreshold regime also translate into the spiking regime in terms of firing rate.

---

[1]This chapter is adapted from Schreiber *et al.* (2004a).

3.2   The noise stimuli

In order to analyze whether the subthreshold frequency selectivity in response to periodic inputs also influences the integration of nonperiodic inputs, four different types of frozen low-pass filtered Gaussian noise stimuli are used, following the analysis of (Haas and White, 2002). Gaussian white noise is convolved with a low-pass filter $f(t)$, with $f(t) = e^{-t/\tau}$, for $t > 0$ and zero otherwise. The time constant, τ, determines the cutoff frequency, $f_{\text{cut}}=1/2\pi\tau$, of the resulting stimulus. Values of τ used are 80, 20, 10, 3 ms, leading to cutoff frequencies of approximately 2, 8, 16, and 53 Hz, respectively. Through the filter operation the power of the stimulus is distributed unevenly over frequency space. The smaller the cutoff frequency, the more of the total stimulus power is allocated to the lower frequencies. A 2 Hz cutoff stimulus, for example, contains 93 % percent of its power in the range below 20 Hz (see Fig. 3.1A), whereas the 53 Hz cutoff stimulus contains only about 23 % of its power in this frequency range. We refer to the first three types of stimuli as lower-frequency stimuli and the 53 Hz cutoff stimulus type as a broadband stimulus.
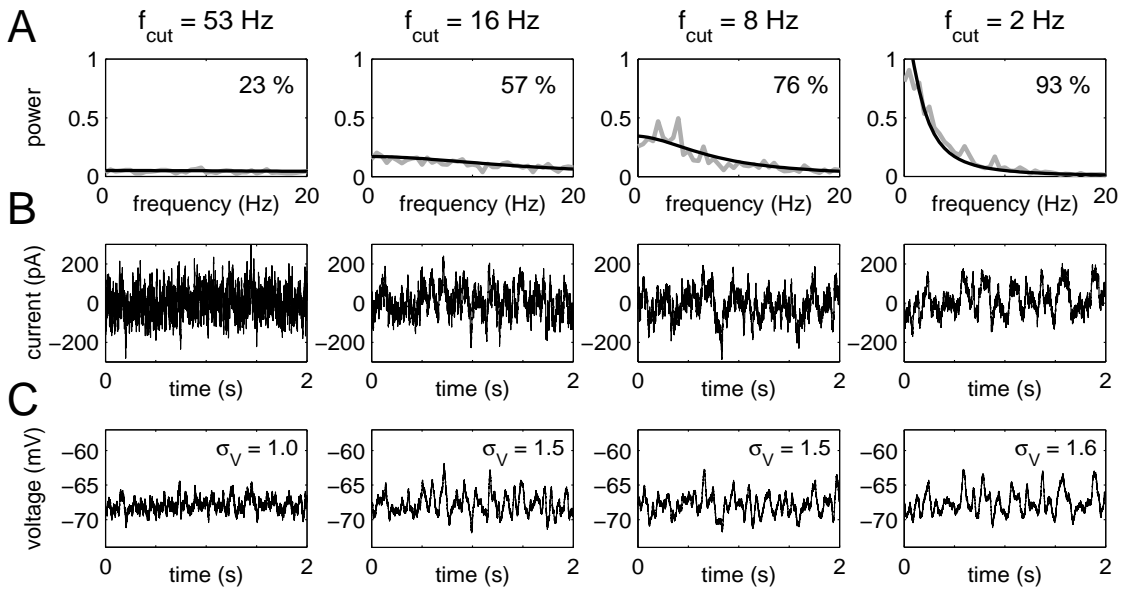
Figure 3.1: Stimuli and responses. **A** Actual average power spectra of the four stimulus types, which differed in their cutoff frequency, f_{cut}. The black line indicates the idealized theoretical power spectra, the labels in the panel's upper right corner denote the percentage of stimulus power that is contained in the frequency band below 20 Hz. Lower-frequency stimuli ($f_{\text{cut}}=16$ Hz and below) have a large percentage of power allocated at frequencies below 20 Hz. The stimulus $f_{\text{cut}}=53$ Hz is more broadband-like and less than 1/4 of its power is allocated to frequencies below 20 Hz. **B** Examples of individual stimuli. All stimuli have the same standard deviation (RMS = 50 pA). **C** Responses of the stellate cell presented in Fig. 3.2. The RMS voltage fluctuation is marked in the upper right corner. Response amplitudes of the broadband stimulus are significantly lower than those of the lower-frequency stimuli.

All raw stimuli had a duration of 2 sec and were normalized to a root-mean-square (RMS) amplitude of 1. The stimuli were then scaled by an amplitude factor between 0 and 250 pA. Depending on each cell, a DC component ranging between -300 and 300 pA was added. For each recording a total of 40 different realizations of the four stimulus types (10 each) were presented in alternating order. The experimental methods are stated in Appendix D.

3.3 Experimental characterization

3.3.1 General cell parameters

Stable recordings were obtained from 11 entorhinal cortex cells, six of which were layer II stellate neurons and five layer III pyramidal neurons.[2] The neurons were morphologically identified based on biocytin staining. We did not distinguish between different subclasses of pyramidal cells. Fig. 3.2A and 3.2B show the responses of two representative cells to DC current injections. All stellate cells exhibited a typical sag potential in response to both hyper- and depolarizing currents. For three cells prominent membrane oscillations in the theta-band of frequencies were confirmed upon depolarization. No membrane potential oscillations were observed in pyramidal cells. Three pyramidal cells exhibited a sag potential, that had a slower time course than the sag observed in stellate cells. The input impedance, estimated from the response to a current step of either 50 pA or -50 pA (for cells with very low firing threshold), was 32 ± 11 MΩ for stellate cells, and 72 ± 30 MΩ for pyramidal cells. The resting membrane potential of stellate cells was -65 ± 5 mV, membrane time constants were measured as 6 ± 2 ms. The resting membrane potential of pyramidal neurons was -75 ± 6 mV, their time constants were 21 ± 8 ms. Note that always the mean $\pm$ SD is stated.

3.3.2 Impedance profiles

Subthreshold frequency preference was estimated by injecting a ZAP current. Fig. 3.2C and 3.2D show the average response to five presentations of the ZAP current for the cells characterized in the panels above. The prominent peak of the ZAP response for stellate cells around 20 seconds is translated into a peak in membrane impedance at 11.3 Hz, see Fig. 3.2E. The pyramidal cell, however, exhibits low-pass filter characteristics. The impedance function showed a maximum at 0 Hz and fell off with increasing frequencies. All recorded stellate cells had an impedance peak between 7 and 15 Hz (average across cells 11 ± 3 Hz), and a pronounced Q-value (ratio between the impedance at the resonance frequency and the impedance at 0 Hz) between 1.2 and 1.8 (average across cells 1.5 ± 0.3). Pyramidal cells either did not show a resonance at all or the impedance had a maximum at very low frequencies (between 0 and 5 Hz, with an average of 3 ± 2 Hz). In addition, the Q-values of pyramidal cells were low (1.0 to 1.2, average 1.1 ± 0.1). For both cell types the impedances were estimated at a depolarization level that was used for further analysis (i.e. at rest for most cells, but also at moderately hyperpolarized or depolarized levels for some cells). Stellate and pyramidal cells

---

[2]I am grateful to Irina Erchova (Humboldt-Universität zu Berlin/Charité) who performed the experiments.
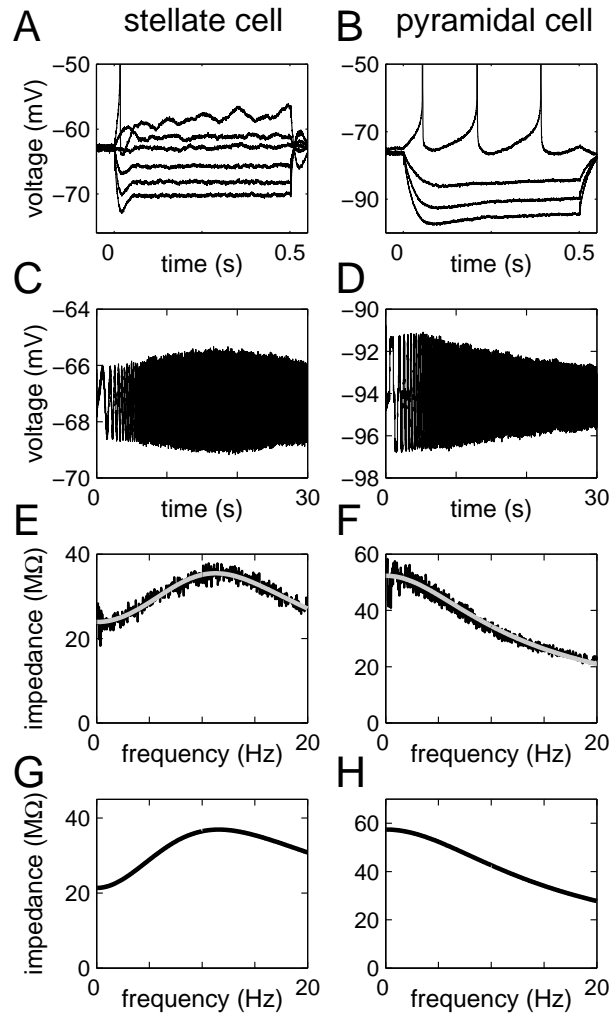
Figure 3.2: Characteristic properties of stellate and pyramidal cells (left and right columns, respectively) **A,B** *Voltage responses to DC current injection (A: -300, -200, -100, 0, 50, 150 pA; B: -300, -200, -100, 50 pA). The stellate cell exhibits membrane potential oscillations at depolarized levels and prominent sag potentials.* **C,D** *Averaged responses to ZAP-current injection (five repetitions, C measured at rest, D measured with a DC component of -260 pA).* **E,F** *Experimental impedance functions derived from the response to the ZAP current presented in C and D (black lines) and the corresponding fits (gray lines) with the electric circuit model described in Methods, see also (Mauro et al., 1970). Stellate cells showed a pronounced resonance at frequencies around 10 Hz. Pyramidal cells mostly exhibited monotonically decreasing impedance functions; three cells also showed a small resonance at low frequencies.* **G**, **H** *Impedance functions of the two conductance-based model cells.*

show only a small dependence of subthreshold resonance frequency on membrane potential. Stellate cells in particular show a stable resonance frequency over a broad range of DC levels (Erchova et al., 2004).

3.4 Noise signals in the subthreshold regime

In order to test the frequency-dependence of the integration of nonperiodic quasi-random noise stimuli, we first assess the total response power of both stellate and pyramidal cells.

3.4.1 Prediction of the response power

If the frequency selectivity estimated from periodic stimulation should equally extend to non-periodic quasi-random stimuli, one would expect that the total response power depends on the subthreshold resonance profile and frequency content of the noise stimuli. In this case, theoretical predictions of the standard deviation (or root-mean-square value, RMS) of the voltage response based on linear system's theory should match the standard deviation (or RMS) of experimentally recorded responses to the corresponding stimuli. Such theoretical predictions can be obtained from the stimulus spectra and the cell's measured impedance function: assuming linearity, the amplitude spectrum of the voltage response corresponds to the product of the amplitude spectrum of the input, $\tilde{I}(f)$, and the frequency-dependent impedance function, $\tilde{Z}(f)$. Taking into account that the variance of any time-dependent function equals its integrated power spectrum over positive frequencies, the predicted RMS value reads

$$RMS(V) = \sqrt{\int_0^\infty |\tilde{I}(f)\tilde{Z}(f)|^2 \mathrm{d}f}.$$

It is assumed that the mean of the input $I(t)$ is subtracted before calculation of the amplitude spectrum, $\tilde{I}(f)$.

3.4.2 Experimentally observed response power

For both cell types, we quantified the amplitude of the fluctuating responses by their root-mean-square (RMS) values. Fig. 3.3A presents the voltage response RMS values as a function of the input RMS values for the stellate cell described in Fig. 3.2. The dependence of the response magnitude on the input RMS value is approximately linear. For an input RMS value of 0 all curves approach the baseline noise level (less than 0.2 mV). For the largest RMS values the curves bend due to a slight shift of the holding potential during the experiment. Most importantly, however, the response RMS values between the broadband stimulus and each of the lower-frequency stimuli differ strongly. On the other hand, the lower-frequency stimuli are not significantly different from each other. Fig. 3.3B shows the average population data of the recorded stellate cells and confirms the differential response power to broadband versus lower-frequency stimuli. For all measured cells, the broadband RMS values were significantly smaller than those of each of the lower-frequency stimuli (confidence level 99 % with Student's t-test at all amplitudes for all recorded cells, with the exception of the lowest 10 pA amplitude, which was close to the noise level, and with the exception of the 16 Hz and 53 Hz cutoff-frequency responses for the pyramidal cell at 200 pA presented in Fig. 3.3E, where the confidence level was only 80 %).

The same analysis was performed for the layer III pyramidal cell presented in Fig. 3.2. Panels E and F of Fig. 3.3 show the corresponding experimental RMS values. Also for this cell

type, the response to the broadband stimulus had significantly lower power than the responses to any of the other lower-frequency stimuli. In contrast to the results obtained for stellate cells, the response RMS values also differ among lower-frequency stimuli.
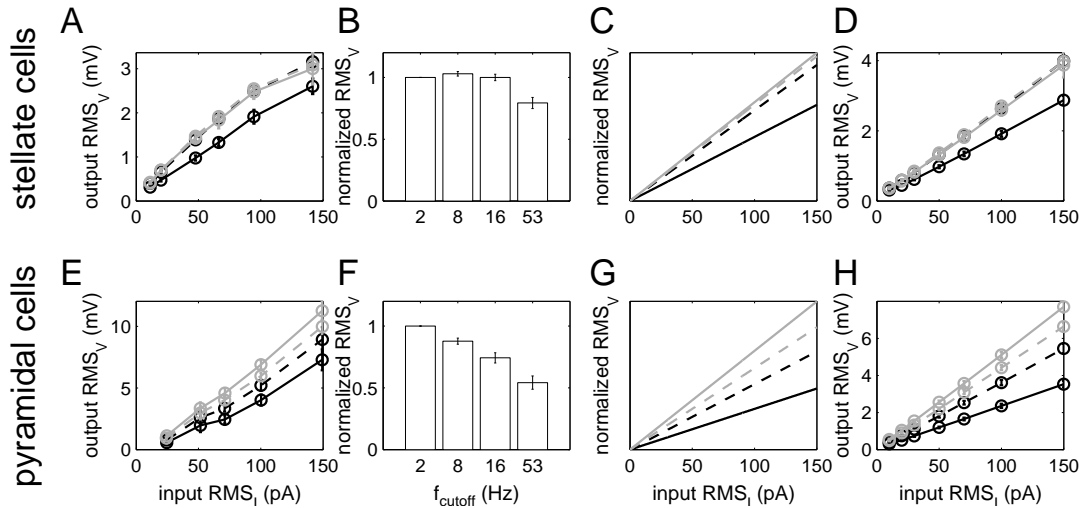
Figure 3.3: Frequency selectivity determines response power. **A** Root-mean-square (RMS) values of the voltage response (mV) as a function of the input RMS (pA) for the stellate cell presented in Fig. 3.2. Different curves correspond to different types of stimuli, with $f_{cut}=2$ Hz (gray solid), $f_{cut}=8$ Hz (gray dashed), $f_{cut}=16$ Hz (black dashed), and $f_{cut}=53$ Hz (black solid). The lowest RMS values are achieved in response to the broadband stimulus. The lower-frequency stimuli yield significantly higher RMS values. In general, the response RMS values increase linearly with stimulus amplitude (or RMS). **B** Relative response RMS values averaged across all stellate cells. The four data points for each input RMS value (from curves such as in A) were normalized by a factor such that the response RMS values to the $f_{cut}=2$ Hz stimulus equal unity. **C** Linear prediction of response RMS values (arbitrary units) on the basis of the measured impedance function for the stellate cell in A. Despite the simplicity of the linear assumption, theoretical prediction and experimental data match well. **D** Similar results are obtained with the conductance-based stellate model cell. **E-H** The same set of results for pyramidal cells. The response RMS value decreases monotonically with increasing f_{cut} of the stimulus. Again, frequency selectivity as characterized by the impedance function allows one to predict the response RMS (G); the model neuron confirms the observation (H). For all presented data, spikes occurring at some of the larger stimulus amplitudes were cut out (10 ms before a spike to 50 ms after the spike). It was checked that the length of these cut out intervals was appropriate to eliminate the effect of spikes.

3.4.3   Theoretical predictions and model cells

Fig. 3.3C and 3.3G depict the linear theoretical predictions of the response RMS values based on the measured impedance function of the presented stellate and pyramidal cell. There is a good agreement between the linear prediction and experimental RMS values, indicating that in both cell types responses to periodic inputs as well as to noise-like stimuli can indeed be explained by the subthreshold frequency selectivity.

In addition, we test how conductance-based model cells with similar impedance profiles integrate noise stimuli. Two types of model neurons were designed to exhibit the subthreshold resonance characteristics of stellate and pyramidal cells, respectively. Subthreshold resonance is achieved by addition of muscarinic potassium channels, M, and H channels. Details are given in Appendix B. The impedance profiles of the model cells measured at rest are shown in Fig. 3.2G and 3.2H. Care was taken that the overall shape of the impedance functions corresponds to the experimental counterparts. The absolute impedance values match qualitatively. For the analysis of response RMS values, small amounts of white Gaussian current noise were injected in addition to the low-pass-filtered noise currents to simulate intrinsic noise sources (standard deviation of $\sigma_n=0.01$ nA for the stellate model cell, $\sigma_n=0.006$ nA for the pyramidal model cell). These values for the standard deviation were chosen to match the noise-induced model voltage fluctuations to the voltage fluctuations observed in experiments. The presence of this additional noise, however, has no significant consequences for the results.

Fig. 3.3D and 3.3H presents the RMS values obtained for the conductance-based model cells with the same set of stimuli. The model results match both, experimental data as well as the theoretical prediction.

3.4.4 Dependence on the DC

Subthreshold resonance is shaped by the dynamics of ionic currents, whose activation often depends on the membrane potential, and may therefore change with membrane potential. As mentioned in Chapter 2, resonance in stellate cells shows only a small dependence on membrane potential: the impedance values moderately increase towards threshold (Erchova et al., 2004), as would be expected from voltage-dependent conductances. The change in resonance frequency with voltage is small. Accordingly, we find that the significant difference in response magnitude between broadband stimuli and lower-frequency stimuli is preserved over depolarized and hyperpolarized values of the membrane potential (data not shown). The difference between the stimuli tends to increase towards threshold. Because, overall, resonance in stellate cells does not dramatically change with membrane potential, we do not expect a qualitative dependence of signal integration on membrane potential in these cells.

3.4.5 Impedance functions calculated on the basis of nonperiodic stimuli

It should be noted that RMS values reflect only the total amount of power. A more detailed picture is given by the distribution of response magnitude over frequencies, which is depicted in Fig. 3.4A and 3.4B on the basis of the experimental responses. For both cell types, the deviations between the responses to the broadband ($f_{cut}=53$ Hz) stimulus and the lower frequency stimulus (as exemplified by the $f_{cut}=8$ Hz stimuli) are largest at low frequencies.

In addition, the impedance function can also be calculated directly from the responses to noise stimuli according to the same procedure as for ZAP currents. Complex impedance functions were obtained for each stimulus and averaged over all stimuli (at fixed input RMS values). This average is justified because there were no significant differences between the impedance functions derived from stimuli with different cutoff frequencies and the impedance fluctuations decrease due to the increased size of the total data set. Because of the shorter
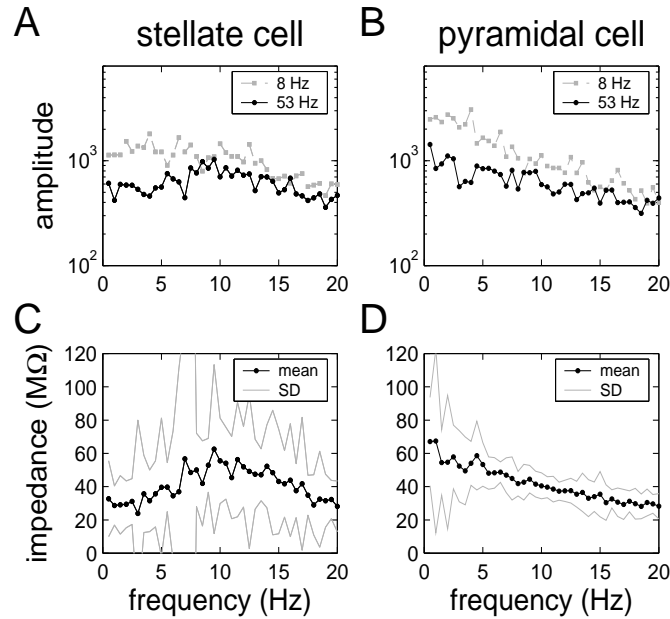
Figure 3.4:   Impedance can be reconstructed from noise stimuli. **A** Amplitude spectra of experimental stellate cell responses to broadband (black solid line, f_{cut}=53 Hz) and lower frequency stimuli (gray dashed line, f_{cut}=8 Hz), input RMS=20 pA each. **B** The same for the pyramidal cell. **C** and **D** The corresponding impedance functions calculated on the basis of responses to all noise stimuli (at the input RMS=20 pA). The thin gray lines indicate the SD of the impedance estimate. Clearly, stellate cells show a nonmonotonic impedance function with a maximum around 10 Hz, similar to the impedance function estimated from ZAP responses (see Fig. 3.2E). For pyramidal cells the impedance function decreases monotonically, as does the impedance estimated from ZAP responses (Fig. 3.2F).

length of noise stimuli, however, these impedance functions are not as smooth as those obtained from stimulation with ZAP currents. The results are presented in Fig. 3.4C and D. For the stellate cell, an impedance peak around 10 Hz is visible. For the pyramidal cell, the impedance decreases monotonically. Overall, the noise-derived impedance functions are very similar to the impedance functions obtained with ZAP stimuli (see Fig. 3.2E and 3.2F). Because the power spectrum of the used broadband noise stimuli is relatively flat (see Fig. 3.1A), the overall shapes of the impedance curves (Fig. 3.4C and 3.4D) mirror the amplitude spectrum of voltage responses (Fig. 3.4A and 3.4B).

3.5   Noise signals in the spiking regime

We now leave the subthreshold response regime and briefly examine whether the differential integration of noise stimuli in the subthreshold regime also has effects on the spiking regime in terms of firing rates. Again, we analyze responses to the set of noise stimuli injected on top of a subthreshold holding current (or at rest). The amplitudes of the noise stimuli are increased

so that spikes are elicited. Fig. 3.5A shows the average firing rate of the stellate neuron from Fig. 3.2 in response to the four noise stimuli (with RMS = 200 pA). Similar to the results in the subthreshold regime, the firing rate evoked by lower-frequency stimuli is higher than that in response to the broadband stimulus (confidence level 99 % with Student's t-test for stimuli with 8 and 16 Hz cutoff frequency, 90 % for stimuli of 2 Hz cutoff frequency). The results for the model stellate cell show exactly the same trend. The measured data as well as the model data suggest that the 16 Hz cutoff stimulus elicits the highest firing rate, but the differences between the three lower-frequency stimuli are not significant.

An extended analysis with the conductance-based model cell involving a tenfold higher number of stimuli per stimulus type suggests an equal firing rate for the 8 and 16 Hz cutoff frequency stimuli (firing rate of approximately 5 Hz), a lower firing rate (approximately 3 Hz) for the f_{cut} = 2 Hz stimulus, and a firing frequency of approximately 1.5 Hz for the broadband stimulus (data not shown).
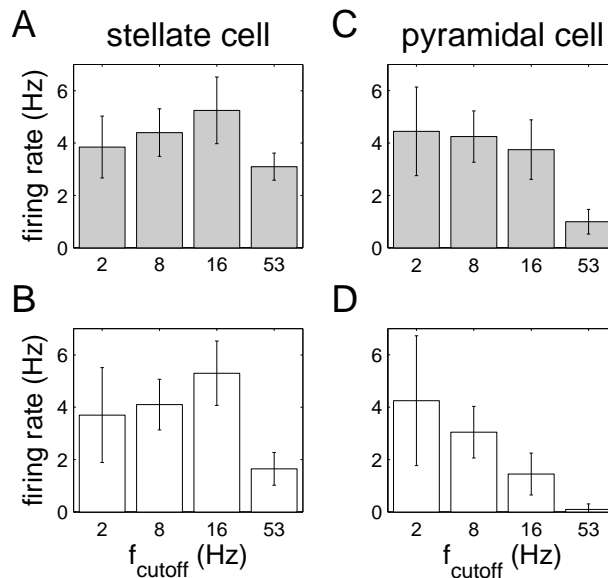
Figure 3.5: Subthreshold frequency selectivity influences firing rate. **A** *Average firing rate in response to each stimulus type for a stellate cell. Similar to the subthreshold regime the firing rates obtained from responses to the lower-frequency stimuli were larger than that of the broadband type stimuli (input RMS = 200 pA).* **B** *The firing rates of the model stellate cell confirms the finding. Stimulus amplitudes (equal for all stimulus types) were adjusted to yield similar firing rates as in the experiments.* **C** *For pyramidal cells the firing rate is a monotonic function of the stimulus cutoff frequency, analogous to the subthreshold regime.* **D** *Qualitatively, the model pyramidal cell shows the same trend. For all panels the error bars indicate the SD of firing rates within one stimulus type.*

For the pyramidal cells the subthreshold frequency selectivity is also translated into a differential firing rate (Fig. 3.5C). The more stimulus power is allocated to lower frequencies, the higher the firing rate. The t-test confirmed a significant difference between the mean firing rate in response to the broadband stimulus and the mean firing rates of the three lower-frequency stimuli (confidence level 99 %). The conductance-based pyramidal model shows a

qualitatively similar behavior. Thus the stimuli resulting in larger response amplitudes in the subthreshold regime also cause the cells to fire more strongly. As firing rate data are not available for the cell presented in Fig. 3.2B, data from a different pyramidal cell are shown in Fig. 3.5C.

The ratio of firing rates in response to different stimuli types depends on the stimulus amplitude. As expected, there is a regime of smaller amplitudes in both the experiment and model where only the lower-frequency stimuli cause a cell to spike, while no spikes are observed for broadband stimuli of the same RMS value. For larger amplitudes the broadband stimulus triggers spikes too, but does not reach the firing rate of lower-frequency stimuli in the amplitude regime tested.

3.6 Discussion

3.6.1 Subthreshold responses

The observed integration of subthreshold signals differs from the findings of Haas and White (2002) in the same experimental system, who do not describe a difference in response magnitude between broadband and lower-frequency stimuli. Comparing the observations in both studies, the responses reported by these authors show a higher level of stimulus-uncorrelated noise. This difference in noise may explain the deviation in the overall RMS voltage response between both studies. Why the studies differ in their observations regarding the response magnitude of broadband and lower-frequency stimuli, however, remains unclear.

Our analysis suggests that nonperiodic signals are integrated according to the same mechanism of frequency-selectivity as periodic signals. Frequency selectivity is determined by the electrical impedance profile, which as we saw is similar for periodic and nonperiodic stimuli. In the subthreshold regime, responses of the recorded neurons can be well described by the principles of linear systems.

3.6.2 Spiking responses

Previous studies have shown subthreshold resonance to influence properties of spiking responses, such as spike timing reliability (Haas and White, 2002) and firing-rate modulation (Richardson et al., 2003). Our data also show that frequency selectivity in the subthreshold regime translates to the spiking regime in terms of firing rate. In the superficial layers of the entorhinal cortex, cells of layers II and III have common cortical input but different hippocampal targets. It has been found that the cells also respond best to synaptic inputs at different frequency ranges. Layer III pyramidal cells are driven most strongly in the 0-5 Hz range, while layer II stellate cells are active at frequencies between 5 and 20 Hz (Gloveli et al., 1997; Heinemann et al., 2000). Our results support the hypothesis that these firing properties are caused by the subthreshold resonance in these cells.

The firing rates, however, are also more sensitive to the particular choice of the stimulus set than the power of subthreshold responses. For model cells, the subthreshold response magnitudes (RMS values) are stable with regard to different stimuli drawn from the same stimulus type, while for stimuli with amplitudes large enough to cause spikes the firing rates

depend more strongly on the specific stimuli chosen. The stimulus type eliciting maximum firing rate is either the 16 Hz cutoff stimulus, or the 8 Hz cutoff stimulus. This observation goes along with the finding that for the stimulus set presented in this paper (Fig. 3.5), no significant distinction between the 16 Hz and 8 Hz cutoff stimuli could be achieved. Nevertheless, the data indicates that additional nonlinearities induced by spiking may influence frequency-selectivity.

Summary

The analysis of responses to low-pass filtered noise stimuli in cells of the entorhinal cortex provides experimental evidence that subthreshold resonance does not only govern the integration of periodic stimuli, but also the integration of nonperiodic stimuli, which has been questioned recently. Differences between the integration of noise stimuli in stellate and pyramidal cells of the entorhinal cortex can be fully explained by the resonance properties of each cell type. Theoretical predictions based on linear system's theory as well as on conductance-based model neurons support this hypothesis. Response power thus reflects stimulus power in a frequency-selective way. The electrical impedance calculated on the basis of noise stimuli is similar to the impedance obtained upon stimulation with ZAP currents.

We also find that the frequency selectivity in the subthreshold range extends to suprathreshold responses in terms of firing rate. Cells in entorhinal cortex are representative examples of cells with resonant or low-pass filter impedance profiles. It is therefore likely that neurons with similar frequency selectivity will process input signals according to the same simple principles.

Chapter 4

Spike timing: the subthreshold regime

We now continue our investigations in the spiking regime and turn from the integration of nonperiodic signals to that of periodic signals. The major focus is shifted to the reliability of spike timing, which remains the central topic of the following four chapters. The first goal is to broaden our understanding of the frequency preference of spike timing reliability. As we will see, however, this does not mean that we completely abandon the field of subthreshold resonance.

4.1   The questions

Whether the timing of spikes is reliable, i.e. whether the pattern of spikes in response to a given stimulus is reproducible in the presence of stimulus-uncorrelated noise, depends on many factors. As we discussed earlier, the intrinsic properties of neurons, additional external signals as well as the statistics of the stimulus play a important role. The first part of the reliability analysis concentrates on the interplay between properties of the stimulus and properties of the cell. The main questions are: Is spike timing reliability frequency-dependent? If so, what are the mechanisms underlying frequency preference? How can intrinsic cell parameters, such as individual conductances, modulate frequency preference?

4.2   The periodic stimuli

The simplest approach to frequency preference is the analysis of periodic stimuli. Because both, stimulus amplitude and frequency may be relevant for spike timing reliability, we use sine waves of different frequencies, f, and amplitudes, C. The mean of the amplitude distribution is formally assigned to a (constant) direct current, I_{DC}. Thus time-dependent stimuli, $i(t)$, take the shape:

$$i(t) = C\sin(2\pi f(t)) + I_{\mathrm{DC}}.$$

For two examples of stimuli see Fig. 4.1A and 4.1C. In principle, I_{DC} represents any constant input component, so that for example constant modulatory synaptic input from other cells can also be viewed as part of the DC.

4.3   Two different regimes

From the dynamical point of view, two operating regimes have to be distinguished in dependence of the DC component. In the first regime, I_{DC} is below threshold. I.e. the neuron does not elicit spikes in response to I_{DC} alone, so that solely the time-dependent component of the stimulus (and potentially intrinsic neuronal noise) is responsible for the occurrence of spikes. We term this the subthreshold regime[1]. In the second regime, the stimulus mean is above threshold, i.e. spikes are elicited in response to I_{DC}, even if no time-dependent component is present. This regime is termed suprathreshold. We can already anticipate that in the suprathreshold regime, the relation of the time-dependent component to the occurrence of spikes can be viewed as modulatory, because the neuron would spike even the absence of this component. Whereas the time-dependent component is causal in the subthreshold regime. In this chapter we investigate the subthreshold regime, while the suprathreshold regime is the subject of the following chapter.

4.4   Dependence of spike timing reliability on the stimulus

First, we analyze, whether spike timing reliability in the subthreshold regime is indeed frequency- and amplitude-dependent. Fig. 4.1B illustrates the response of a conductance-based model neuron to 20 presentations of a 6 Hz sine wave stimulus (presented in the panel above). Because the intrinsic noise (injected as a White noise current of small amplitude in addition to the stimulus) is different in each trial, the spiking responses are variable, although the stimulus is the same for all trials. The noise has a large influence on the occurrence of the spikes, hardly two of the responses are the same in all spike times. In response to some stimulus cycles the cell responds with two spikes, while at others there is only one or none. Fig. 4.1C and 4.1D show a sine wave of different frequency (9 Hz) but same amplitude presented to the same model cell and the corresponding responses (intrinsic noise level and I_{DC} as before). Surprisingly, the cell now responds very reliably. No spikes are missing and the timing jitter is small. Obviously, the spike timing of the cell is frequency-selective.

To analyze frequency and amplitude dependence in a more systematic way, the model cell was stimulated with a whole set of sine waves of different frequencies and amplitudes (I_{DC} remaining fixed). Reliability values for each stimulus were obtained on the basis of correlation of responses to repeated presentation of the stimulus, each with an independent realization of the noise. See Chapter 2 and Appendix A for further details. Reliability as a function of stimulus frequency, f, and amplitude, C, is presented in Fig. 4.2. The upper panel shows a color-coded version of reliability. In analogy to the term established in the regime of stimuli with suprathreshold mean, we will refer to this type of plot as Arnold plot. For comparison, the same data is presented as individual curves for reliability as a function of stimulus frequency in the panel below. Different curves correspond to different stimulus amplitudes.

Fig. 4.2 shows clearly that spike timing reliability increases with stimulus amplitude. For all amplitude levels there is one region of increased reliability around 17 Hz. The cell exhibits

---

[1]The term subthreshold may seem contradictory when referring to the timing of spikes, which are per definition suprathreshold. Subthreshold relates exclusively to the stimulus mean.
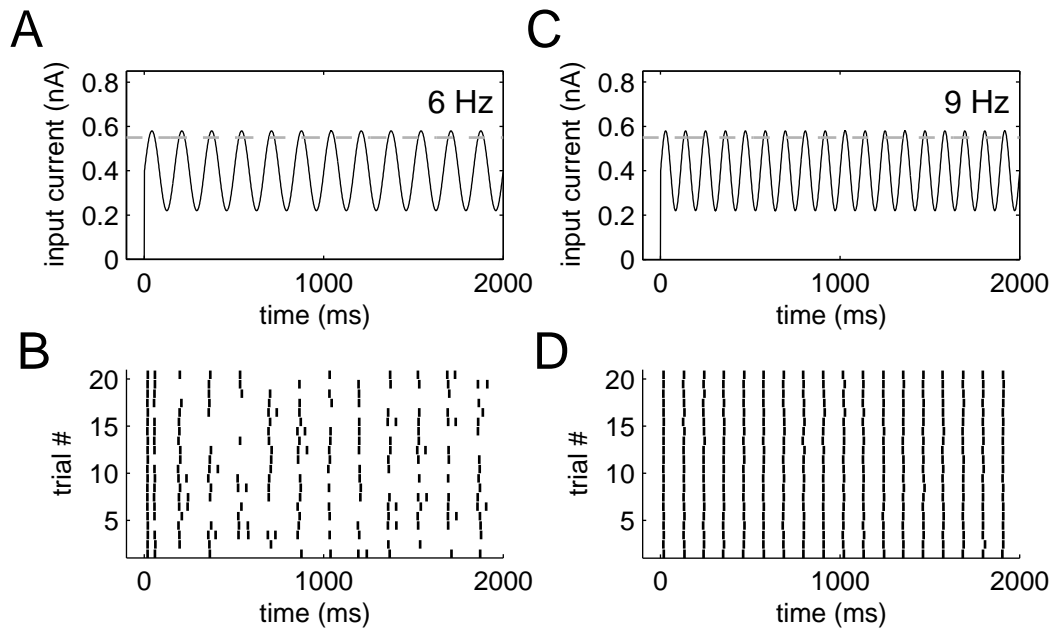
Figure 4.1: Reliability depends on the stimulus frequency. **A** and **C** Examples of 6 and 9 Hz stimuli. The current threshold is marked as a dashed gray line. **B** and **D** Rastergrams with 20 responses of a conductance-based model neuron to the stimuli presented above. While responses to the 6 Hz stimulus show a fair amount of missing and additional spikes, reliability in response to the 9 Hz stimulus is high. The first 500 ms after stimulus onset are discarded for the quantification of reliability.

a clear frequency preference of spike timing reliability. The shapes of the curves are symmetric for small amplitudes but become more asymmetric (with dominance of higher frequencies) for larger amplitudes. More importantly, the reliable frequency range widens with increasing amplitude. At the reliability peaks, responses are mode-locked to the stimuli in a 1:1 fashion, i.e. one spike is elicited per stimulus cycle. To the left and the right of the peak, however, reliability decreases because more and more spikes are missing from a 1:1 mode-locking pattern. At large stimulus amplitudes, responses to frequencies smaller than the best frequency also show a number of additional spikes. Here, a 2:1 mode-locking with 2 spikes per stimulus cycles is adopted, while still a large number of spikes is missing. Accordingly, the rastergram in Fig. 4.1B can show either no spike, one spike, or a spike doublet per stimulus cycle. A more detailed discussion of different mode-locking patterns is postponed to the next chapter, where these response patterns will be more evident. A 1:2 mode-locking (one spike every two stimulus cycles) for frequencies larger than the best frequency is camouflaged by an increasing number of missing spikes.

Due to the large number of missing spikes, also firing rates are reduced with distance from the most reliable frequency. Even in the range to the right of the most reliable frequency the increase in the number of missing spikes surpasses the increase in firing rate and a cell eventually does not fire any more in response to high frequency stimuli.
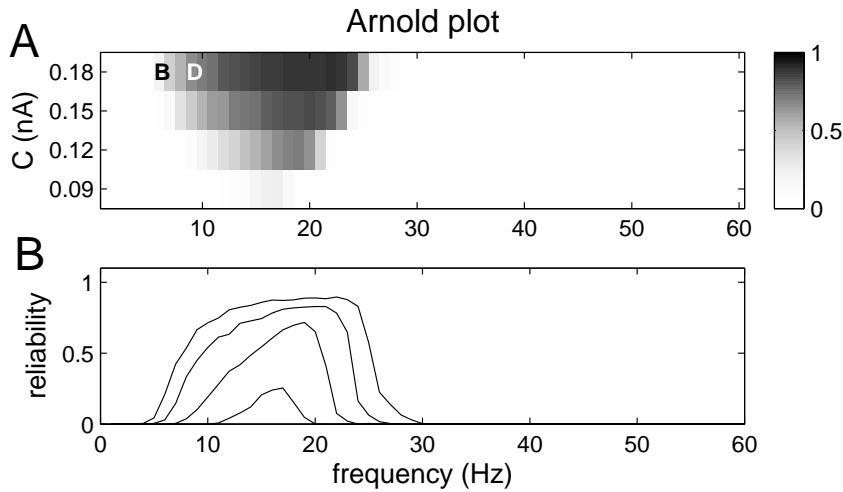
*Figure 4.2: Arnold plot. **A** Color-coded reliability as a function of frequency, f, and amplitude, C, of the sine component in the input. Reliability around $17\,Hz$ is increased. The reliable region extends to neighboring frequencies with larger stimulus amplitudes. Each reliability point is based on responses to 20 repeated presentations of a stimulus. The reliability estimates in the locations marked B and D are based on the rastergrams presented in the corresponding panels of Fig. 4.1. **B** Alternative presentation of the reliability in A. Different curves correspond to different amplitudes, C.*

4.5   Spike timing reliability and subthreshold resonance

How can the frequency-dependence of spike timing reliability be explained? Let us look once more at the influence of amplitude on reliability. The four tested stimulus amplitudes, C, are relatively small. In fact, for the three lower amplitudes the stimulus peak values (given by the sum of the stimulus mean and amplitude, $I_{DC} + C$) are below the current threshold of the cell (here 0.55 nA). The latter is estimated from injection of DC currents and defined as the value of the smallest DC current that causes the cell to fire continuously. Thus at first glance it may be remarkable that the cell elicits spikes in response to those stimuli at all. At second glance it becomes obvious that subthreshold resonance may explain this observation. If the cell has a subthreshold resonance peak at frequencies larger than 0 Hz, stimulus frequencies around the subthreshold resonance will cause larger responses. They may be large enough to cross the threshold and elicit spikes. Potentially, because of their larger "efficient amplitude", these responses will also be more reliable. Fig. 4.3 shows that the model cell presented here exhibits a subthreshold resonance at the given level of I_{DC}. Indeed, the subthreshold resonance frequency coincides with the best frequency of spike timing reliability.

4.5.1   Two example cells with resonance

For a more systematic approach, we discuss three model cells in more detail. The peak conductances of the first two model cells have been selected such that the cells exhibit a clear subthreshold resonance, mediated by a muscarinic potassium conductance ($\bar{g}_M = 1\,mS/cm^2$).
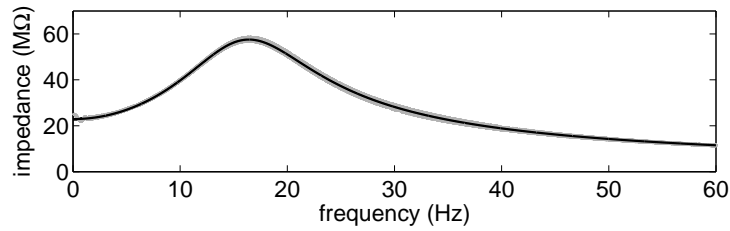
Figure 4.3: Impedance function of the cell presented in Fig. 4.2. The gray line indicates the impedance function calculated from a ZAP of 100 s duration, covering frequencies from 0–20 Hz. The black line shows the corresponding fit with the electrical circuit model. The impedance peak coincides with the reliability peak in Fig. 4.2.

The other conductances present are $\bar{g}_{\mathrm{Na}} = 24 \,\mathrm{mS/cm^2}$, $\bar{g}_{\mathrm{Kdr}}{=}3\,\mathrm{mS/cm^2}$, $\bar{g}_{\mathrm{L}}{=}0.02\,\mathrm{mS/cm^2}$, and $\bar{g}_{\mathrm{NaP}}{=}0.2\,\mathrm{mS/cm^2}$. Both cells have a current firing threshold of 0.55 nA. All parameters are the same, with the exception of the H conductance. While the latter is included in the first cell ($\bar{g}_{\mathrm{H}}{=}0.04\,\mathrm{mS/cm^2}$), the second cell is assumed not to have any H channels ($\bar{g}_{\mathrm{H}}{=}0\,\mathrm{mS/cm^2}$). Consequently, the profile of subthreshold resonance in these cells changes differently with DC (Fig. 4.4): Close to threshold both cells show a subthreshold resonance, mainly mediated by the muscarinic potassium channels. Close to rest, however, the cell with H shows a clear resonance around 8 Hz, while for the cell without H the impedance profile peaks at 0 Hz. If subthreshold resonance determines the preferred frequency of spike timing reliability, we would expect that the two cells show a similar spike timing profile close to threshold, but a clear difference in the spike timing frequency-dependence for lower DC levels.

Fig. 4.5A depicts Arnold plots for the cell with H over a wide range of DC levels, I_{DC}. Because larger stimulus amplitudes are required to cause the cell to fire from rest than to cause the cell to fire from just below threshold, amplitudes were chosen differently for each DC level (as 60, 80, 100, and 120 % of the difference between I_{DC} and the current threshold). At all DC levels the Arnold plots clearly show a region of increased reliability. Towards threshold, this region slightly shifts towards higher frequencies. Note that the DC levels underlaid in gray are suprathreshold. They can be regarded as appetizers for the following chapter. For the moment, however, we ignore this part of the figure and concentrate on the subthreshold levels of I_{DC}. For the latter, the subthreshold resonance frequencies (obtained from responses to ZAP currents of 0.02 nA amplitude) are marked below the frequency axis. Obviously, subthreshold resonance frequency correlates well with the location of the high reliability region at each DC level.

Similar results are obtained with the model cell without H, which is shown in Fig. 4.5. Again, regions of increased reliability are visible. For larger DC values the reliability profiles of both cells are very similar. For the low DC levels the high reliability regions are located at smaller frequencies than those of the cell with H. This DC dependence coincides with the trend of the subthreshold resonance. Also the cell without H shows a correlation between the subthreshold resonance frequency and preferred spike timing frequency. Closer to threshold, however, this correlation is better than close to rest. An explanation for the discrepancy at low DC levels and a better estimate of the preferred frequency of spike timing reliability will
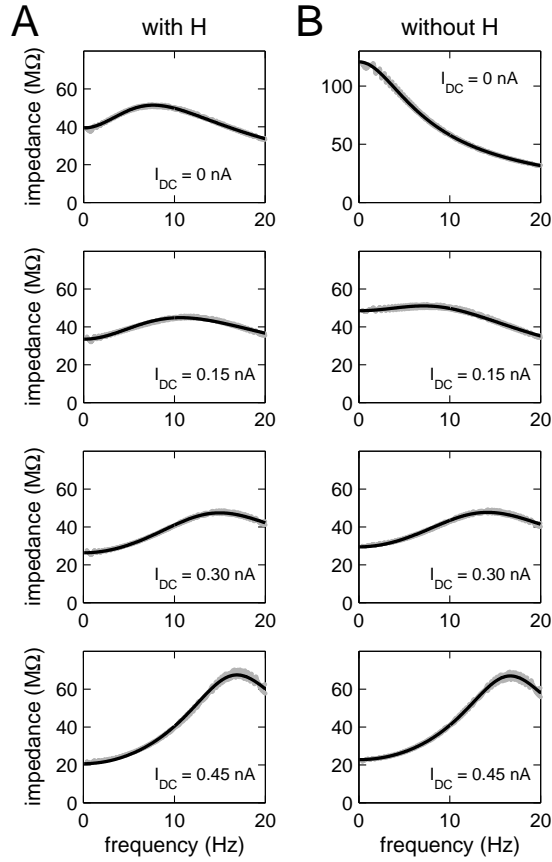
Figure 4.4: Impedance profiles of two conductance-based cells. **A** Impedance profile for the cell with H channels (see text) for 4 different DC levels, as indicated. The cell exhibits a subthreshold resonance at all DC levels from rest to threshold; the resonance frequency increases towards threshold. **B** Impedance functions of the same cell without H channels (all other parameters are the same; the current threshold is still at 0.55 nA, as for the cell with H). In contrast to the cell with H, this cell shows no subthreshold resonance at rest, while the impedance profile closer to threshold is almost identical to that in A.

be discussed in the following section. Before doing so, however, it is necessary to also perform the negative test - what does the reliability profile of a cell without subthreshold resonance look like?

4.5.2   An example cell without resonance

Such a neuron can be obtained by not including currents responsible for subthreshold resonance. The nonresonant cell therefore does not contain H or M conductances, whereas $\bar{g}_{\mathrm{Na}}{=}24\,\mathrm{mS/cm}^2$, $\bar{g}_{\mathrm{Kdr}}{=}3\,\mathrm{mS/cm}^2$, $\bar{g}_{\mathrm{L}}{=}0.04\,\mathrm{mS/cm}^2$, and $\bar{g}_{\mathrm{NaP}}{=}0.02\,\mathrm{mS/cm}^2$. A small slow potassium conductance, $\bar{g}_{\mathrm{Ks}}{=}0.1\,\mathrm{mS/cm}^2$, is also implemented to increase the firing threshold (here 0.17 nA). It is not large enough to cause a subthreshold resonance. The resonance profile
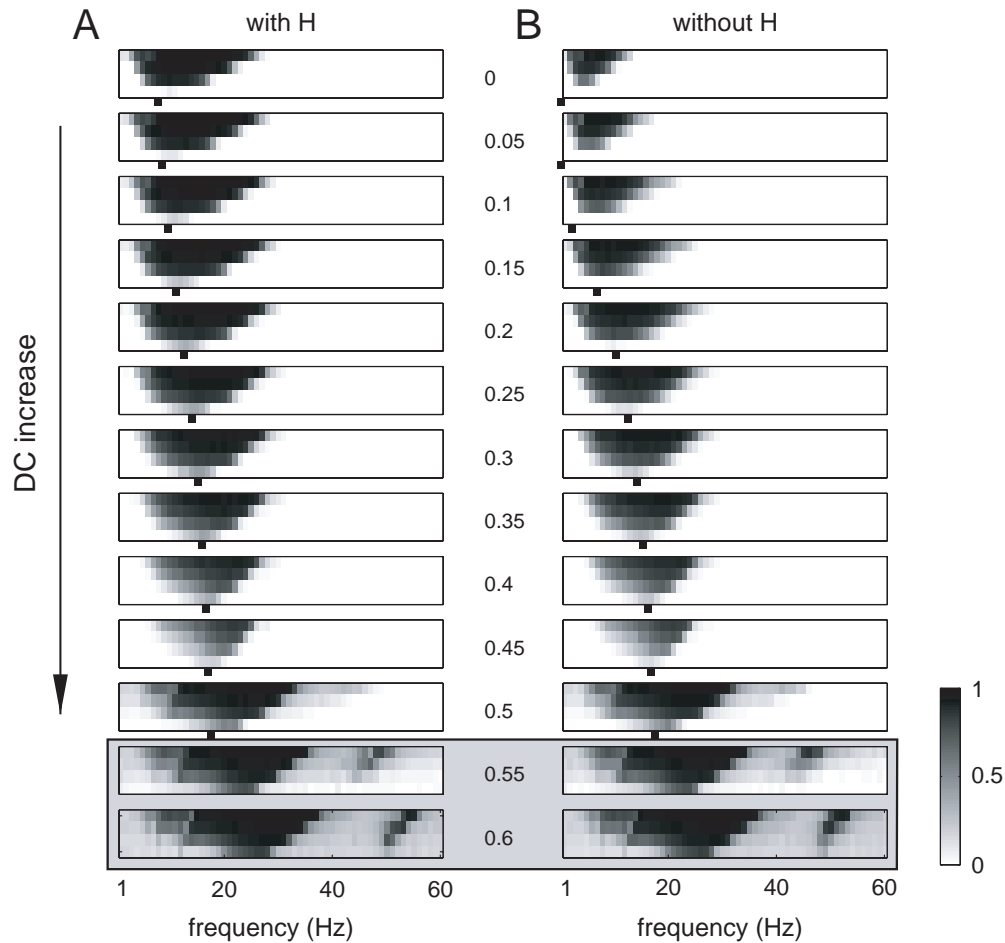
Figure 4.5: *Arnold plots of conductance-based cells.* **A** *Arnold plots of the conductance-based cell with H (as in Fig. 4.4A) for various DC levels (from rest to above threshold). At each DC level (values indicated in the middle column in nA), regions of increased reliability are visible. These correlate well with the subthreshold resonance frequency marked by the filled square below each Arnold plot.* **B** *The same data for the cell without H (as in Fig. 4.4B). The subthreshold resonance frequency matches the preferred frequency of spike timing reliability. The largest deviations occur close to rest. Note that the gray background indicates suprathreshold DC levels, whose discussion will be postponed until the next chapter.*

has low-pass-filter characteristics at all levels between rest and threshold (data not shown).

Fig. 4.6 shows the Arnold plots at different levels of I_{DC}. Again, regions of increased reliability exist. For all subthreshold DC levels but the one just below threshold, this region is located at the lowest frequencies. Thus also for nonresonant cells, frequency preference of spike timing reliability correlates the the subthreshold frequency preference. Once the threshold is crossed (and slightly below) we observe an increase in the preferred frequency. The discussion of this observation, however, is postponed until Chapter 5.
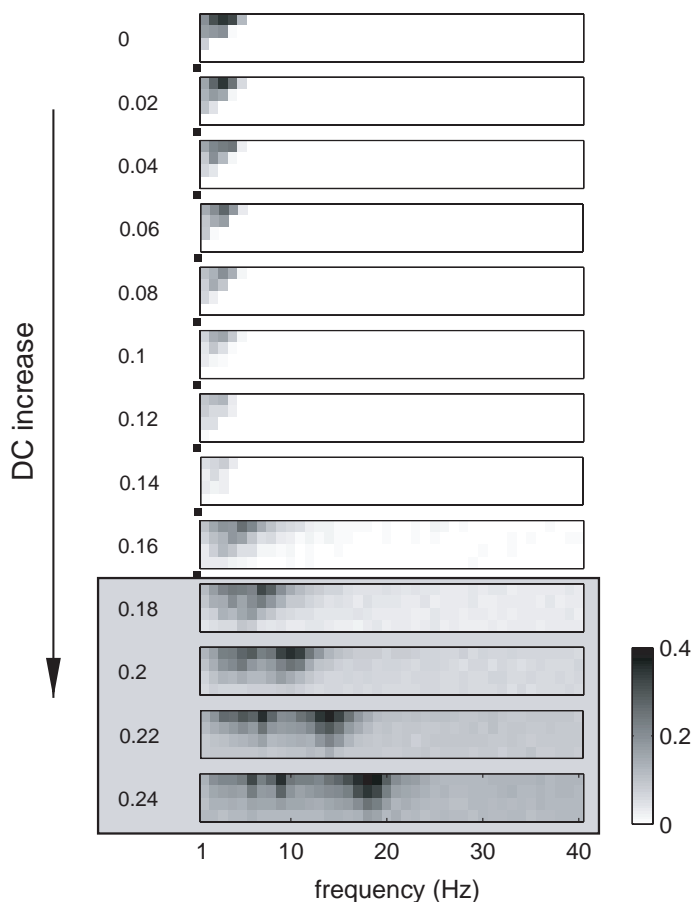
Figure 4.6: Arnold plots of a nonresonant cell for different DC levels (as indicated to the left in nA). The cell does not exhibit subthreshold resonance at any DC level (as indicated by a resonance frequency of 0 Hz, marked by a filled square below each panel). The Arnold plots show a corresponding peak at very low frequencies. Only above threshold (gray background) the reliable spike timing regions shift to higher frequencies, which will be discussed in the following chapter. The amplitudes were chosen as 90, 110, 130, and 150 % of the difference between I_{DC} and the current threshold.

4.6 Amplitude dependence of subthreshold resonance

So far we have seen that subthreshold resonance is a good predictor for the frequency preference of spike timing reliability. The agreement is reasonable, though larger deviations occur for DC levels close to rest. What remains open is the question why the estimate improves towards threshold. Or in other words, what is the cause of the discrepancies closer to rest? To answer these questions we will first investigate the amplitude-dependence of subthreshold resonance.

For stimuli with subthreshold mean, the amplitude of the time-dependent stimulus component has to be large in order to elicit spikes. This holds especially for values of I_{DC} far away
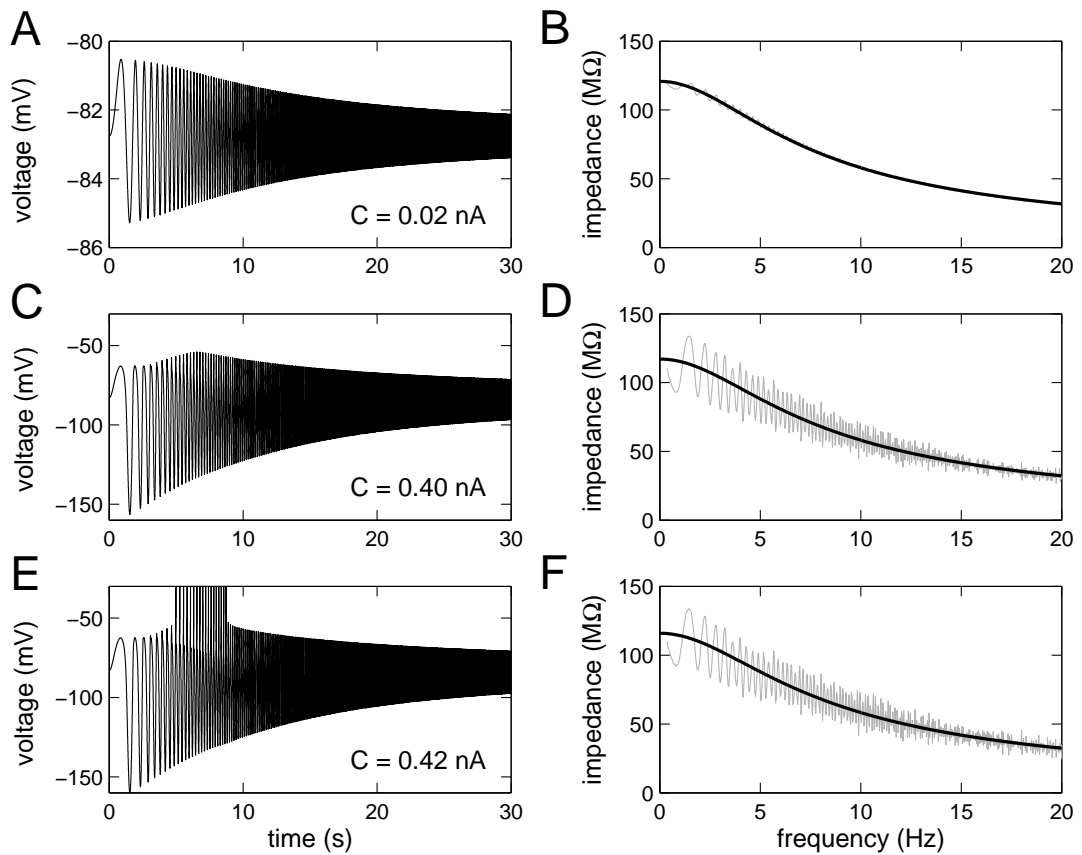
*Figure 4.7: Amplitude dependence of responses to ZAP stimulation. **A**,**C**, and **E** Responses to ZAP currents of three different amplitudes (as marked). While the response to small-amplitude ZAPs decays monotonically, responses to larger-amplitude ZAPs show a peak (at approximately 7 s) in the upper response envelope (B). If the ZAP is large enough to elicit spikes, these occur at a similar time (i.e. similar stimulus frequency). **B**, **D**, and **F** The impedance profiles corresponding to the responses on the left (gray line for the impedance, black line for the fit with the electrical circuit model). Interestingly, the maxima in the upper response envelope to the ZAP currents are not reflected in the impedance functions, which are very similar for all three amplitude levels. Also note that the large wiggles in the raw impedance data based on large-amplitude ZAPs (gray lines in panels D and F) reflect the influence of nonlinearities.*

from threshold. In the previous chapter we have shown subthreshold resonance to act approximately linearly in stellate cells. Thus one could conclude that amplitude should not matter much. On the other hand, for stellate cells the subthreshold resonance profile is relatively stable over a large range of DC levels. This is different in the case of our model cells, especially for the cell without H, where also the largest deviations between subthreshold resonance frequency and preferred spike timing frequency have been observed.

Fig. 4.7A shows the response of the above described model cell without H to a ZAP current of small amplitude (0.02 nA) at rest ($I_{DC}=0$). Already the ZAP response itself indicates that

the cell most likely has no resonance at this DC level. Indeed, Fig. 4.7B confirms this conclusion and shows a resonance profile with a maximum at 0 Hz and low-pass filter characteristics. The stimulus amplitude that was required to elicit spikes (for the corresponding Arnold plot in Fig. 4.5), however, was twentyfold larger (C=0.41 nA). Fig. 4.7C shows the response of the same cell to a ZAP of equally large amplitude (0.4 nA). It was assured that the amplitude was still small enough so that the response did not contain spikes. Unexpectedly, the response is asymmetric with regard to the line of mean voltage (parallel of the time axis): a global maximum around 4 Hz is evident for the upper part of the response, whereas the envelope of the lower part of the response is monotonic. So far, for lower ZAP amplitudes both upper and lower response envelopes showed similar (sign-inverted) trends. More remarkably, the maximum of the upper response envelope is not reflected clearly in the impedance profile. Fig. 4.7D depicts the impedance profile calculated from the response to the large-amplitude ZAP. The profile shows slight deviations from that of the low-amplitude ZAP, but overall, the impedance function peaks at 0 Hz and is monotonically decreasing.[2]

Although deviations between upper and lower envelope may not show up in the impedance profile, they can affect the initiation of spikes, as Fig. 4.7E shows. The amplitude of the ZAP is slightly increased (from 0.4 to 0.42 nA), so that the cell elicits spikes for a certain frequency range. Although the impedance function peaks at 0 Hz and thus would predict spike initiation at the lowest frequencies, spikes are first initiated in a higher frequency region (around 4 Hz). This region coincides with the location of the maximum in the upper envelope. Thus for spike initiation, the *upper* part of a ZAP response (of large enough amplitude) is more important than the lower part, which is further away from threshold.

The occurrence of the maximum in the upper response envelope of the cell without H can be intuitively explained from a very simplified point of view. For small amplitudes the input "experiences" only one resonance environment, the local resonance profile around the DC level. For larger amplitudes a wider range of voltages is crossed during up- and downstroke of the signal. The resonance profiles vary significantly over this range of voltages and thus differentially influence signal integration of upper and lower stimulus segments. Signal integration in the large-amplitude case is nonlinear if the shape of the resonance profiles (measured with small amplitude stimuli) strongly depends on the DC level. For small amplitudes, nonlinearities are negligible, even if the resonance profile varies with the DC level.

Thus we can also conclude that amplitude dependence of responses to ZAP currents does not play a significant role for the stellate cells discussed in the previous chapter, given that the dependence of subthreshold resonance on the DC level is low (Erchova et al., 2004). For illustration Fig. 4.8 shows ZAP responses of a model cell that exhibits a stable subthreshold resonance frequency around 10-12 Hz over a broad region of DC levels. The resonance profile and its dependence on the DC level was already discussed in Fig. 2.3C of Chapter 2. The responses to ZAP currents presented at rest are approximately symmetric with regard to the location of the maxima and minima of the upper and lower envelopes for both small and large stimulus amplitude. They coincide with the resonance frequency (at 11 Hz) estimated from

---

[2]The fact that the peak the upper response envelope is not clearly reflected in the impedance function may seem surprising. It helps the intuition, if one takes into account that the difference between the upper and lower response envelopes also does not exhibit a peak.
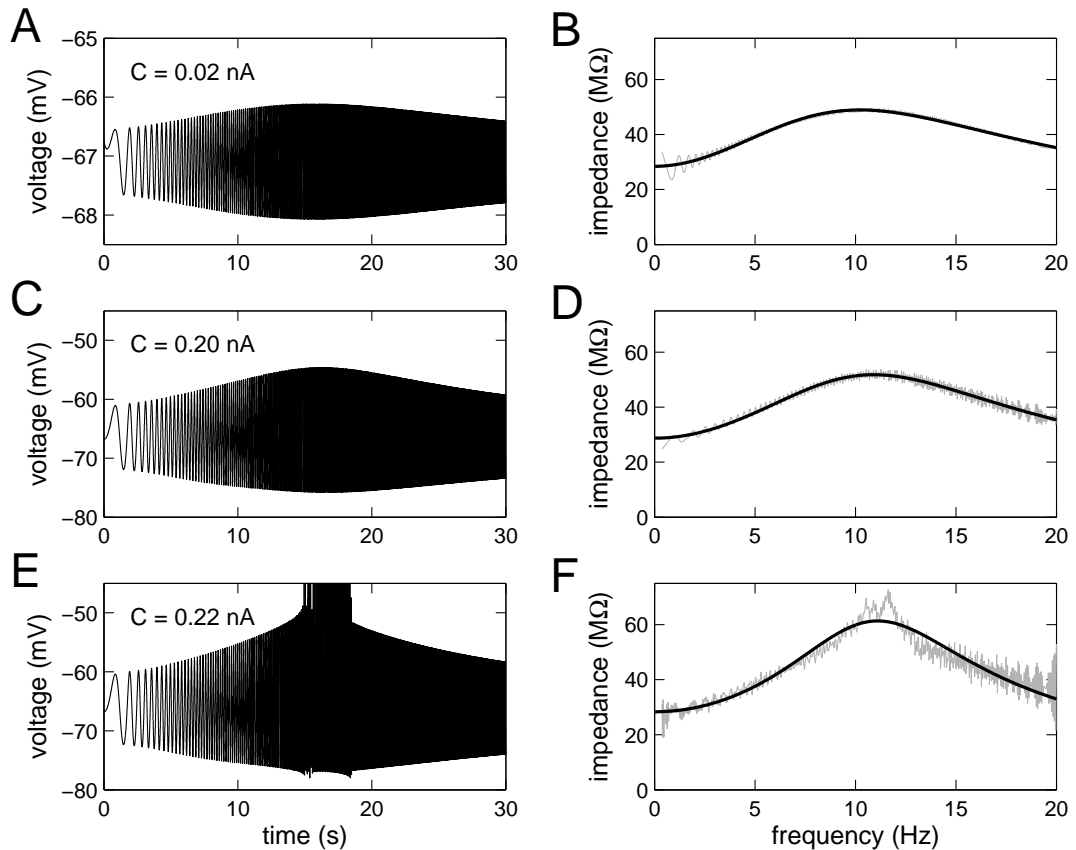
Figure 4.8: Amplitude dependence of ZAP responses in a model cell with a DC-independent resonance frequency. The impedance profile of this cell was analyzed in Fig. 2.3C. **A**, **C**, *and* **E** *In contrast to the cell with a strong DC-dependence of subthreshold resonance, the ZAP responses of this cell indicate no changes in the maximum of the upper response envelope with the DC level.* **B**, **D**, *and* **F** *The impedance functions are similar for all three ZAP stimuli.*

the impedance profile. Fig. 4.8C indicates that for very large stimulus amplitudes, spikes are initiated around the resonance frequency. Obviously, amplitude-dependence is more critical for cells with a strong dependence of subthreshold resonance on the membrane potential.

4.7 A more precise estimate of preferred frequency

The two example cells discussed with regard to spike timing reliability above showed a dependence of subthreshold resonance on the DC level. Thus for large amplitudes, as they are necessary to cause the cells to fire from rest, deviations in the upper ZAP response envelope can be expected. The importance of such deviations for the initiation of spikes therefore suggest that a better estimate of frequency preference of spike timing reliability can be obtained from the upper envelope of ZAP responses with equally large amplitude.

4.7.1   The three model cells revisited

This hypothesis can be tested: Instead of evaluation of the subthreshold resonance frequency estimated from the impedance profile on the basis of small-amplitude ZAP stimuli, we now use the raw responses to ZAP currents of large amplitude. For each DC level, the largest ZAP amplitude that does not elicit spikes is chosen. Consequently, the amplitude of these large ZAP stimuli varies with the DC and close to threshold the amplitudes are rather small (despite the term "large"). The position of the maximum of the upper response envelope in frequency (here plainly approximated by the position of the global maximum of the ZAP response) is determined for each cell as a function of I_{DC}. It is assumed that the position of the response maximum in time can to good approximation be directly related to the frequency of the ZAP at this point in time. Fig. 4.9A and 4.9B shows the summarized data for both model cells.
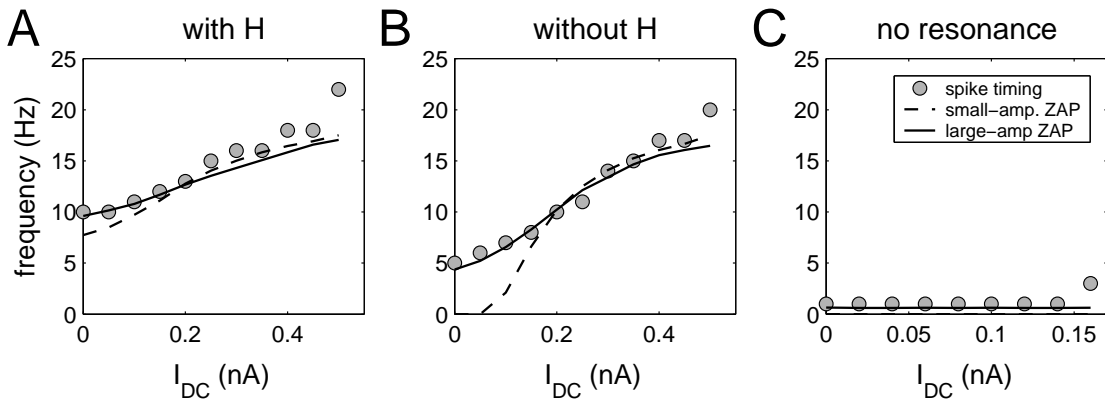
Figure 4.9: *Summary of the spike timing reliability frequency preference as a function of the DC for the three conductance-based model cells presented before.* **A** *Cell with H channels.* **B** *Cell without H channels.* **D** *Cell without resonance. In all panels the frequency with the best spike timing reliability (gray circles), the subthreshold resonance frequency estimated with small-amplitude ZAP currents (dashed line, amplitude 20 pA), and the frequency with a response peak in the upper envelope of large-amplitude ZAP stimuli (solid line) are depicted. The amplitudes of the large-amplitude ZAPs were adjusted to be maximal but cause no spiking responses. For all cells, the upper envelope of the large-amplitude ZAP is a good predictor of the preferred spike timing frequency.*

While the subthreshold resonance frequency already gave a reasonable estimate of preferred frequency of spike timing reliability, the large-amplitude upper envelope measure gives an even better estimate. Closer to threshold, both estimates give similar results, which are close to the preferred spike timing frequency. Here the amplitudes are relatively small, so no deviations between both measures would be expected. Closer to rest, however, the amplitudes necessary to elicit spikes are large and the upper-response measure give better results. The improvement with the new estimate is more obvious for the cell without H. This is not surprising, because the cell also shows a stronger dependence of subthreshold resonance on the DC level.

Note that close to threshold, small-amplitude ZAP responses and responses to ZAP stimuli with an amplitude adjusted to approach threshold give similar results, because in both cases

the amplitudes are small and responses can therefore be well approximated by the integration in the linearized system.

For completeness, Fig. 4.9C shows the preferred frequency of the nonresonant model cell discussed earlier in this chapter. No resonance, also for larger amplitudes, was observed. Both estimates predict a preferred frequency around 0 Hz. Note that the minimum frequency tested with regard to spike timing reliability is 1 Hz.

4.7.2 Morris-Lecar neurons

At the end of this chapter we briefly turn to a reduced type of model neuron – the two-dimensional Morris-Lecar neuron – which was developed to capture the voltage dynamics of the muscle fibers of barnacles (Morris and Lecar, 1981). An advantage of the Morris-Lecar model is that it has been previously shown to exhibit both *type I* and *type II* neuronal dynamics, depending on the values of only a few parameters. If the influence of ion channels on spike timing reliability is mediated through variation of the resonance frequency, a correlation between the resonance frequency and the preferred spike timing frequency is to be expected. One example of each type is analyzed in the following and as we will see, spike timing frequency preference is indeed predicted according to the principles stated above.

Based on a linearization of the system of differential equations, the impedance profile and the resonant frequency for this model are calculated analytically. The details are given in the Appendix C. For the type II Morris-Lecar neuron, the subthreshold resonance profile shows a strong dependence on the DC. The type I neuron does not exhibit a subthreshold resonance, the impedance decreases monotonically at all DC levels. Fig. 4.10 shows the subthreshold resonance frequency for both neuron types (gray solid lines). The resonance profile obtained from the linearization is comparable to the resonance profiles obtained with small amplitude ZAPs.

Numerical analysis of spike timing reliability reveals that both neuron types have preferred frequency (gray circles in Fig. 4.10). For the type II neuron this frequency is between 35 and 65 Hz; it increases with the DC. For the nonresonant type I neuron, the preferred frequency is at very low frequencies. As in the conductance-based model neurons, the subthreshold resonance frequency predicts the general trend of the preferred frequency of spike timing reliability. The estimate for the type II neuron, however, is not very precise.

The reason for the deviations are the strong nonlinearities of the type II neuron (which are also the cause of a strong dependence of the impedance profile on the DC). Also in Morris-Lecar neurons, the numerically derived maximum of the upper response envelope to large-amplitude ZAP currents (with an amplitude adjusted to prevent the cells from firing) gives a better estimate (small black dots in Fig. 4.10A).

As in the more detailed conductance-based model neurons, frequency preference of spike timing reliability is determined by the subthreshold impedance profiles of a cell. In the Morris-Lecar neurons, however, we can observe another effect that is much weaker in the conductance-based neurons, as the following section illustrates.
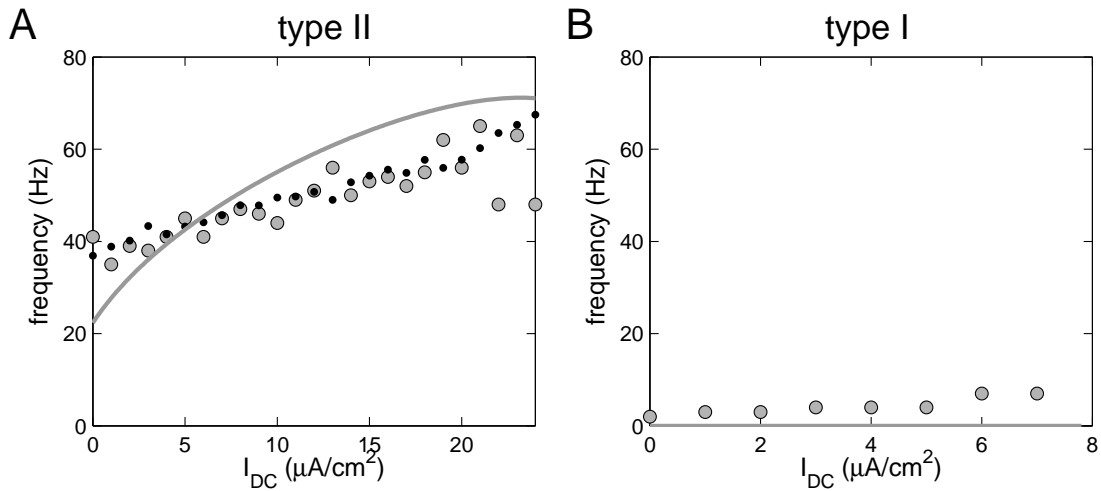
Figure 4.10: Preferred frequency of spike timing reliability in Morris-Lecar type II and type I neurons as a function of the DC. **A** *Type II neuron: The frequency of maximal spike timing reliability (gray circles), the subthreshold resonance frequency of the linearized system (gray line), and the (numerically derived) frequency of the maximum in the upper-response envelope to large-amplitude ZAP stimuli (small black dots) are shown. The large-amplitude ZAP stimuli were chosen with maximal amplitude, under the constraint that the response contained no spikes. Also in Morris-Lecar neurons the upper-response envelope to large-amplitude ZAP currents predicts the best spike timing frequency.* **B** *Type I neuron: The absence of a subthreshold resonance results in very low preferred frequencies of spike timing reliability (gray circles). Note that the regions of increased reliability in the Arnold plots of Morris-Lecar neurons are very wide (also see Fig. 4.11). Consequently, the estimate of best spike timing frequency has a larger error for both cells. For clarity this error is not marked in the figure.*

4.8 Spike timing reliability at the harmonics

Arnold plots of the conductance-based model neurons showed only one reliable region for most DC levels. Only very close to threshold a second region located at the first harmonic of the main region appears. Arnold plots of Morris-Lecar neurons, however, showed two regions of increased reliability for all DC levels (Fig. 4.11A). Fig. 4.11 also depicts three examples of spike trains underlying the reliability values in the Arnold plot. Apparently, in the first region (Fig. 4.11B) responses are phase-locked to the stimuli in a 1:1 mode (one spike every stimulus cycle), while the responses in the second region (Fig. 4.11D) are phase-locked in a 2:1 mode (one spike every second stimulus cycle). In between these regions (Fig. 4.11C) reliability is mainly decreased by missing spikes.

In conductance-based neurons mode-locking can also occur, as the example in Fig. 4.1B indicates. In these examples, however, it was never strong enough to give rise to regions of increased reliability. Quite differently, also for conductance-based model neurons, increased reliability at the harmonics of the preferred frequency is a common phenomenon in the suprathreshold DC regime, as we will see in the following chapter.
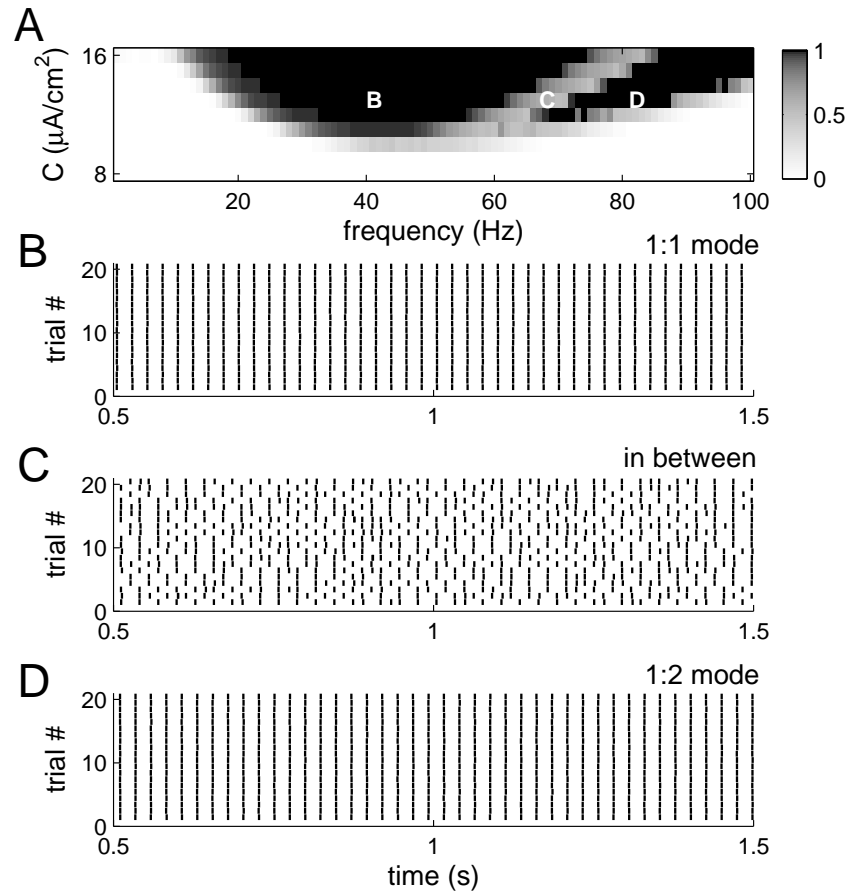
Figure 4.11: Spike timing at the harmonics of the best frequency in Morris-Lecar model neurons. **A** *Arnold plot of the type II Morris-Lecar neuron ($I_{DC}=10\,\mu A/cm^2$). In contrast to the results in conductance-based model neurons, this neuron shows two regions of increased reliability in the investigated frequency-range.* **B-D** *Rastergrams in response to stimuli of different frequencies but fixed amplitude ($C=13\,\mu A/cm^2$). In the first region (example B) highly reliable responses are phase-locked to the stimulus in a 1:1 fashion. Responses in the second area of increased reliability (example D) show 1:2 phase-locking to the stimulus (one spike every two stimulus cycles). Responses in between (as in C) are unreliable.*

Summary

The frequency preference of spike timing reliability has to be discussed separately for stimuli of sub- and suprathreshold mean, which we termed the sub- and suprathreshold regime, respectively. In this chapter we have evaluated spike timing reliability of responses to rhythmic inputs with subthreshold mean.

Spike timing reliability of responses to sinusoidal inputs increases with the amplitude of the time-dependent stimulus component, but also shows a strong dependence on the stim-

ulus frequency. The stimulus frequencies with the most reliable responses can be estimated from the subthreshold resonance profile at the respective DC level. Consequently, cells without subthreshold resonance show best spike timing for low stimulus frequencies, whereas cells with subthreshold resonance show the most reliable spike timing for stimuli at the resonance frequency. We also saw that the responses to large-amplitude ZAP stimuli can be very asymmetric with respect to their mean. This observation leads to an even better predictor of the preferred spike timing frequency: the maximum in the upper envelope of responses to ZAP stimuli, whose amplitudes are large enough to approach threshold but not to elicit spikes.

Generally, at the preferred frequency the spike patterns of cells show a 1:1 mode locking, where one spike per stimulus cycle is elicited. While for conductance-based model neurons only one frequency band of increased reliability is observed, Morris-Lecar model neurons can show a second frequency band, where the response is locked reliably to the stimulus in a 1:2 mode. These reliable mode-locking patterns are more characteristic of the suprathreshold DC regime, as the next chapter will show.

Chapter 5

Spike timing: the suprathreshold regime

As we have seen in the previous chapter, for stimuli of subthreshold mean neurons exhibit a clear frequency preference of spike timing reliability, determined by the subthreshold resonance profile around the mean level of depolarization. For stimuli with a mean above threshold, however, the response to the mean alone contains spikes and the concept of subthreshold resonance cannot be applied. Therefore the question arises, how spike timing reliability depends on stimulus frequency in the suprathreshold regime.[1]

5.1 A suprathreshold resonance effect of spike timing reliability

A mechanism that can explain frequency preference in the suprathreshold regime has been suggested recently (Hunter et al., 1998). It is based on a resonance effect between the stimulus frequency and the intrinsic frequency of a neuron. The latter is determined by the DC firing rate of the neuron and thus also depends on the stimulus mean (or DC). The effect states that spike timing reliability is maximal if the frequency of the stimulus and the intrinsic frequency of the neuron match. This mechanism has been observed experimentally in motor neurons of Aplysia and reproduced in leaky integrate-and-fire model neurons. Many other studies had previously emphasized the importance of the firing rate in the generation of phase-locked firing patters (Keener et al., 1981; Knight, 1972; Rescigno et al., 1970; Hunter et al., 1998; Coombes and Bressloff, 1999).

For our study, we therefore constrain the analysis of the mechanisms to the confirmation that the resonance effect is responsible for the frequency-selectivity of reliability in conductance-based model neurons. In contrast to the previous chapter, where the involvement of ion channels in the generation of frequency preference was only implicit (by shaping of the subthreshold resonance), we now explicitly focus on the ability of ion channels to modulate the preferred frequency in the suprathreshold regime.

5.1.1 Dependence of spike timing reliability on the stimulus

As in the analysis of reliability in response to stimuli with subthreshold mean, sine wave stimuli are used to characterize spike timing reliability as a function of stimulus frequency. Fig. 5.1B and Fig. 5.1C show two examples of stimuli (f = 9 and f = 11 Hz, respectively) and the

---

[1]This chapter is adapted from Schreiber *et al.* (2004b).

corresponding rastergrams of 20 responses each, obtained from a conductance-based model cell that will serve as a reference cell in this chapter. The response to the 11 Hz stimulus is more reliable than the response to the 9 Hz stimulus (at the same DC level, I_{DC}=0.3 nA and for the same stimulus amplitudes, C=0.05 nA). In contrast to responses to stimuli with subthreshold mean (see for example Fig. 4.1), the number of missing and additional spikes is low. Reliability is mainly decreased by jitter in the spike times.
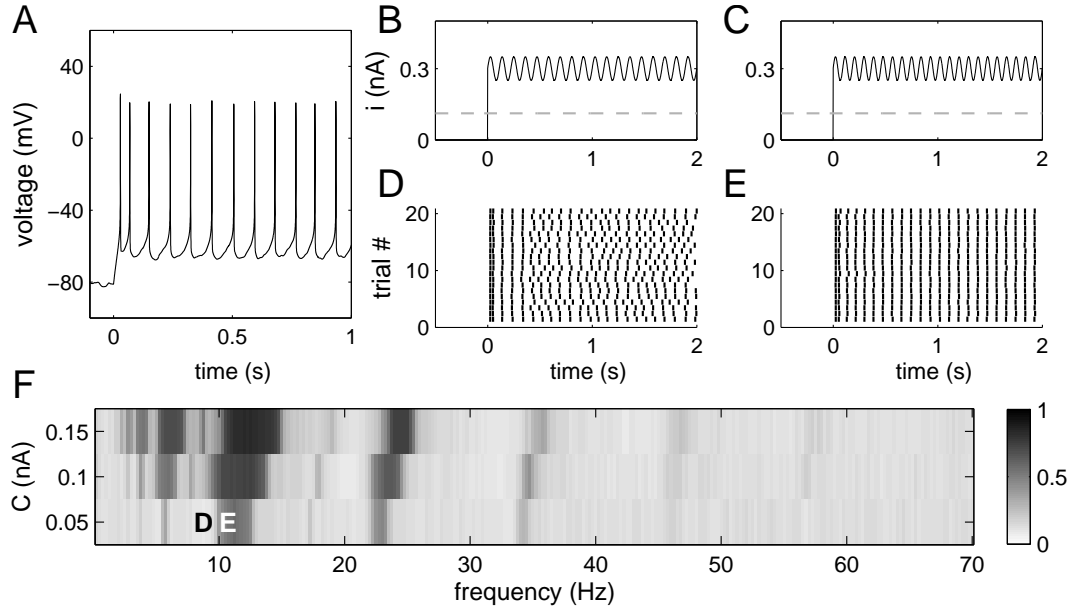
Figure 5.1: Frequency dependence of reliability. **A** Voltage response of the reference cell to a current step of $I_{DC} = 0.3\,nA$ at time 0. The current threshold is marked is a gray dashed line. **B** and **C** Two examples of stimuli used to drive the reference neuron ($f = 9\,Hz$, $C = 0.05\,nA$ and $f = 11\,Hz$, $C = 0.05\,nA$, for the sine component respectively; $I_{DC} = 0.3\,nA$ in both cases). **D** and **E** Rastergrams of the spiking responses to the stimuli presented above. Low reliability values mark unreliable spiking (as in D), where R_{corr}=0.1. Higher reliability values correspond to more reliable spike timing (R_{corr}=0.64 for panel E). **F** Arnold plot depicting reliability as a function of the sine frequency, f, and the sine amplitude, C (here calculated with a high resolution, 0.25 Hz, each data point based on 50 responses). Several "tongues" (regions of increased reliability) are visible. The strongest tongue around 11 Hz corresponds to a 1:1 phase-locking between stimulus and response.

The full characterization of the model cell over a frequency range of 70 Hz and for three different amplitudes of the stimuli (on top of a fixed DC level, I_{DC}=0.3 nA) is shown in Fig. 5.1F. Reliability values (each based on responses to 20 presentations of the same stimulus) are color-coded to yield an Arnold plot. As in the subthreshold regime, spike timing reliability depends on the stimulus frequency. Now several distinct, tongue-shaped regions of high reliability are visible. Because of the similarity to resonance phenomena in physics, the regions have also been termed Arnold tongues (Coombes and Bressloff, 1999; Beierholm et al., 2001). As in the subthreshold regime, the largest reliable region (around 11 Hz) corresponds to a 1:1 mode-locking between stimulus and response (one spike per stim-

ulus cycle). The frequency of the 1:1 mode-locking in the suprathreshold regime, however, is determined by the DC firing rate. The additional regions of increased reliability to the right of the main region are located at harmonics of the resonance frequency, where the cell spikes only at every second or third stimulus cycle (2:1 or 3:1 phase locking). These are now more pronounced than in the subthreshold regime. Smaller high-reliability regions to the left of the resonance frequency are related to 1:2 and 1:3 phase locking, where several spikes per stimulus cycle are elicited. Overall, reliability increases with the power of the input around the resonance frequency and its harmonics and subharmonics. Although several regions of increased reliability exist in the suprathreshold regime, we keep the term preferred frequency for the frequency at the 1:1 Arnold tongue, which in the majority of cases coincides with the frequency of maximum reliability. The preferred frequency does not strongly depend on stimulus amplitude, although a slight shift towards higher frequencies with increasing amplitude can be observed. The effect is limited to a few Hz.

5.1.2 The DC component is fixed

The importance of the DC firing rate for the reliability frequency preference implies that a neuron's preferred frequency depends on the mean level of depolarization (in the model determined by I_{DC}), as well as on the composition of the ion channels at the site of action potential initiation. Because we want to focus on the contribution of ion channels to the preferred frequency, we content ourselves with the statement that it was checked that changes in DC lead to changes in the preferred frequency as predicted by the resulting change in firing rate (data not shown). The possibility of other neurons to modulate frequency preference of spike timing reliability through modification of the DC has been recently investigated elsewhere (Hunter and Milton, 2003). For all plots in this chapter, the DC component of the stimulus remains fixed (to 0.3 nA).

5.1.3 DC firing rate determines the preferred frequency

The relation between the preferred frequency of spike timing reliability and the DC firing rate is investigated for different sets of conductance-based model cells in this chapter. Although the detailed description of the set of model cells is postponed to the following section, a comparison between the DC firing rate and the preferred spike timing frequency is summarized here. Fig. 5.2 shows the preferred frequency (estimated from the location of the strongest Arnold tongue in frequency space) as a function of the DC firing rate (with fixed I_{DC}=0.3 nA). For each cell, preferred frequency is estimated at three different amplitudes (C=0.5, 0.1, and 0.15 nA) of the sine component. Firing frequency and preferred frequency correlate well for all investigated cells. In general, the resonant frequency at the lowest amplitude of the sine component is closest to the DC firing frequency. Two outliers can be seen (around 10 and 20 Hz), where the highest value of reliability was achieved at the subharmonic, or the first harmonic of the DC firing frequency. We conclude that the effect observed in Aplysia and integrate-and-fire can be observed in conductance-based model neurons too. The approximation of the preferred frequency is best for small stimulus amplitudes. Due to nonlinearities the frequency preference may shift with larger stimulus amplitudes.
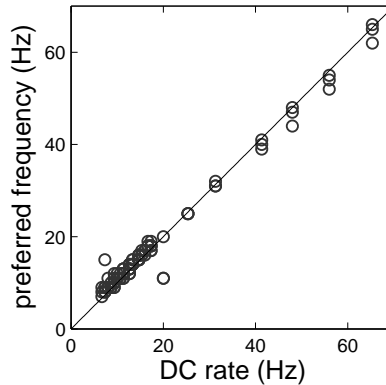
Figure 5.2: DC firing rate (I_{DC}=0.3 nA) and the stimulus frequency resulting in the highest reliability for different sets of model cells. For each cell, the best spike timing frequency is estimated at three different stimulus amplitudes (C=0.05, 0.1, and 0.15 nA). In all cases the DC firing rate correlates tightly with the stimulus frequency resulting in maximal spike timing reliability. The largest deviations (around 10 and 20 Hz) occurred when the maximum reliability was achieved at the first harmonic or the subharmonic of the stimulus frequency. Altogether, DC firing rate is a good predictor of the preferred spike timing frequency.

5.1.4   Spike timing reliability at the harmonics

While in general it is the jitter in the timing of individual spikes that decreases reliability in the suprathreshold regime, phase-locking to different cycles of the stimuli can occur for frequencies neighboring the harmonics of the preferred frequency. Estimated with the correlation measure, reliability will be lowered for these stimulus frequencies, although the precision of individual spikes is relatively high. Fig. 5.3A shows an example. The responses presented in the sequence of recording suggest unreliable spike timing. A reordered version[2] of the same responses shows, however, that the responses split into two classes (trials 1–9 and trials 10–20 in Fig. 5.3B). Reliability within each class is high. Such splitting of responses into different attractors (Tiesinga et al., 2002) is only observed for stimulus frequencies close to the harmonics. A second example shown in Fig. 5.3C illustrates that in between harmonics, reliability is decreased due to jitter in the timing of spikes. Such responses cannot be clustered into coherent patterns; phase-locking between stimulus and response can only be maintained over brief periods of time.

5.2   Influence of ion channels on the preferred frequency

From the discussion of the general mechanism responsible for the frequency dependence of spike timing reliability, we now turn to the capability of ion channels to modulate the frequency preference. Taking into account that effective numbers of ion channels as well as

---

[2]Reordering was achieved with a K-means cluster algorithm involving the correlation measure as an estimate of similarity. Details are described in Appendix A.
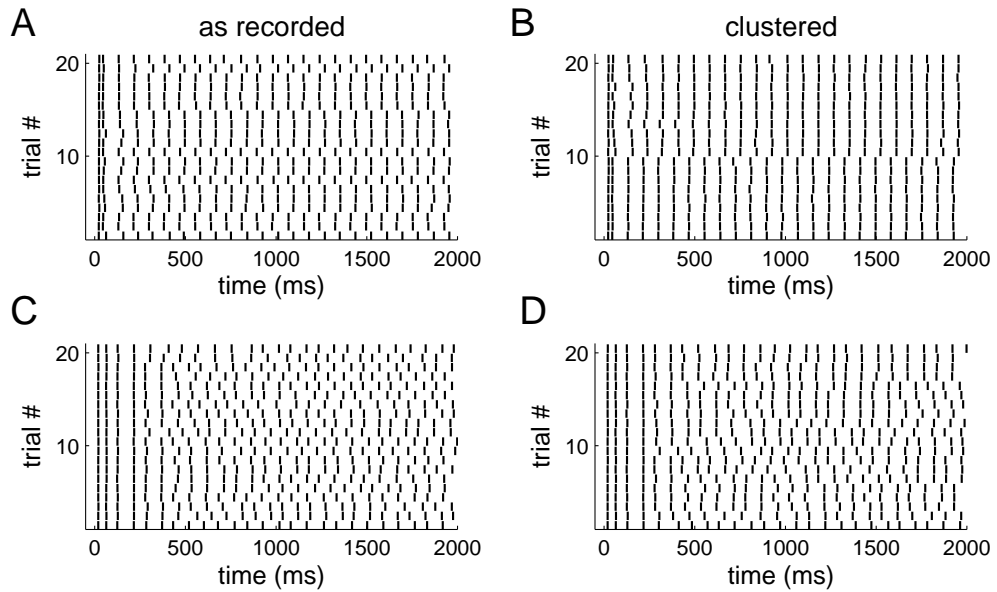
*Figure 5.3: Reordering of spike trains reveals reliable response subgroups close to the harmonics. **A** 20 spike trains elicited by the reference cell in response to a stimulus with a frequency close to the second harmonic (f=35 Hz) in the sequence of recording. **B** The same set of responses presented in a new sequence after application of a clustering algorithm based on the correlation measure (see Appendix A). Two response subgroups can be identified, reliability within each subgroup is high. **C** Responses to a stimulus in the middle between the preferred frequency and the first harmonic (f=20 Hz) in the sequence of recording. **D** Reordered representation of the spike trains in C after application of the clustering algorithm. In contrast to the example shown in A, the responses do not fall into a small number of highly reliable subgroups.*

their properties can be changed on short timescales through neuromodulation and cell-intrinsic messengers, changes in ion channels may provide a useful way for a neuron to dynamically maximize (or minimize) spike timing reliability according to the properties of the input. A strategy achieving maximum spike timing reliability exploits the resonance effect and consequently requires adjustment of the conductances such that the preferred frequency (or its first harmonic or subharmonic) and the stimulus frequency match.

5.2.1 Dynamic regulation

The following example illustrates how changes in the peak conductance of slow potassium channels can serve to regulate reliability (Fig. 5.4). The input to the neuron is a 9 Hz sine wave, on top of a suprathreshold DC current. Spike timing reliability is initially low. The temporary increase in the slow potassium conductance (after 1.5 seconds), results in a significant increase in reliability within half a second. As the decrease in g_{Ks} back to the original value shows, the effect on reliability is reversible. The conductance step is chosen such that the preferred frequency of the cell after the conductance increase is similar to the stimulus frequency. In a

real neuron, the change in conductance would not be instantaneous, however, the change in reliability could be expected to follow the time scale of neuromodulator activation, which is on the order of hundreds of ms.
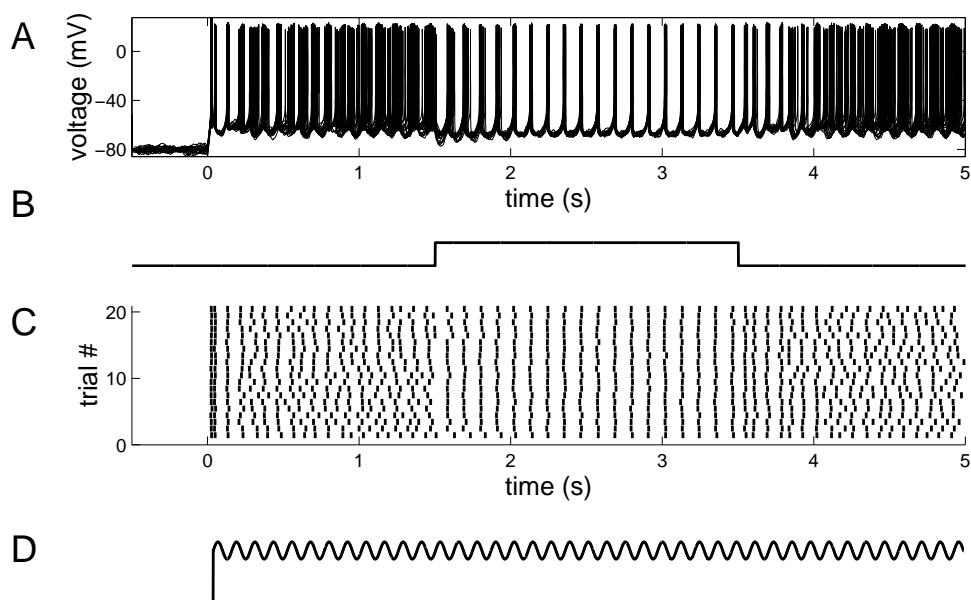
Figure 5.4: Dynamic changes in spike timing reliability due to conductance steps. **A** Superimposed voltage traces (N=20) in response to a sine wave (f=9 Hz, C=0.05 nA), which is shown in **D**. The K_s conductance was temporarily increased, as indicated in panel **B**. **C** Rastergram of the responses. The parameters of the cell were those of the reference cell, g_{Ks} values were 0.9 mS/cm^2 and 1.4 mS/cm^2, noise standard deviation σ=0.03 nA. Reliability (here estimated with σ_t=3 ms) changed from 0.18 to 0.57 at the conductance step and back to 0.17.

5.2.2   Influence of individual ion channels

For a systematic investigation of the influence of ion channels on frequency preference we analyze sets of cells and vary one channel density at a time, keeping the densities of the other channels fixed. As a reference cell we choose the original parameters of the model for a cortical pyramidal cell (Golomb and Amitai, 1997). It is important to include a slow potassium conductance, because it is responsible for a spike frequency adaptation in response to a current step, which has been experimentally observed in cortical pyramidal neurons (McCormick et al., 1985; Connors and Gutnick, 1990). The response of the reference cell to a conductance step from 0 nA to the DC level of 0.3 nA is shown in Fig. 5.1A.

The Arnold plots for two sets of cells (one with modified leak conductance, the other with modified K_s conductance) are shown in Fig. 5.5. Note that different Arnold plots now correspond to different cells (all at the same DC level). All cells show a pronounced region of increased reliability. With an increase in the leak conductance, the preferred frequency only

moderately shifts to lower frequencies. In contrast, an increase of the K_s conductance has a large effect on the preferred frequency; the latter is lowered by more than 60 Hz.
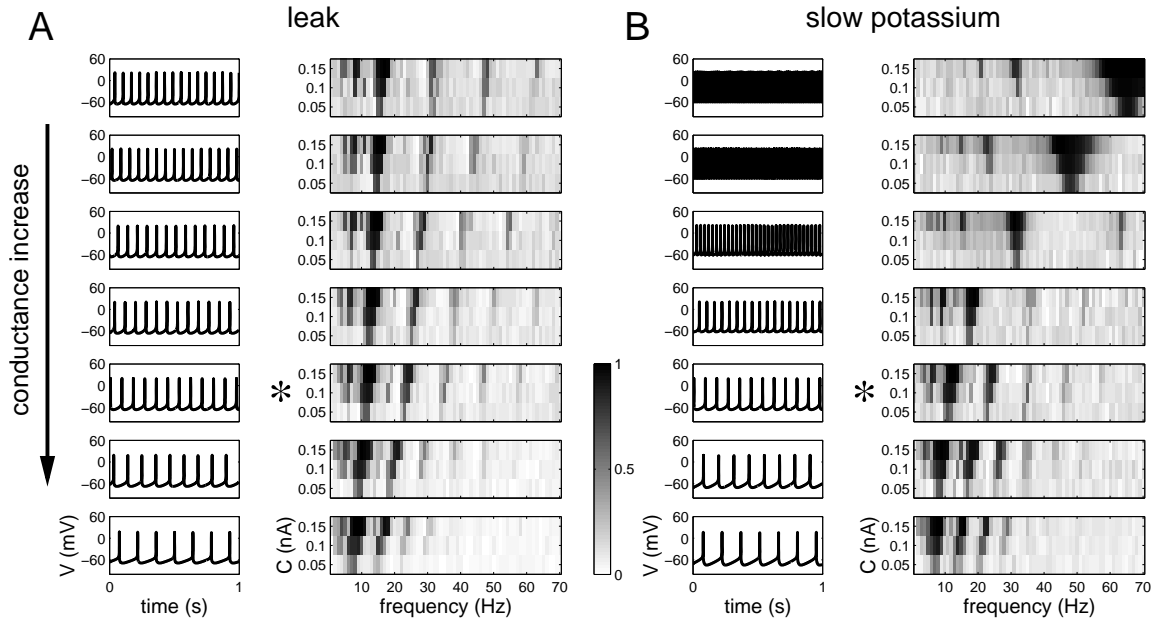
Figure 5.5: Influence of leak and slow potassium conductances on spike timing reliability. **A** *The right column of the left panel shows Arnold reliability plots for seven different model cells, systematically varying in the amount of leak channels present (0, 0.005, 0.01, 0.015, 0.02, 0.03, and $0.04\,mS/cm^2$ from top to bottom). The left column shows spikes of the corresponding cells in response to pure DC stimulation without intrinsic noise.* **B** *Arnold plots and spikes in response to DC stimulation for seven different model cells with increasing amounts of K_s (0.05, 0.15, 0.3, 0.6, 1.0, 1.5, and $2.0\,mS/cm^2$, top to bottom). For both panels the third plot from the bottom (*) represents the reference cell (as in Fig. 5.1F). Variation in $\bar{g}_{Ks}$ achieves larger shifts in the preferred frequency than variation in $\bar{g}_L$.*

Changes in the preferred frequency mediated by the Na, K_{dr}, and Na_P conductances are summarized together with the results for leak and K_s conductances in Fig. 5.6A. The curves represent preferred frequencies that yield maximum reliability (at $C=0.1\,nA$) as a function of normalized channel density. Because each channel type operates in a different range of densities, some of which differ by orders of magnitude, the densities are normalized to the range $[0;1]$ for each channel type (for unnormalized parameters see Appendix C). The conductance range for each ion channel type was determined such that conductance changes from the reference cell resulted in regular spiking responses to $I_{DC}=0.3\,nA$, with a peak voltage smaller than 50 mV. As for leak channels, large changes in Na, K_{dr}, and Na_P densities are necessary to shift the preferred frequency. The overall change for these channel types is in the range of 5 to 15 Hz. Thus starting from the reference cell, only variation in the K_s density can shift the preferred frequency by several tens of Hz from below 10 Hz to more than 60 Hz.

5.2.3   Influence of slow potassium channels

Because the slow potassium channel has proven best to adjust the preferred frequency over a large range of frequencies, we now test the influence of two further potassium channels with slow kinetics on frequency preference of the reference cell: the muscarinic potassium channel M (already known from Chapter 2) and a calcium-dependent potassium channel, K_{Ca}. K_{Ca} is responsible for a slow afterhyperpolarization (Tanabe et al., 1998). It is activated by intracellular calcium and does not depend on voltage. Because of the dependence of K_{Ca} on calcium, an L-type calcium channel is inserted, as well as a simple Ca-ATPase pump and a mechanisms for internal buffering of calcium. For details see Appendix B. In both cases, K_s was substituted by the new potassium conductance, M and K_{Ca}, respectively.
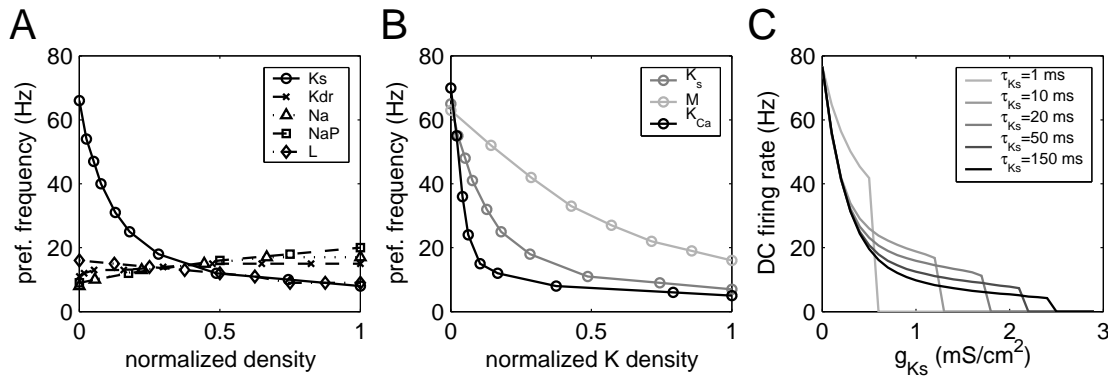
Figure 5.6: Dependence of the preferred frequency of the reference cell on individual channel densities. **A** *Preferred frequency as a function of normalized channel density (definition see text), for five different conductances. Variation in K_s achieves the broadest shift in preferred frequency.* **B** *Preferred frequency for variation in a muscarinic potassium channel, M, and a calcium-dependent potassium channel, K_{Ca}, as a function of normalized channel density (based on sine wave reliability analysis). M and K_{Ca}, respectively, replaced K_s in the reference cell.* **C** *DC firing rate (an estimate of the preferred frequency) for K_s channels of different time constants, τ_{Ks}, as a function of K_s peak conductance. Densities are not normalized in this panel. The lowest achievable frequency (at I_{DC}=0.3 nA) depends on τ_{Ks}.*

The results of the Arnold plot analysis are shown in Fig. 5.6B. For both channel types, an increase of their conductance shifts the preferred frequency over a broad range of frequencies. If two or more slow potassium conductances are present at high densities, the broad tuning effect is diminished and eventually suppressed at high conductance levels (data not shown). Fig. 5.6C presents the preferred frequency as a function of the K_s conductance for different time constants τ_{Ks}. The slower the kinetics of the K_s channel, the lower the minimum achievable frequency and the broader the frequency range accessible through variation of the slow potassium conductance. This matches the observations obtained with the other two potassium conductances (M has the fastest kinetics of the three slow potassium channels, K_{Ca} the lowest).

5.2.4 Firing rate analysis

So far, starting from the reference cell, only one conductance was varied at a time. For a more complete picture of the influence of ion channels on spike timing frequency preference, now all combinations of Na, Na_P, K_{dr}, K_s, and L conductances are analyzed. For computational efficiency we rely on the DC firing rate as an estimate of the preferred frequency. The distribution of maximum changes in firing rate (i.e. preferred frequency) achievable by variation of the density of one ion channel type over all combinations of the other four densities is presented in Fig. 5.7, which shows one curve for each ion channel type. For a more detailed description of this analysis see Appendix B.

The figure shows that K_s has a significant effect on the preferred frequency in almost all parameter regimes. The influence of K_s is weakest when another potassium channel (K_{dr} in this case), is present at high density (data not shown). The mean change achieved with K_s is around 20 Hz, while the mean change achieved by the other ion channels is below 10 Hz.

The analysis also shows that in principle, all ion channel types can achieve changes in preferred frequency of 20 Hz or more. Within the parameter space investigated, however, this is true only for a minority of values of the other four conductances. In all these cases, the K_s conductance was low. Fig. 5.7B shows four examples of parameter regimes where these channels significantly change the preferred frequency.

5.2.5 Experimental results

In order to test the effects of ion channels on preferred frequency physiologically, patch-clamp recordings in slices of rat prefrontal cortex were performed [3]. The experimental methods are stated in Appendix C. We employed the dynamic clamp technique, which allows the injection of realistic time-dependent currents into *in vitro* neurons through online feedback (Sharp et al., 1993; Jaeger and Bower, 1999; Dorval et al., 2001). Because the most interesting influence of ion channels on spike timing frequency preference was observed with slow potassium channels, we chose to artificially introduce the slow potassium conductance, with dynamics equal to those of the K_s current used in the model simulations.

We first characterized its spike timing reliability as a function of frequency of a sine wave input in the "native" conductance state of the cell (the control state). Then responses to the same set of stimuli were recorded – this time in the presence of an additional K_s conductance in the cell, which was introduced with dynamic clamp (the K_s state). The DC level was kept constant and was the same for control and K_s experiment. Fig. 5.8 shows spike timing reliability as a function of the frequency of the input for the control and K_s states. In the control experiment the cell had a preferred frequency of approximately 17 Hz. When K_s was introduced, the preferred frequency was lowered to 7 Hz and the spike timing reliability was increased beyond the maximum reliability of the control state. We observed a negative shift in the preferred frequency for all cells recorded (N=4). For most cells, the shift in the preferred frequency resulted in an increase of spike timing reliability at that value (N=3). For one cell reliability at the preferred frequency in the K_s state was not larger than in the control state.

---

[3]I am grateful to Jean-Marc Fellous (The Salk Institute of Biological Studies, La Jolla, USA) who performed the experiments.
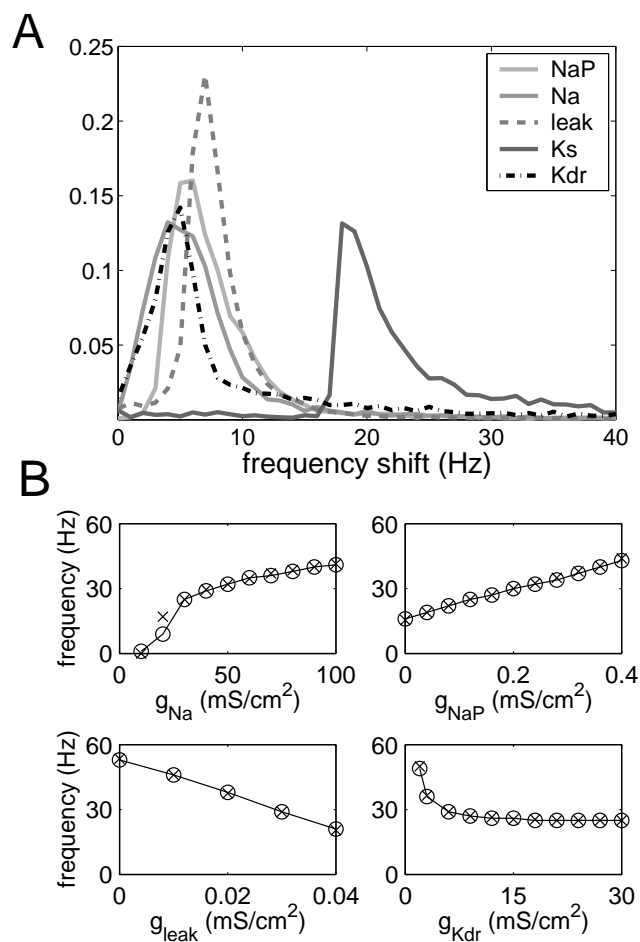
Figure 5.7: *Influence of parameter variation on the preferred frequency.* **A** *Normalized distribution of frequency shifts (maximum changes in firing rate) achievable by one ion channel type (measured over all combinations of the other four channel types). Cells in conductance space that do not fire are discarded. Different curves correspond to different ion channel types.* **B** *Four examples of cells where* Na, Na$_P$, L, *and* K$_{dr}$ *can mediate large changes in preferred frequency (for parameters see Appendix). Circles and solid lines indicate the preferred frequency derived with the sine wave protocol (C = 0.05 nA), crosses indicate the DC firing rate.*

Thus the experimental data confirm the influence of ion channels, specifically the influence of a slow potassium conductance, on spike timing reliability.
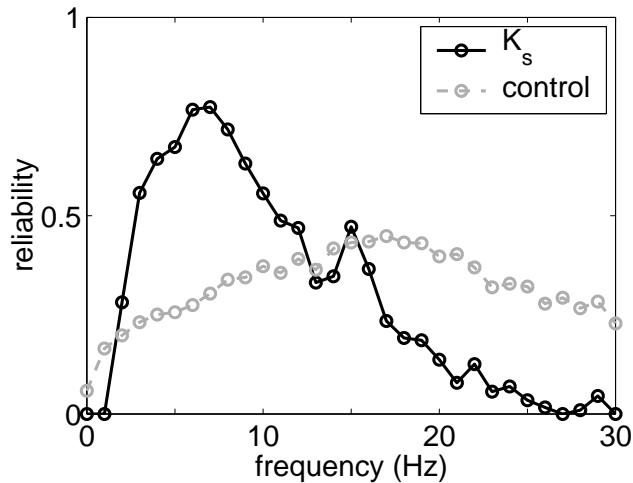
Figure 5.8: Reliability as a function of frequency for a cortical neuron. The gray curve shows reliability in the control case (no additional K_s present). The black curve shows reliability with dynamic clamp recordings, where additional amounts of K_s were present.

5.3 Reliability of inputs with more than one frequency

Many biologically relevant inputs are rhythmic, such as for example the input to CA1 pyramidal cells in hippocampus, which participate in the theta rhythm (Kamondi et al., 1998; Buzsaki, 2002). These inputs, however, are not well described by a single sharp peak in their power spectrum. They rather exhibit a broad distribution of power of frequencies. We therefore briefly test whether results obtained for modulation of spike timing frequency preference through ion channels can be extended from strictly periodic to more natural stimuli.

Model neurons are stimulated with quasi-random stimuli whose power spectrum contains two peaks of different amplitude: one in the theta-range (around 8 Hz) and one in the gamma range (30 Hz to 70 Hz). Three different stimuli are implemented, one of which has the dominant peak in the theta-range; the other two show the dominant peak in the gamma range (30 and 50 Hz, respectively). The characteristics of stimuli and their responses are depicted in Fig. 5.9.

Each stimulus is presented to a set of cells, which consists of reference model cells with different K_s conductance (as in Fig. 5.5B). The middle panels in Fig. 5.9 show that the reliability of the neuronal response depends on the amount of K_s present in a cell. For the theta-dominated input (Fig. 5.9A) cells with larger K_s conductances respond more reliably, whereas cells with lower K_s conductances (therefore tuned to higher frequencies) respond with lower reliability. For the two gamma-dominated stimuli, only cells with an optimally low K_s conductance achieve high reliability. A high K_s conductance makes the cell more unreliable.
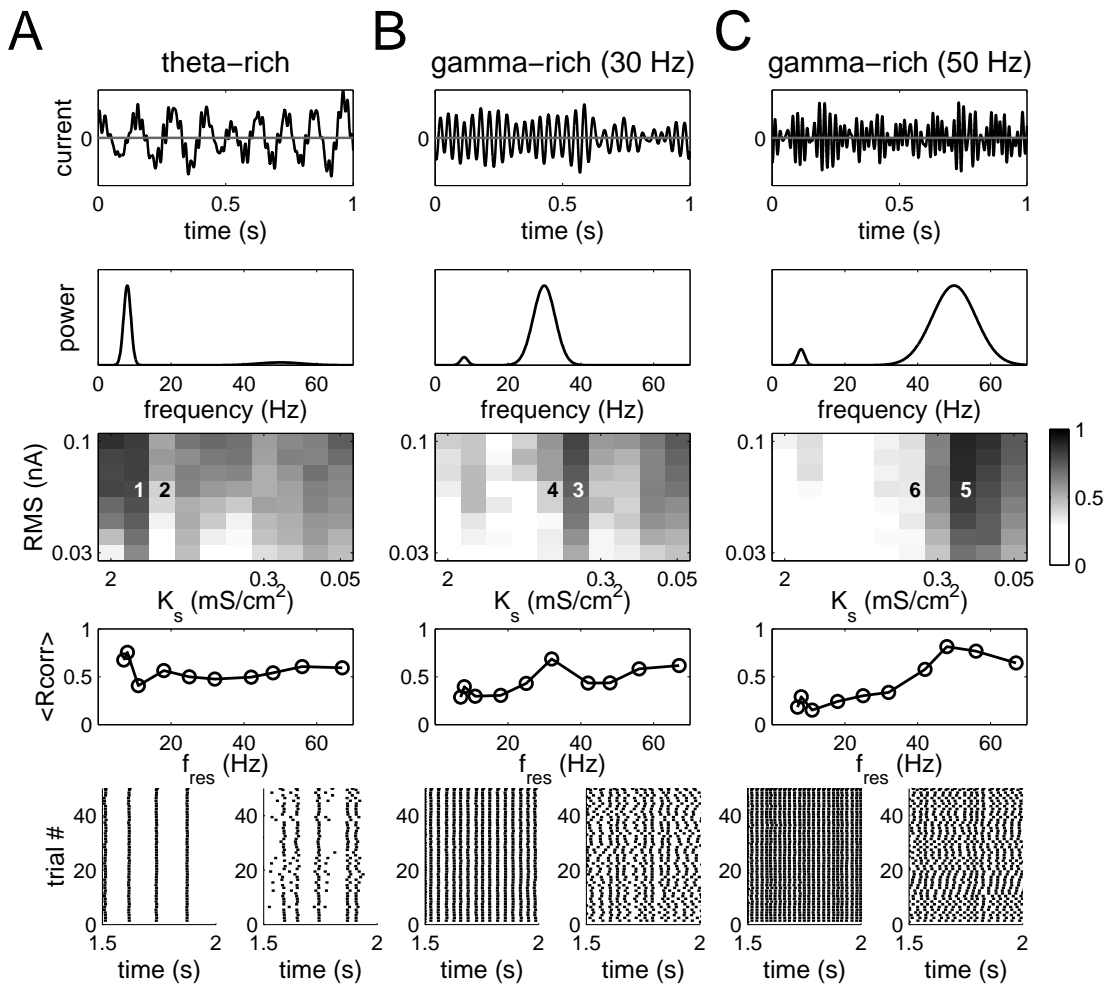
Figure 5.9: Spike timing reliability tested for three different inputs: a theta-dominated waveform (*A*), and two gamma-dominated waveforms (*B* and *C*). The uppermost panel in each column shows one second of the respective stimulus waveform. The second panel from the top shows the corresponding power spectrum. Below, gray-scale-coded reliability is presented as a function of the K_s conductance (horizontal axis) for 8 different RMS values of an input (0.03 nA to 0.1 nA, vertical axis). The panels above the rastergrams show reliability averaged over all RMS values as a function of the preferred frequency (corresponding to the K_s values). The bottom rastergrams show 500 ms of the responses at the numbered positions in the gray scale coded reliability panels (1 to 6 from left to right).

For all stimuli, the cell whose preferred frequency (adjusted by K_s) is closest to the dominant frequency in the input yields the highest spike timing reliability (as illustrated by the lower panels in Fig. 5.9). Interestingly, the second (smaller) peak in the power spectra of the inputs is also reflected by a small increase of reliability at corresponding densities of K_s. Not surprisingly, across all stimuli and cells reliability tends to increase with stimulus standard deviation

(or RMS value). Obviously, the results obtained with pure sine wave stimulation bear relevance for more natural rhythmic inputs.

Summary

Also in the suprathreshold regime a frequency-dependence of spike timing reliability exists. The preferred frequency is correlated to the firing rate in response to the pure DC component. In addition to the frequency band around the preferred frequency, where a 1:1 mode locking occurs, in the suprathreshold regime also conductance-based model cells show further frequency bands of high reliability, characterized by 1:2, 1:3 and 2:1 mode locking.

We have seen that properties of ion channels – their peak conductances as well as their kinetics – can directly determine the preferred frequency of spike timing reliability. Of the channels tested, the peak conductance of slow potassium channels has proven especially efficient in changing the preferred frequency over a broad range of frequencies. In particular, the size of the tunable range depends on the slow potassium time constant. We have demonstrated that in principle, adjustment of the ionic peak conductances, as can be achieved by neuromodulators, is suited for dynamic tuning of reliability frequency preference, as may be advantageous in view of changing stimulus statistic. Last but not least, experiments in slices of rat prefrontal cortex confirm the influence of slow potassium channels.

Chapter 4 and 5 have identified two separate mechanisms for the frequency preference of spike timing reliability, depending on the stimulus mean. It remains, however, to compare both regimes.

Chapter 6

Frequency preference of spike timing reliability

The aim of this chapter is to summarize and discuss the observations on spike timing frequency preference in the sub- and suprathreshold regimes. We will have a more detailed look at the frequencies that predict the spike timing reliability preference, and also review the ion channels suitable for regulation of frequency preference.

6.1 Relating sub- and suprathreshold regimes

As we demonstrated in the previous chapters, spike timing reliability depends on the stimulus frequency. The two main players determining the frequency preference of spike timing reliability are the subthreshold resonance frequency (below threshold) and the DC firing frequency (above threshold). An obvious question inflicted upon the reader is how the two frequencies compare close to the threshold, where both sub- and suprathreshold regimes coincide. Although we do not present a full analytical analysis of their relation, a systematic investigation of Morris-Lecar model neurons will help to gain some intuition.

6.1.1 Subthreshold resonance and bifurcation type

Before turning to spike timing reliability, we note that for any neuronal system described by two-dimensional differential equations, such as Morris-Lecar models, there is a relation between the local subthreshold resonance frequency at the threshold and the bifurcation type of the linearized system (and hence also of the nonlinear system): Cells exhibiting a Hopf bifurcation at threshold (type II dynamics) have a non-zero subthreshold resonance frequency near the threshold for small stimulus amplitudes. Conversely, cells that do not exhibit a Hopf bifurcation, i.e. in two dimensions have a saddle-node bifurcation (type I dynamics), do not have a subthreshold resonance near threshold. A proof of this statement is presented in Appendix C. For the Hopf bifurcation, the resonance frequency equals the imaginary part of the eigenvalue of the linearized system. For the saddle-node bifurcation, the imaginary part of the eigenvalue is zero and therefore the electrical impedance peaks at 0 Hz. The two (type I and type II) Morris-Lecar model neurons introduced in Chapter 4 illustrate this finding.

6.1.2   Spike timing in Morris-Lecar neurons

Fig. 6.1 summarizes the results obtained for the spike timing reliability of these two Morris-Lecar model neurons. Depending on the DC level, the corresponding subthreshold resonance frequency or the DC firing rate are good predictors of frequency preference.

Type I neurons, do not exhibit a subthreshold resonance near threshold, although they may show subthreshold resonance at other DC levels. The type I neuron presented in Fig. 6.1B shows no resonance at any DC level between rest and threshold. Thus, the preferred frequency for spike timing reliability is low. When crossing threshold, a type I neuron can exhibit arbitrarily low firing rates, which increase with the DC. The spike timing frequency preference follows this trend (see also the example of the nonresonant conductance-based model neuron in Chapter 4, Fig. 4.6).

Type II neurons, exhibit a subthreshold resonance at threshold and have a non-zero onset firing rate when crossing threshold. In the subthreshold regime, the subthreshold resonance frequency and the frequency at the maximum in the upper response envelope of ZAP stimuli approximate the preferred frequency (Fig. 6.1A). At the threshold (but not necessarily other DC levels), the resonance frequency and the frequency obtained from the upper response envelope coincide, because the stimulus amplitudes are very small. Both frequencies converge to the imaginary part of the eigenvalues of the linearized system at this point (see Appendix C).

It is tempting to suspect that the imaginary part of the eigenvalues of the linearized system at threshold also approximates the oscillation frequency of the limit cycle that emerges at the bifurcation point for the full nonlinear system. This would, for example, be true for a supercritical Hopf bifurcation. Morris-Lecar type II model neurons, however, show a subcritical Hopf bifurcation (Rinzel and Ermentrout, 1998). In this bifurcation, the fixed point loses stability and the limit cycle that emerges at the bifurcation point is unstable and inverted. The spikes arise from another stable and potentially distant limit cycle – which is the "only attractor in town" (Strogatz, 1994). Hence, the subthreshold resonance frequency and the oscillation frequency on this limit cycle (i.e. the DC firing rate) may not be similar. Thus a jump in the preferred frequency of spike timing can be expected at threshold, as can be seen for the neuron in Fig. 6.1A. The magnitude of the jump is a measure of how much the angular velocity of the system varies between the unstable fixed point and the stable limit cycle. For the sets of cells investigated here, the larger the size of the jump, the more type II a cell is, i.e. the larger the imaginary part of its eigenvalues at threshold.

   As the distant stable attractor appears before the fixed point loses stability, the subcritical bifurcation is accompanied by a region of bistability before the bifurcation. In this (typically small) region, both spiking and nonspiking behavior can be observed in response to a pure DC, depending on the initial conditions. The stable limit cycle is separated from the stable fixed point by the unstable limit cycle (or separatrix). Thus for these DC levels, a subthreshold resonance frequency exists as well as a DC firing rate. Which of the two frequencies determines spike timing reliability in this narrow DC region poses an interesting question in itself. It is, however, not discussed within the scope of this thesis, because it requires an exhaustive
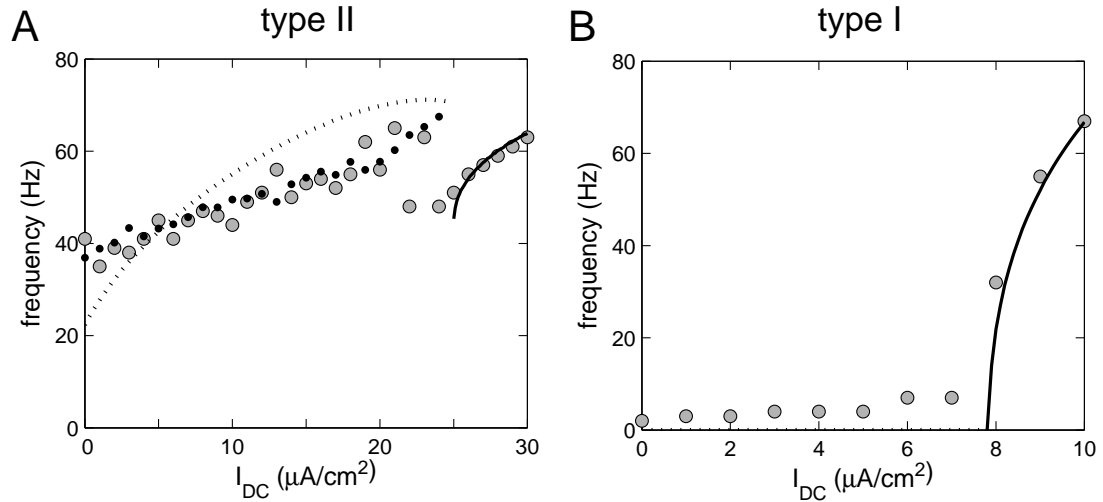
Figure 6.1: *Preferred frequency of spike timing reliability (gray circles) as a function of $I_{\rm DC}$ for a type II and a type I Morris-Lecar model neuron.* **A** *Type II neuron: Below threshold (at $24.9\,\mu A/cm^2$) the best frequency correlates with the subthreshold resonance frequency (dotted line), and is predicted well by the maximum of the upper response envelopes to large-amplitude ZAP currents (small black dots). Above threshold, the preferred frequency follows the DC firing rate (black solid line). A small jump in preferred frequency when crossing threshold is visible.* **B** *Type I neuron: Below threshold (at $7.8\,\mu A/cm^2$) the preferred frequency is low; the cell exhibits no subthreshold resonance. Above threshold the preferred frequency follows the DC firing rate (black solid line).*

exploration of all possible initial conditions and the relevance of this phenomenon for biology is likely to be small. We content ourselves with the discussion of an onset firing rate defined as the DC firing rate at the DC where the fixed point loses stability.

6.1.3 Frequency preference around the threshold

For a more systematic numerical investigation of these frequencies around threshold, 26 different Morris-Lecar model neurons were created. The type II and type I neuron presented above differ in the values of three parameters. These parameters were linearly interpolated, so that the first model neuron corresponds to the originally used type II neuron and the last model neuron corresponds to the originally used type I neuron (Fig. 6.1). Analytically-calculated subthreshold resonance frequencies and numerically-calculated firing rates as a function of $I_{\rm DC}$ are shown for four example neurons in Fig. 6.2A. Out of the 26 neurons, the first 19 neurons exhibit a subthreshold resonance at the threshold and change to the spiking regime via a Hopf bifurcation (type II). The bifurcation type can be determined by the analysis of the eigenvalues of the linearized systems, as is indicated for the example cells in Fig. 6.2B. The other 7 neurons show a saddle-node bifurcation (type I) and are nonresonant at threshold, as is the last cell of Fig. 6.2B.

The relation between the subthreshold resonance frequency just below threshold and the onset firing rate just above threshold is presented in Fig. 6.3A. The neurons of type I show
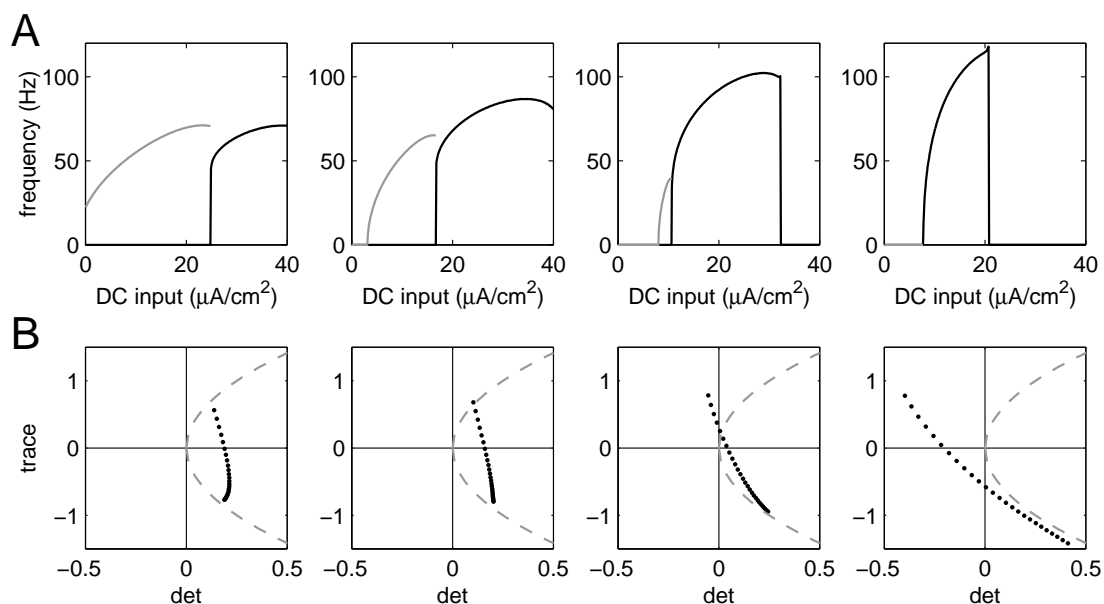
*Figure 6.2: DC firing rate (black solid line) and subthreshold resonance frequency (gray solid line) as a function of I_{DC} for different Morris-Lecar neurons. **A** Three type II model neurons and one type I model neuron (left to right). All type II neurons show nonzero onset firing rates and a subthreshold resonance at the threshold. The type I neuron exhibits arbitrarily low firing rates when crossing threshold and shows no subthreshold resonance. The cells were derived by linear interpolation of three parameters (see Appendix B). Note that the decrease in DC firing rate back to zero visible in the two righthand examples arises from a second bifurcation, not discussed here. If the DC is too large, the cell stops firing and settles onto a new steady-state voltage. **B** Determinant and trace of the values of the matrix of eigenvalues of the corresponding linear system (black dots). The gray dashed line separates the area of complex eigenvalues from the area of real eigenvalues. A Hopf bifurcation (type II neuron) occurs when the black dots cross the (horizontal) line of zero trace at positive values of the determinant, as is the case for the first three neurons. A saddle-node bifurcation (type I) occurs when the black dots cross the (vertical) line of zero determinant at negative values of the trace, as in the fourth cell.*

an impedance maximum at 0 Hz (marked as a resonance frequency of 0 Hz) and very low onset firing rates (white symbols). The neurons of type II (gray and black symbols) all exhibit an onset firing rate significantly different from 0 Hz. The onset firing rate is close to the subthreshold resonance frequency, though the subthreshold resonance frequency surpasses the firing rate in all cases. It should be noted that values determined numerically do not necessarily reflect the subthreshold resonance frequency *at* the threshold. Morris-Lecar neurons with parameters near the border between type I and type II show a resonance frequency that, close to threshold, sharply decreases as a function of the DC. In these cases it is not guaranteed that this behavior is resolved numerically, due to the finite sampling of DC levels. The consequences for spike timing reliability in these neurons should, however, be negligible, because only a very small DC region (in fact smaller than the DC resolution of $0.5\,\mu\mathrm{A/cm}^2$) is affected.

Interestingly, similar results can be obtained for conductance-based cells. The same analysis
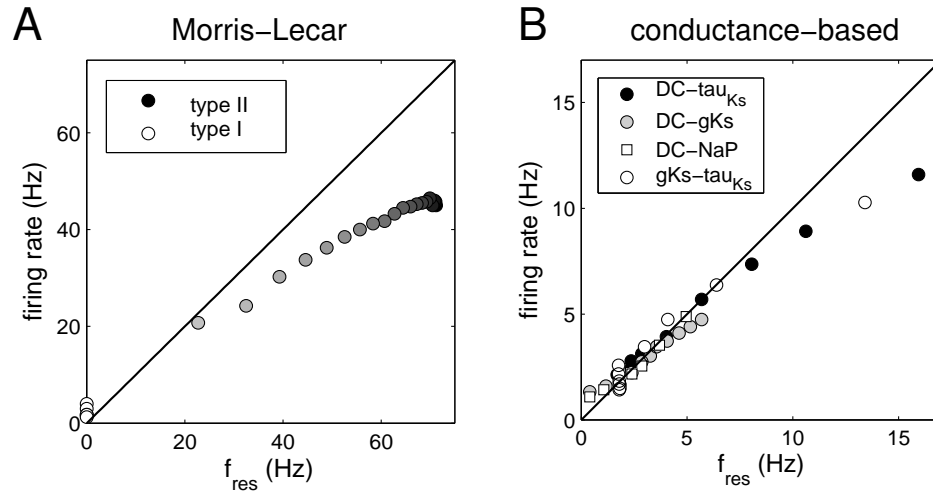
*Figure 6.3: Onset firing rate (just above threshold) and subthreshold resonance frequency just below threshold. **A** 26 Morris-Lecar model neurons, differing in the value of three parameters such that the set gradually changes from type II (black and gray circles) to type I (white circles) neurons. The onset firing rate correlates with the subthreshold resonance frequency just below threshold. The larger the value of the resonance frequency, the more the resonance frequency surpasses the onset firing rate. **B** The same analysis for different sets of conductance-based model cells, showing a strong correlation between both frequencies. The subthreshold resonance frequency tends to be larger than the onset firing rate. Note that due to the limited resolution of the DC steps (0.001 to 0.0025 nA, depending on the model set) the depicted values for the onset firing rate represents an upper bound. For example, it cannot be excluded that the true values of the white symbols are below the equality line.*

for four sets of conductance-based cells differing in the peak conductances of individual ion channel types or in the kinetics of some ion channels (as marked in the legend) is presented in Fig. 6.3B.[1] Firing rate and subthreshold resonance frequency correlate very well. As for the Morris-Lecar neurons, the subthreshold resonance frequency tends to surpass the onset firing rate for larger frequencies.

Altogether, the analysis of Morris-Lecar neurons and conductance-based neurons suggests that at threshold jumps in the preferred frequency of spike timing reliability can occur, depending on the characteristics of the system. The shifts in frequency preference around threshold illustrated in this chapter are relevant for the integration of small-amplitude stimuli. For larger stimulus amplitudes, however, nonlinear interactions between the sub- and suprathreshold regime can be expected, which are likely to have further effects on how the preferred frequency changes from the subthreshold to the suprathreshold regime.

---

[1]These particular sets of conductance-based cells will be of further interest in the following and last chapter on spike timing reliability. For the moment, however, we only explore their behavior close to threshold.

6.2   Comparison of sub- and suprathreshold spike timing

What have we learned about frequency-preference of spike timing reliability? First of all, two different regimes, depending on the level of depolarization and thus also on the DC component of the stimulus have to be distinguished: sub- and suprathreshold mean stimuli. From a biophysicist's point of view the scenarios can be described as follows: *In the subthreshold regime*, the neuron has a stable fixed point, i.e. a fixed steady state voltage determined by the stimulus mean. Nevertheless, the time-dependent component of the stimulus constantly drives the input away from this fixed point, sometimes with excursions large enough to send the neuron on the trajectory of a spike. *In the suprathreshold regime*, the situation is qualitatively different. Even in the absence of the time-dependent stimulus component the neuron circles on the trajectory of a stable limit cycle and thus periodically elicits spikes. The time-dependent component drives the neuron away from the limit cycle, delaying or advancing the neuron on the limit cycle.

6.2.1   Similarities

Nevertheless, sub- and suprathreshold regimes have many properties in common: Frequency selectivity of spike timing can be observed in both regimes, each determined by an intrinsic frequency - either the subthreshold resonance frequency (assumed to be 0 if a resonance is not present) or the DC firing rate. Both frequencies *per se* depend on the DC, and both are tunable by intrinsic conductances and their kinetics. Some ion channel types are efficient in adjustment of frequency preference in the sub- and suprathreshold regime, such as the potassium channels with slow kinetics. For stimuli of sub- and suprathreshold mean reliability increases with the RMS value of the stimulus (i.e. the amplitude of the time-dependent component). In both regimes, noise lowers the reliability.

6.2.2   Differences

There are also fundamental differences in the reliability of responses, depending on the stimulus mean. For stimuli of subthreshold mean, decreased reliability is dominated by missing and additional spikes, while the timing of individual spikes may be rather precise. For stimuli of suprathreshold mean, reduced reliability is mainly reflected in the jitter of individual spikes, while spikes are rarely missing completely. Equally, a larger dependence of the average firing rate on the stimulus frequency is observed for subthreshold mean stimuli.

These observations can also be understood intuitively: For stimuli with a mean below threshold, only when the time dependent component approaches threshold, spikes can be elicited. The "temporal window" for spikes is limited by the structure of the stimulus. In addition, in this regime it is quite often the stimulus uncorrelated noise which determines, whether or not the stimulus crosses threshold and a spike is actually fired. For stimuli above threshold, however, noise only changes the phase of the oscillation (i.e. advance or delay the spike).

Another difference concerns the influence of nonlinearities. Because from DC levels close to rest large amplitudes are required to elicit spikes in the first place, nonlinearities play a larger

role in this (subthreshold) DC range.

Last but not least, in conductance-based model neurons we saw that only in the suprathreshold regime (or just below threshold) reliability is increased for stimuli at the harmonics or subharmonics of the preferred frequency. This lack of multiple regions of increased reliability in the subthreshold regime could, however, not be confirmed for Morris-Lecar type neurons. Which of the two behaviors is adopted by real neurons remains to be tested.

6.3 The role of ion channels

From a mechanistic discussion of the spike timing frequency preference, we now briefly review the ion channels analyzed in this work and their influence on frequency preference.

6.3.1 Potassium channels

Within the framework of this study, the most prominent role in the sub- as well as the suprathreshold regime has to be assigned to potassium channels. Humans have over 70 potassium channel genes (Jentsch, 2000), which - considering splicing - can be turned into an even higher number of different potassium channels. The most common functional class of potassium channel are the delayed rectifiers, which are activated with a delay after a depolarizing voltage step. These channels are known to regulate pacemaker potentials as well as overall excitability (Hille, 2001). Their activation time constants span several orders of magnitude. Thus the activation kinetics of the slow potassium channel in the heart are 1000 times slower than in frog nodes of Ranvier. In addition, potassium channels are regulated dynamically by a multitude of cellular signals and neuromodulators, examples of which are cAMP-dependent phosphorylation of slow potassium channels in the heart or regulation of muscarinic potassium channels through acetylcholine.

We find that among the potassium channels those with slow kinetics have the greatest effect on the frequency preference of spike timing reliability. In the suprathreshold regime, the ability of K_s to control the inter-spike-interval during repetitive firing makes slow potassium channels ideal candidates for regulation of the preferred frequency. As we saw in the previous chapter, changes in K_s conductance are most efficient in adjusting the DC firing rate and thus spike timing frequency preferences. In the subthreshold regime, K_s suppresses the response to slowly varying stimuli and thus is instrumental in shaping the subthreshold resonance. Slower potassium channel kinetics lead to lower preferred frequencies, while the preferred frequency increases with faster kinetics (White et al., 1995). In the sub- as well as the suprathreshold regime, the presence of slow potassium channels limits the ability of other ion channels to tune the preferred frequency.

6.3.2 Sodium channels

In contrast to potassium channels, sodium channels are less diverse. They are responsible for the rapid regenerative upstroke of an action potential. They also contribute to pacemaker and subthreshold potentials that underlie decisions to fire or not to fire. As the firing rate

usually increases with the Na peak conductance, sodium channels can tune the frequency preference in the suprathreshold regime. The ability of sodium channels to modulate the firing rate, however, depends strongly on the presence of slow potassium channels. Only if the $\mathrm{K_s}$ conductance is relatively low, can sodium channels efficiently change preferred frequency. In the subthreshold regime, the influence of sodium channels on frequency preference is smaller. The persistent sodium channel is known to act as an amplifier of subthreshold resonance (Hutcheon and Yarom, 2000). The location of the subthreshold resonance in frequency space, however, depends more strongly other channels, such as H and $\mathrm{K_s}$, than on $\mathrm{Na_P}$.

6.3.3 H and leak channels

In contrast to the sodium and potassium channels used in this study, H channels activate slowly upon hyperpolarization. They are almost as permeable to Na^+ as to K^+ ions, with a reversal potential at depolarized voltage levels (here -43 mV). Thus they initiate slow depolarization if the membrane potentials become negative. The analysis of spike timing reliability suggests that H channels help to set the preferred frequency of spike timing reliability at hyperpolarized membrane potentials and close to rest. As they serve to stabilize the subthreshold resonance frequency (as described in chapter 2), they also can help avoid a dependence of the preferred frequency on stimulus amplitude (for a given DC). A significant role of H in modulating the preferred frequency could not be confirmed in the suprathreshold regime (data not shown).

Last but not least, leak channels influence frequency preference. They provide a small, relatively voltage-independent background conductance. In the subthreshold regime they are essential for shaping the subthreshold resonance by suppressing the response to high-frequency components of the stimulus. In the suprathreshold regime, increasing the leak conductance results in lower firing rates. Therefore, they can, in principle, regulate the frequency preference. As for the other channels, their effect is decreased in the presence of slow potassium.

Summary

Although the mechanisms responsible for the frequency preference of spike timing reliability are different in the sub- and suprathreshold regime, they show many similarities. Most importantly, both mechanisms are based on a resonance between the stimulus frequency and the intrinsic neuronal dynamics. At threshold, where both regimes "meet", deviations between the two resonance frequencies can be observed. In the examples presented here, however, these deviations were relatively small. The most prominent difference between both regimes is the contribution of missing and additional spikes versus spike timing jitter to decreases in reliability. While unreliable responses in the subthreshold regime show a large amount of missing and some additional spikes, the timing jitter is dominant in the suprathreshold regime. It is important to notice that in both regimes the frequency selectivity is tunable by ion channels, the most prominent ion channels investigated in this study being the slow potassium channels.

These channels also have a third effect on spike timing reliability, as we will see in the following chapter.

Chapter 7

Ion channels influence the sensitivity to noise

The previous chapters have shown in detail how neurons can adjust their frequency preference of spike timing reliability. In the suprathreshold regime, however, adjustment of the preferred frequency comes at the cost of a change in the average firing rate. In this chapter we demonstrate how ion channels can influence spike timing reliability *without* changing overall excitability: how ion channels directly set the sensitivity of neuronal responses to noise.[1]

7.1 Differential reliability despite the same preferred frequency

In the regime of suprathreshold stimulus mean, the preferred frequency of spike timing reliability is determined by the DC firing rate. Equal firing rates and consequently equal preferred spike timing frequencies can, however, be achieved under various conditions. Thus cells with different compositions of conductances can have the same DC firing rate at a given DC level. Does that mean that spike timing reliability of both cells to a given stimulus is equal? The answer is no. Even for cells with equal preferred frequency there are fundamental differences in spike timing reliability. In the following we will show the differential spike timing reliability and relate the reliability to the composition and kinetics of ionic channels.

7.1.1 Variation in the slow potassium channels

First, we create a set of cells with the same preferred frequency at a given DC level, but different time constants, τ_{Ks}, and different peak conductances, $\bar{g}_{\mathrm{Ks}}$, of the slow potassium channel. For each cell, the time constant of the slow potassium channels is set and the K_s peak conductance is adjusted such that the DC firing rate (in response to $I_{\mathrm{DC}}=0.3\,\mathrm{nA}$) equals 20 Hz. All other conductance parameters remain those of the reference cell introduced in Chapter 5. Arnold plots obtained from responses to a set of sine wave stimuli (the same for each cell) are shown in Fig. 7.1. These plots confirm that all cells in the set have the same preferred frequency.

The most interesting observation, however, is a systematic difference in the value of reliability at the preferred frequency, in the width of the 1:1 Arnold tongue, as well as in the values of spike timing reliability at the harmonic frequencies (1:2 and 1:3 Arnold tongues). The absolute value of reliability at the preferred frequency and its harmonics increases significantly

---

[1]This chapter is in part adapted from Schreiber *et al.* (2004b).
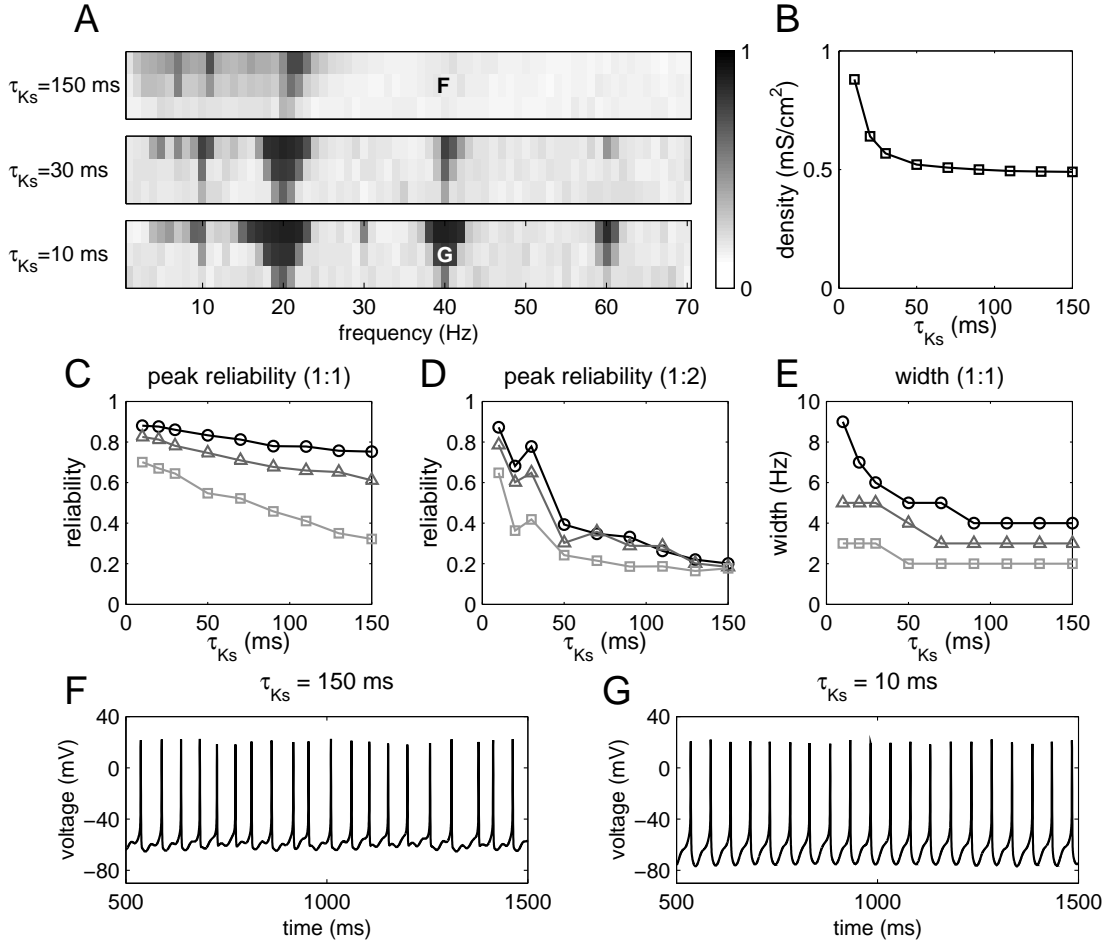
Figure 7.1: Differential reliability at identical preferred frequencies. **A** *Arnold plots for examples of three cells differing in the values of τ_{Ks} (as indicated) and slow potassium peak conductance, $\bar{g}_{Ks}$.* **B** *$\bar{g}_{Ks}$ was adjusted such that all cells had a DC firing rate of 20 Hz, i.e. the same preferred frequency.* **C** *Peak reliability at the preferred frequency (1:1 mode locking) as a function of τ_{Ks} for the three different amplitudes of the sine component.* **D** *Peak reliability at the first harmonic (1:2 mode locking). For panels C and D the standard deviation of the reliability estimate was smaller or equal to the symbol size.* **E** *Width of the reliability peak around the preferred frequency. Measured as the width (in Hz) at 50 % height in between the peak and background reliability levels (mean of reliability from 27 to 29 Hz). The standard deviation of the estimate was never bigger than 1 Hz for all points presented. The plateaus are due to the 1 Hz discretization of the frequency axis.* **F** *and* **G** *Sample voltage traces of neurons with a slower and a faster potassium channel, respectively (see labeling in panel A). The input to both cells has a frequency of the first harmonic (1:2 mode locking). Noise is identical for both cells.*

with decreasing τ_{Ks}, i.e. faster kinetics and higher values of $\bar{g}_{Ks}$ (Fig. 7.1C and 7.1D). This effect is more pronounced at the first harmonic of the preferred frequency, despite a small deviation from the general trend around $\tau_{Ks}=25$ ms. The width also increases with faster

kinetics and larger values of $\bar{g}_{\mathrm{Ks}}$. In addition, Fig. 7.1F and 7.1G show the voltage traces at the first harmonic for $\tau_{\mathrm{Ks}}=10$ ms and $\tau_{\mathrm{Ks}}=150$ ms. The rise in reliability with larger and faster $\mathrm{K_s}$ conductance is accompanied by a deepening of the afterhyperpolarization following a spike (see Fig. 7.1) and a more efficient shut down of sodium currents after a spike (data not shown). Similar results were obtained for a set of cells with a preferred frequency of 8 Hz (data not shown).

7.1.2 Influence of slow potassium kinetics and peak conductance

In order to distinguish the contribution of the peak conductance and the time constant of the slow potassium channel to the differential reliability, two more sets of neurons with a preferred frequency of 20 Hz are analyzed. Cells in the first of these sets vary in the $\mathrm{K_s}$ peak conductance. This time, the DC current, I_{DC} is adjusted to keep the firing rate at 20 Hz. Cells in the second of these sets differ in the time constant τ_{Ks}. Again, adjustment of I_{DC} keeps the firing rate constant. The amplitude of the sine wave components of the input, however, remain the same for all cells.

Fig. 7.2A shows a significant increase of reliability at the preferred frequency with increasing potassium peak conductance. This observation can be made at all three stimulus amplitude levels. In addition, the width of the reliable region around the preferred frequency increases with $\bar{g}_{\mathrm{Ks}}$ (Fig. 7.2D). Note that for low values of $\bar{g}_{\mathrm{Ks}}$, the curves are nonmonotonic. For these values, the difference between the peak reliability and that at surrounding frequencies is very small, which as a consequence broadens the estimate of width at the preferred frequency.

From Fig. 7.2B and 7.2E it is obvious that also the $\mathrm{K_s}$ time constants influence spike timing reliability at the preferred frequency. Apart from a shallow maximum around $\tau_{\mathrm{Ks}}=30$ ms, the general trend confirms that faster $\mathrm{K_s}$ channels increase the peak conductance and broaden the width. Overall, the effect of the $\mathrm{K_s}$ peak conductance is higher than that of the time constant.

7.1.3 The influence of persistent sodium channels

Slow potassium channels are not the only channel types whose peak conductance and kinetics influence spike timing reliability. Fig. 7.2C and 7.2F illustrate that also persistent sodium channels, $\mathrm{Na_P}$, modulate reliability. Again, a set with a preferred frequency of 20 Hz was created by adjusting I_{DC}. For persistent sodium channels, the effect on reliability is opposite to that of slow potassium. The larger the $\mathrm{Na_P}$ peak conductance, the more sensitive a cell is to noise and the less reliable is the response to a given stimulus. Even more pronounced is the effect of $\mathrm{Na_P}$ on the width of the 1:1 Arnold tongue. The more $\mathrm{Na_P}$ is present, the narrower is the band of increased reliability around the preferred frequency.

7.2 Sensitivity to noise

The observation that certain ion channels have a pronounced effect on reliability beyond an influence on the preferred frequency of spike timing reliability can be attributed to a change in the sensitivity to noise. In support of this hypothesis we also analyze the response of the neurons to pure DC stimuli.
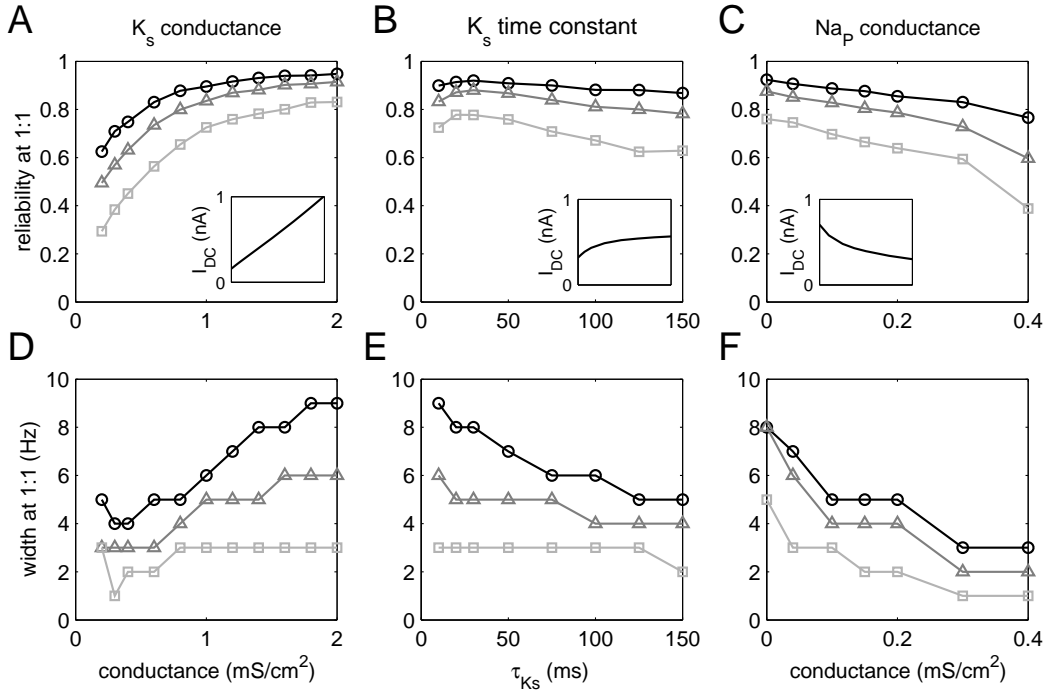
Figure 7.2: Influence of $\bar{g}_{Ks}$, τ_{Ks}, and $\bar{g}_{NaP}$ on reliability at the preferred frequency. Peak reliability at the preferred frequency is presented for neurons differing in $\bar{g}_{Ks}$ (**A**), τ_{Ks} (**B**), and $\bar{g}_{NaP}$ (**C**). Different curves correspond to different amplitudes of the sine component. The standard deviation of the reliability estimate does not exceed the symbol size. The insets indicate how the DC is adjusted to keep the firing rate constant (the x axis of the insets is equal to that of the respective panel). The lower panels (**D**-**F**) depict the widths of the 1:1 reliability peak. The standard deviation of this estimate was never larger than 1 Hz. Altogether, more and faster K_s channels enhance reliability, while Na_P channels impair reliability.

7.2.1   The DC response

When the stimulus consists only of the DC component, I_{DC}, one cannot expect a neuron to respond reliably (apart from a brief transient period directly after stimulus onset). The explanation is straightforward: Because there is no time-dependent stimulus component, the response will not lock to the stimulus, but to the noise. The noise, however, is different in each trial so that decorrelation of spike times occurs for times long after stimulus onset. Thus one would predict that the above described sets of cells do not show a difference in the reliability of response segments long after stimulus onset (steady-state reliability). On the other hand, one would expect a difference in the time that it takes to reach the steady-state reliability, i.e. in the time it takes to decorrelate the initially precise spikes – if the differential reliability within the above described sets can be attributed to a differential sensitivity to noise. Indeed, Fig. 7.3 shows clearly that the cells of the $\bar{g}_{Ks}$-τ_{Ks} set take different times to reach the steady-state reliability (equal for all cells). Reliability is estimated from 500 ms long response segments, every 10 ms after stimulus onset. The reliability trend within the set observed at the preferred

frequency and the harmonics (in the previous section) also is visible for pure DC stimulation. The faster the slow potassium channels and the larger their peak conductance, the longer reliability values above the steady-state reliability are maintained after stimulus onset. The effect of these channels is not constrained to the preferred frequency, but can be attributed to a general change in the sensitivity of the responses to noise.
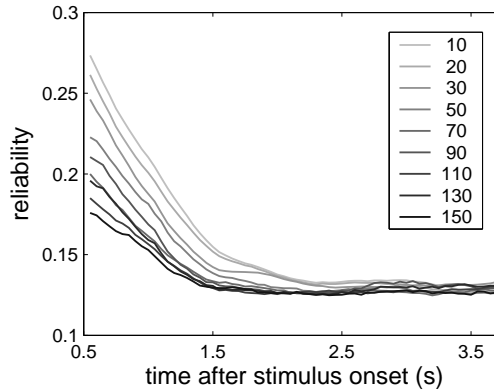
Figure 7.3: *Reliability in response to pure DC stimuli (I_{DC}=0.3 nA) as a function of time after stimulus onset. Different curves correspond to different cells distinct in their K_s peak conductance and K_s time constant (on the basis of the same cell set as in Fig. 7.1). The legend marks the time constant, τ_{Ks}, in ms. Time-dependent reliability was estimated from a 500 ms long gliding window (every 50 ms). The first 500 ms after stimulus onset were discarded from analysis. Although all cells eventually settle on the same low value of reliability, a significant difference in the first second after stimulus onset and transient can be observed. Similar to the effect at the preferred frequency, faster K_s channels with higher peak conductance show improved robustness to noise.*

7.2.2 Phase-resetting curves

A cell's sensitivity to noise is also reflected in so-called phase-resetting curves. Phase resetting curves describe the influence of brief perturbation pulses on the occurrence of the following spike, while the cell is in a regular firing mode under pure DC stimulation, see for example (Ermentrout, 1996). Short current pulses are given in addition to the DC stimulus at various times after a selected spike. The resulting shift in the occurrence time of the following spike as a function of the time the pulse was presented defines the phase-resetting curve.

Fig. 7.4A shows phase-resetting curves for the set of cells with varying K_s peak conductance (presented in Fig. 7.2A). For cells with low $\bar{g}_{Ks}$, a perturbation directly after the spike significantly advances the following spike. Whereas for cells with high $\bar{g}_{Ks}$, the perturbation has almost no effect on the timing of the following spike. The effect of perturbations presented in the last third of the unperturbed inter-spike interval (ISI) is relatively independent of $\bar{g}_{Ks}$.

The other panels of Fig. 7.4 show similar results for all cell sets presented above. The data indicate that the K_s time constant and the Na_P peak conductance influence the phase-resetting curves. For all cell sets the trend is equal: The change in parameters that was found to increase spike timing reliability also lowers the influence of perturbations on spike timing.
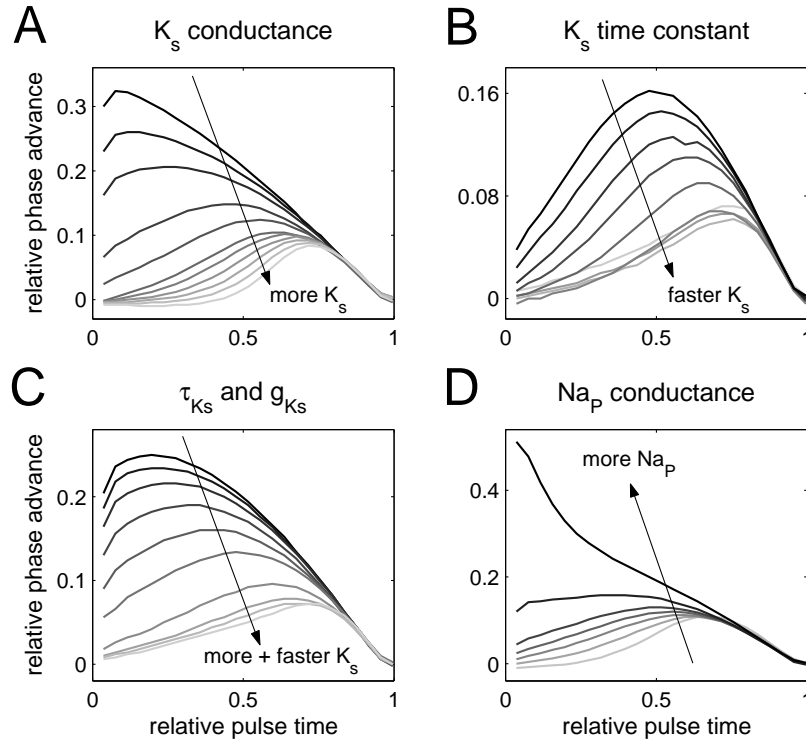
Figure 7.4: The dependence of phase-resetting curves on different cell parameters. **A** *Different curves correspond to different values of $\bar{g}_{Ks}$, from the set of cells shown in Fig. 7.2A. The larger $\bar{g}_{Ks}$, the lower the influence of small perturbations on the timing of the following spike, especially for perturbations shortly after the first spike. Similar observations can be made for the sets of neurons with different K_s time constant (**B**), different K_s time constant and $\bar{g}_{Ks}$ (**C**) and different Na_P peak conductance (**D**). Overall, the trends are the same as those observed for spike timing reliability. Some phase-resetting curves show small negative values (like the light-gray curves in A). Most of the time, however, the pulses cause a phase advance (i.e. positive values of the phase-resetting curve). The largest influence of cell parameters on the timing of the following spike is exerted in the first half of an ISI. The perturbation pulses had a duration of 2 ms and an amplitude of 0.3 nA.*

Even the small peak for the set of τ_{Ks} variation can be found in the phase-resetting curves; the phase-resetting curve for the fastest K_s conductance is larger that of the next slower ones (Fig.. 7.4B).

7.2.3   A relation between phase-resetting and timing jitter

Finally, we briefly establish a relationship between phase-resetting curves and spike timing reliability. Because in the suprathreshold regime, unreliability predominantly arises from the jitter in the timing of spikes, reliability is lowered to the extend to which noise between spikes can shift the following spike. Now the noise between two spikes can be considered as a time-dependent perturbation, $\Delta I(\psi)$, where ψ denotes the phase (or time normalized to the the

average inter-spike interval of the unperturbed system). ψ is therefore constrained to the interval [0;1]. In a linear regime of integration - i.e. for *noise of small amplitude* - the influence of the noise $\Delta I(\psi)$ on the timing jitter, Δt, of the second spike can be approximated by

$$\Delta t \approx - \int_0^1 \mathrm{d}\psi \, z(\psi)\Delta I(\psi), \tag{7.1}$$

where $z(\psi)$ is the phase-resetting curve (Ermentrout, 1996; Benda and Herz, 2003). In the case of zero-mean, white Gaussian noise, the average Δt is zero. What matters for the reliability, however, is the variance, $\sigma^2_{\Delta t}$, of Δt:

$$\sigma^2_{\Delta t} \approx \left\langle \left(\int_0^1 \mathrm{d}\psi \, z(\psi)\Delta I(\psi) \right)^2 \right\rangle_{\Delta I} \tag{7.2}$$

$$= \int_0^1 \int_0^1 \mathrm{d}\psi \mathrm{d}\psi' \, z(\psi)z(\psi')\left\langle \Delta I(\psi)\Delta I(\psi') \right\rangle_{\Delta I}. \tag{7.3}$$

Because the noise terms are uncorrelated,

$$\langle \Delta I(\psi)\Delta I(\psi') \rangle_{\Delta I} = \sigma^2_{\mathrm{I}} \, \delta(\psi - \psi'), \tag{7.4}$$

where σ_{I} is a constant that relates to the noise variance. Thus the timing variance, $\sigma^2_{\Delta t}$, reads

$$\sigma^2_{\Delta t} \approx \sigma^2_{\mathrm{I}} \int_0^1 \mathrm{d}\psi \, \mathrm{z}^2(\psi), \tag{7.5}$$

and therefore depends on the area under the squared phase-resetting curve, $z^2(\psi)$. Thus the timing jitter (and consequently unreliability) increase with the area under the squared phase-resetting curve.

7.3 Potassium and persistent sodium channels

Several lines of evidence presented in this chapter support the hypothesis that potassium channels and persistent sodium channels can control the sensitivity to noise when a cell is in regular firing mode. This observation is independent of the frequency-dependence discussed in the previous chapters.

The most important property of potassium channels is that they counteract depolarization. Thus the responsiveness of a cell is reduced in the presence of a large potassium conductance, especially directly after a spike, when the potassium channels are most active, as the phase-resetting curves in Fig. 7.4A indicate. Consequently, the cell is less sensitive to noise. An additional effect leading to insensitivity is the inactivation of Na channels after a spike. We observed that cells with larger $\mathrm{K_s}$ conductances also were characterized by a more efficient shut down of sodium channels after a spike (data not shown).

We also find that cells with faster $\mathrm{K_s}$ channels have more reliable responses than cells with slower $\mathrm{K_s}$ channels. A possible explanation is that neural noise (as well as the noise used in this study) is relatively fast and needs fast channels to follow the time course and

counteract depolarization (according to the same principle that underlies amplitude attenuation in subthreshold resonance). One speculation is that the small peak in the effect of the kinetics on reliability (see for example Fig. 7.2B), reflects a trade-off between long-lasting insensitivity after a spike (due to slow kinetics) and the ability to attenuate high-frequency noise.

In general, the strong activation of fast K_s channels after a spike is manifested in a deep afterhyperpolarization, as we observed in cells with a large and fast K_s conductance in contrast to cells with low and slow K_s conductance (see for example Fig. 7.1F and 7.1G). It is worthwhile to note, however, that in general the degree of afterhyperpolarization alone is not sufficient to infer reliability, because lower voltage values after a spike do not exclude an equally increased sensitivity to signals in the inter-spike interval.

Finally, the effect of persistent sodium channels on reliability can be easily understood. These channels do not inactivate and thus help boost depolarizing signals and directly increase sensitivity to noise. Interestingly, similar ion channels – slow potassium and persistent sodium - have recently been found to determine the state of synchrony in neural networks (Pfeuty et al., 2003). The trend is the same: slow potassium channels promote synchrony and persistent sodium channels impede synchrony.

Summary

The analysis in this chapter has shown that individual ion channels and their kinetics can influence reliability without changing the firing rate or the preferred frequency. Although the effect is most obvious for stimuli with frequencies at the harmonics of the preferred frequency, it is not exclusive for periodic inputs. It rather reflects a general decrease in the sensitivity to noise, which results in more precise spikes. Support for this hypothesis comes from pure DC stimulation, where we saw that cells with more and faster slow potassium channels channels could maintain initially high values of reliability over a longer period of time. Also the analysis of phase-resetting curves indicates that ion channels selectively influence the sensitivity of spike timing to noise. Altogether, the regulation of the sensitivity to noise through ion channels provides a second mechanism controlling spike timing reliability, in addition to the adjustment frequency preference.

Chapter 8

Conclusions and outlook

We followed three major lines of investigation in this thesis. They relate frequency-selectivity, spike timing reliability and the influence of intrinsic neuronal parameters:

1. The frequency selectivity of subthreshold response amplitudes has been proven to extend to nonperiodic stimuli and to translate into firing rates.

2. The mechanisms leading to frequency preference of spike timing reliability have been elucidated and the capacity of specific ionic conductances to modulate the frequency preference have been shown.

3. A direct influence of ion channels on the sensitivity of the timing of spikes to noise has been demonstrated.

In the first part, comprising the chapters 2 and 3, subthreshold resonance has been introduced as a mechanism leading to frequency-selective signal integration. We have shown that although subthreshold resonance profiles are usually characterized on the basis of periodic signals, they equally affect responses to nonperiodic stimuli, such as frozen colored noise. The analysis presented here thus provides an alternative view to previous experiments that suggested a nonlinear interpretation of the integration of nonperiodic signals.

Interestingly, for stellate and pyramidal cells of the entorhinal cortex, the integration of periodic and nonperiodic graded signals follows the rules of a linear system and there is no need to assume additional and selective nonlinear mechanisms. Hence, our results also suggest that the occurrence and frequency of spontaneous subthreshold oscillations in the presence of a subthreshold resonance may be quantitatively explained by a simple filtering operation acting on intrinsic channel noise, see also (White et al., 1998). Whether this relation holds quantitatively, remains to be tested. The translation of the subthreshold frequency selectivity to a frequency-dependent firing rate observed here, may be exploited in the frequency-dependent flow of information, as suggested previously (Gloveli et al., 1997).

Finally, it is important to notice that subthreshold resonance is shaped by intrinsic currents, as discussed widely in the literature, see for example (Hutcheon et al., 1996b; Hutcheon and Yarom, 2000; Hu et al., 2002). The modeling of stellate cells in entorhinal cortex has

shown that in principle the presence of H and M currents (in addition to the usual Na, K, and L currents) is enough to achieve a subthreshold resonance profile that is independent of the membrane potential, for a large range of voltages.

In the second part, comprising the chapters 4 to 6, we have followed up on the previous observation that spike timing reliability can depend on the stimulus frequency. The mechanisms leading to a frequency selectivity of spike timing reliability and the ability of intrinsic currents to tune this preference have been analyzed.

For the first time, two regimes determined by the relation of the DC to the firing threshold have been distinguished clearly and the role of subthreshold resonance for the spike timing of rhythmic inputs has been elucidated. Nonlinear effects have been shown to act on large-amplitude ZAP currents and to influence spike timing reliability in the subthreshold regime.

In the suprathreshold regime, a mechanism leading to frequency selectivity of spike timing had been suggested before (Hunter et al., 1998). We have confirmed that this resonance effect is also observed in conductance-based model neurons and have focussed on the identification of ion channels that can tune the preferred frequency. The peak conductance of potassium channels with slow kinetics, which may be adjusted on short time scales by neurotransmitters, has proven efficient to modulate the preferred frequency over a broad range of frequencies.

In addition to the preferred frequency, neurons also have the option to exploit the harmonics of this frequency. We saw that, in principle, for reliable responses the firing rate can be chosen lower than the stimulus frequency, if a 1:2 or 1:3 mode locking at harmonic frequencies is used. Alternatively, the firing rate can also be increased to yield 2:1 mode locking. In this case, responses with burst-like spikes in short sequence and bimodal inter-spike interval distributions are obtained. Spikes in short sequence can induce short-term plasticity in the synaptic transmission of central neurons, such as paired-pulse facilitation (Dobrunz and Stevens, 1997). Therefore, the differential utilization of mode-locking states may also allow to modulate synaptic plasticity.

In the third part, comprising chapter 7, an intriguing finding has been presented: the direct influence of ion channels on the sensitivity to noise, not involving changes in the average firing rate. In the suprathreshold firing mode this provides an additional mechanism to increase or decrease spike timing reliability. This effect is not bound to a particular frequency, although it is reflected more strongly at the resonance frequency and its harmonics. We could specifically show that the sensitivity to noise can be modulated by the ionic peak conductances, such as slow potassium or persistent sodium, but also by the kinetics of ionic channels, as results obtained for the time constant of slow potassium indicate. We will briefly discuss below, how this mechanism can help maintain a strong rhythmicity or to be sensitive to temporal variations in the input.

8.1   Rhythmic versus nonrhythmic signals

Rhythmic activity has been observed in many higher level brain structures, for a review see (Destexhe and Sejnowski, 2001). Oscillations measured in EEG recordings reflect synchronized

synaptic potentials in neuronal populations, but they can also be found on the level of individual cells. Often neural rhythms are associated with behavioral states, such as the theta rhythm in rat hippocampus, which is observed during explorative behavior (Vanderwolf, 1969), or the delta rhythm during slow wave sleep (Steriade, 2003). They may therefore require dynamic regulation. For a cell participating in a rhythm, the adjustment of the preferred frequency as well as the reduction of its sensitivity to noise may prove fruitful to maintain a stable oscillation.

The results in this thesis, however, give reason to suspect that neurons may choose different strategies for nonperiodic signals. An increased insensitivity to noise, as described here for cells with a large slow potassium conductance, also implies an increased insensitivity to time-varying signals in general. Especially during periods that follow a spike, the integration of the signal – and not only the noise – will be suppressed. Signal integration is thus subordinate to a maintenance of rhythmic responses in cells with reduced sensitivity to noise. For cells whose task it is to transmit potentially nonperiodic time-varying signals, such as cells in sensory peripheries or the LGN, it may be more efficient to increase the sensitivity to time-varying stimuli and compensate increased sensitivity to noise by larger stimulus amplitudes (mediated for example by an increased synaptic strength). Whether these two hypothesized strategies are valid remains to be tested in more detail.

For periodic and nonperiodic stimuli, a decrease in temporal jitter may be easier to achieve when signals are kept in the subthreshold regime, if necessary through additional inhibitory synaptic input or upregulation of the threshold. This strategy, however, comes at the cost of reduced reliability in the number of spikes, in particular the number of missing spikes may increase. The latter may be acceptable, though, if the representation of the signal is assigned to several neurons subject to uncorrelated noise sources.

8.2 Network synchrony

Spike timing reliability, as it is investigated in this thesis, reflects the ability of an individual neuron to produce phase-locked responses to its input. Therefore, spike timing reliability is also important for the synchrony in networks of neurons as described above. Given that a network is in a synchronous state, the ability of an individual neuron to maintain synchrony reduces to its ability to produce reliable, phase-locked responses to the input provided by the other neurons.

Interestingly, the results we obtained for spike timing reliability of single cells, are similar to the recent observations made in networks of conductance-based model neurons (Pfeuty et al., 2003). Pfeuty and colleagues find that potassium channels increase the network synchronicity, while persistent sodium channels enlarge asynchronous network activity. As we did for spike timing reliability, these authors establish a relation between synchrony and the influence of ionic conductances on neuronal phase-resetting curves. For synchrony, however, they particularly discuss the position of the maximum, while we focussed on the total area under the squared phase-resetting curve.

Overall, the influence of ion channels on spike timing reliability is likely to bear importance for the synchronization of neurons, but also for their ability not to synchronize.

8.3   Related problems

Questions related to the topics in this thesis arise from the results as well as from the restrictions of our analysis. Let us finish by naming a few of them:

1. A natural step to follow the analysis of spike timing reliability is to test the predictions made in section 8.2 and to analyze the influence of intrinsic parameters on the synchro- nization of networks. Although first steps in this direction have been undertaken, see for example (Pfeuty et al., 2003; Acker et al., 2003), much remains to be explored.

2. As mentioned in section 8.1, different strategies may be optimal for the spike timing of rhythmic and nonrhythmic stimuli. The spike timing reliability of nonrhythmic stimuli remains to be analyzed in detail. The outcome of such a study may allow to predict different compositions of ion channels for neurons receiving periodic inputs, such as hippocampal neurons participating in rhythms, and neurons receiving nonperiodic inputs, as for example in the sensory periphery.

3. A high value of spike timing reliability and a high rate of information transfer may not always be correlated. For example, a neuron firing periodically with perfect reliability may not convey any information about the stimulus. Therefore, it would be interesting to see, how the information rates depend on the intrinsic conductances and how these rates compare to the trends observed for spike timing reliability.

4. Additional extrinsic and intrinsic factors will also influence spike timing reliability. With regard to the results of this study, an important extrinsic influence is likely to be exerted by the synaptic background activity and the synaptic strength via the DC (Hunter and Milton, 2003). A prominent intrinsic candidate determining spike timing reliability is the noise produced by the stochastic gating of ion channels, that merits further investigation (Schneidman et al., 1998).

5. We have explored the generation of action potentials. Neural signals, however, before have to be passed from the synapse to the axon hilloc. They reach the cell in form of conductance changes (in contrast to current changes as employed in the majority of experimental and theoretical studies). On their way, the signals are extensively filtered (as for example expressed in the shape of postsynaptic potentials, PSPs) and summated in differential ways, depending on the cell geometry and the spatial distribution of ion channels. All these factors may differentially contribute to spike timing reliability and allow further insights into the role of intrinsic cell parameters.

6. Subject to further analysis rest the spike timing reliability and frequency preference in bursting neurons, which have not been discussed here. The results obtained in this study suggest the hypothesis that both, the frequency of bursts as well as the frequency within bursts, may be decisive.

7. The relation between the subthreshold resonance at threshold and the type of neuronal dynamics (I or II) has been shown for systems of two dimensions in this thesis. Whether

the presence of a resonating current activated at threshold, like a slow potassium current, can commonly be associated with type II behavior in real neurons, remains unclear.

8. Finally, a question that can be posed for any neuronal mechanism is that of additional constraints, such as energy efficiency. Because the signaling on the basis of changes in conductances involving changes in ion channel concentrations is metabolically very expensive (Attwell and Laughlin, 2001; Schreiber et al., 2002), it may be fruitful to consider this constraint when optimizing intrinsic conductances.

8.4   Finale

In this thesis we have tried to draw the attention to the fact that the properties of individual neurons, specifically the peak conductances of ion channels and their kinetics, as well as their dynamic regulation are of outstanding importance for the integration of signals in the nervous system. We have illustrated in various examples how the dynamics of single cells are shaped by intrinsic parameters and have elucidated mechanisms related to spike timing reliability and frequency preference. Though it is not shown explicitly in this work, these mechanisms and their dynamic regulation are likely to affect the gating of signals in the network and properties of the networks themselves, such as synchronization. Parameters beyond the scope of a single cell, such as the network connectivity, exert a large influence on the way signals are integrated, but the properties of individual neurons cannot be neglected.

Relating to the introduction of this thesis, the right piece of music and the cheerleading are important to motivate the audience to clap and even applaud in synchrony. But at the very basics, we need to be physically capable and willing to synchronize with the rhythm of enthusiasm after the performance. So do the neurons in our brain.

Appendix A

The measure of spike timing reliability

In this appendix we take a brief look at how the correlation-based measure compares to widely used histogram-based measures with regard to variation in the number of spikes (additional and missing spikes) and with regard to temporal jitter.[1] We also show that the basic operation underlying the measure used in this thesis – correlation of smoothed pairs of spike trains – provides a good estimate of similarity that allows to cluster spike trains according to their temporal patterns.

A.1   Comparison to histogram-based measures

Many measures have been used to characterize reliability of spike timing on the basis of the spike trains a neuron produces in response to repeated presentation of the same stimulus, see for instance (Berry et al., 1997; Hunter et al., 1998; Mainen and Sejnowski, 1995; Nowak et al., 1997; Tiesinga et al., 2002; Victor and Purpura, 1996; Van Rossum, 2001). The most widely used measures are based on the post-stimulus time histogram (PSTH), which is insensitive to the structure of individual spike trains (Tiesinga et al., 2002). In this study, we introduced a different measure of spike timing reliability that is based on the similarity between pairs of individual spike trains. This measure takes the structure of individual spike trains into account and, unlike histogram-based measures, does not depend on the *a posteriori* identification of specific events in the neural responses. As histogram-based measures, it is sensitive to the absolute timing of spikes. Precise relational timing between spikes, however, as for example precise timing of the inter-spike intervals without phase-locking to the stimulus, may not be captured.

A.1.1   Histogram-based measures

The post-stimulus time histogram (PSTH) is constructed from multiple spike trains elicited in response to the same stimulus. Fig. A.1 illustrates how the PSTH relates to the individual trials. Histogram-based spike timing measures depend on the particular choice of up to four parameters, the first of which is the bin width, $\mathrm{bin_h}$, of the histogram. To obtain an estimate of reliability, events in the PSTH have to be defined, usually as peaks in the PSTH. In order to reliably extract peaks, the PSTH is typically smoothed with a time window, τ_h, which

---

[1]This appendix is in part adapted from Schreiber et al. (2003).

constitutes the second parameter. In practice, care must be taken to set the third parameter: the threshold, θ_h, that distinguishes peaks from noise (see dashed line in the lower panels of Fig. A.1). Note that the threshold cannot be set independently of the first parameter bin_h. Once the events are detected, spikes are labeled as belonging to an event. This labeling sometimes depends on the choice of a fourth parameter, the allowable time window, w_h, around the time of peak, outside of which spikes cannot be considered as part of the event. This parameter sets a time scale that depends on the phenomena of interest.
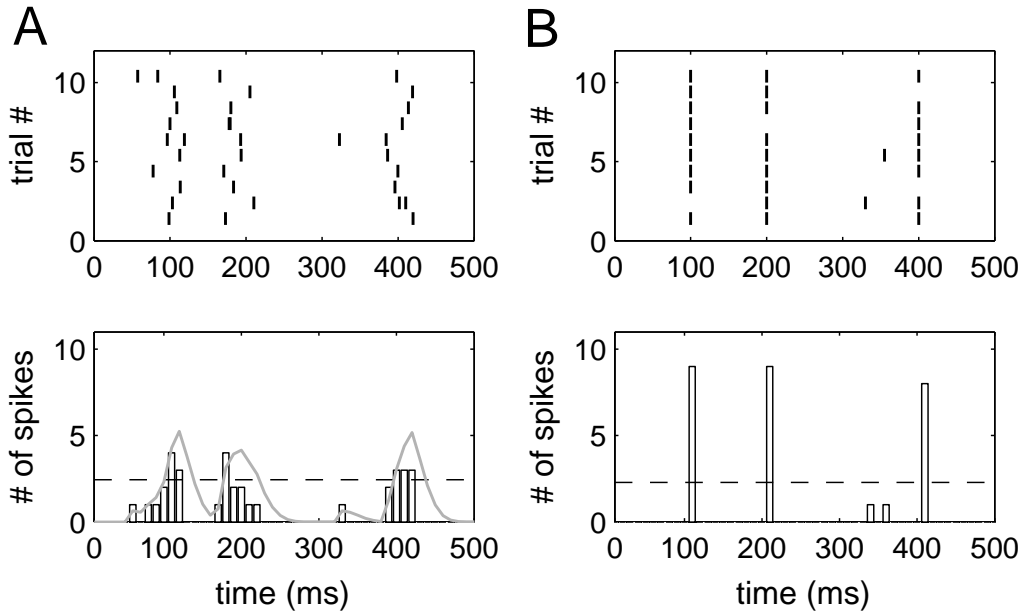
*Figure A.1: Illustration of histogram-based measures. **A** A response rastergram characterized by a significant amount of spike jitter. The PSTH (bars), a smoothed version of it (gray solid line), and a possible threshold (dashed line) are shown in the lower panel. A single spike can decide whether a group of several spikes is classified as reliable or not. **B** A rastergram with no temporal jitter, but some missing spikes. The average number of spikes in A and B is comparable. The measure is very sensitive to its parameters, especially the event threshold (dashed line).*

Reliability, R_{hist}, is defined as the average number of spikes within events, divided by the total number of spikes, n_{total}, present in the histogram: $R_{\text{hist}} = (\sum_{e \in \text{events}} n_e)/n_{\text{total}}$. Because of the dependence on four interrelated parameters a fair amount of discretion from the part of the experimenter is required. It is difficult to compare reliability measures between studies, unless exactly the same procedure has been used.

For comparison with the correlation-based measure, we smooth the PSTH with a Gaussian filter (standard deviation τ_h), the threshold, θ_h, is fixed, and only bins with values exceeding θ_h are considered event bins. The allowable window is defined as twice the width of the peak, at mid-height.

A.1.2 Surrogate test data sets

To test the two measures, a surrogate data set, consisting of seven firing events within one second is introduced (Fig. A.2). Each rastergram is comprised of $N = 35$ spike trains. Without
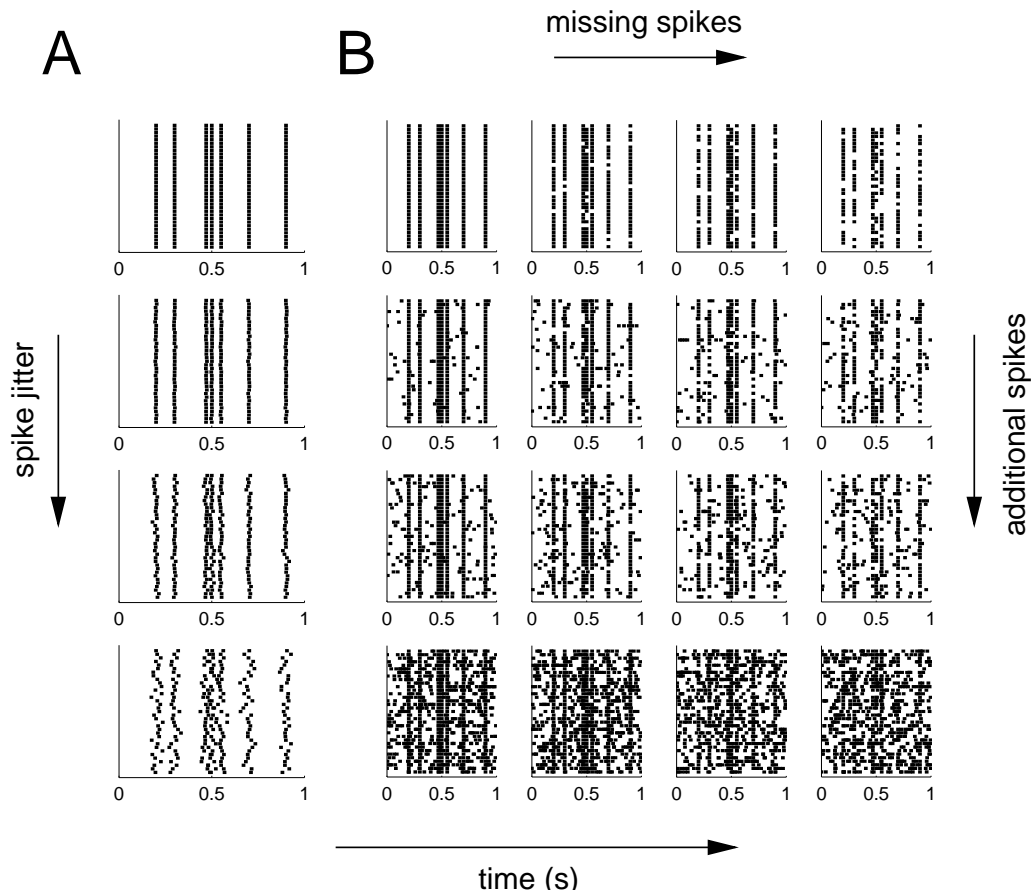
Figure A.2: **A** *The basis surrogate data set (events at 200, 300, 470, 500, 550, 700, and 900 ms) and three examples of data sets with different jitter, σ_j (2, 6, and 16 ms);* **B** *Examples of data sets of different amounts of missing and extra spikes (0, 2, 4, and 16 % extra spikes, and 0, 10, 20, 30 % missing event-spikes).*

jitter, extra spikes, and missing spikes all trials are identical and reliability equals 1 (upper rastergram in Fig. A.2A and upper left most rastergram in Fig. A.2B). This rastergram is used to derive additional surrogate sets of spike trains, by systematically varying the amount of jitter and the amount of missing and additional spikes. For the sets with variation in jitter, all spikes of each trial in the reliable set are shifted independently in time. The shift is drawn from a Gaussian distribution of the standard deviation σ_j, which characterizes the amount of jitter. For the sets with missing and additional spikes additional spikes are introduced at random times and randomly selected spikes of the reliable set are removed.

A.1.3   The performance of both measures

Reliability with jitter: Fig. A.3 shows that for the correlation measure, reliability degrades
smoothly with jitter.   For higher values of the filter width , σ_t, the reliability tends to be
higher (Fig. A.3A), because there is more overlap between smoothed spike trains.
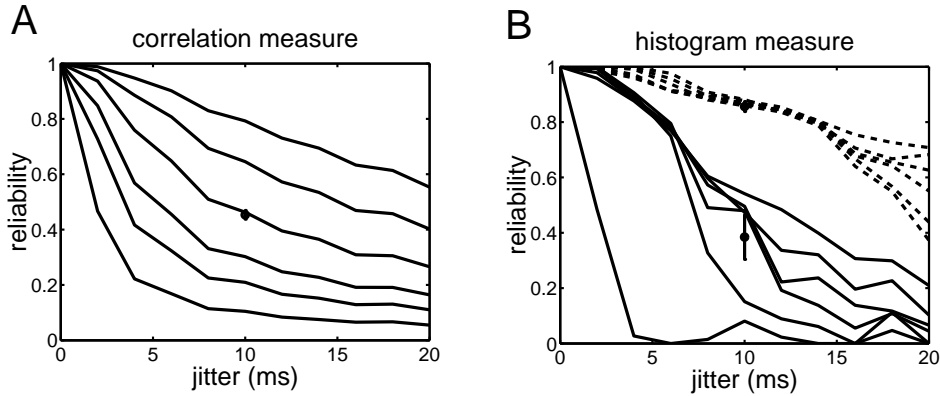
Figure A.3: **A** *Correlation-based reliability as a function of spike jitter, σ_j. Different
curves correspond to different filter width, σ_c (1, 2, 3, 5, 8, and 12 ms, bottom to top).
In a control calculation, 25 different rastergrams with 10 ms jitter were generated and
the reliability was computed for a filter width of 5 ms (circle, and standard deviation).
B Histogram-based reliability as a function of jitter (bin_h = 2 ms). Different curves
correspond to different smoothing filter widths, τ_h (1, 2, 3, 5, 8, and 12 ms, bottom to
top). The solid curves were calculated with a threshold of $\theta = 1200\,Hz$. For the dashed
curves the threshold is 600 Hz. For both measures error bars based on 25 control data sets
($\sigma_j = 10ms$, $\tau_h=5\,ms$) are indicated.*

For the histogram-based measure, the degradation of reliability with jitter is less smooth
(Fig. A.3B). The solid set of curves was obtained for a histogram measure with high threshold.
The dashed curves were obtained with the same parameters of the histogram measure, but a
threshold value lowered by 50%. Measured with a higher threshold, reliability as a function of
jitter depends on the smoothing filter width of the histogram measure, τ_h. The jaggedness of
the curves of the histogram-based measure arises because, from one jitter value to the next,
some events fall below threshold and hence change the reliability estimate discontinuously. For
a lower threshold (dashed curves), the reliability curves were highly similar and all reliability
values were high. Although this measure is stable over a broad range of filter width parame-
ters, the reliability values do not reflect the true jitter. Similar observations can be made for
reliability as a function of jitter when varying the bin size of the histogram measure (data not
shown). Altogether, the histogram-based measure proves sensitive to the choice of threshold.

Reliability with extra and missing spikes: In Fig. A.4 we compare how the reliability measures
performed on data sets that include extra and missing spikes. Fig. A.4 A shows the correlation-
based reliability as a function of the percentage of missing event-spikes. Each curve is based
on data sets with a fixed number of extra spikes per trial. Reliability values degrade smoothly

as the number of missing spikes increases. The performance of the histogram-based measure on these data, shown in Fig. A.4 B, is similar. However, the degradation is less smooth and suffers from the same threshold choice sensitivity mentioned above.
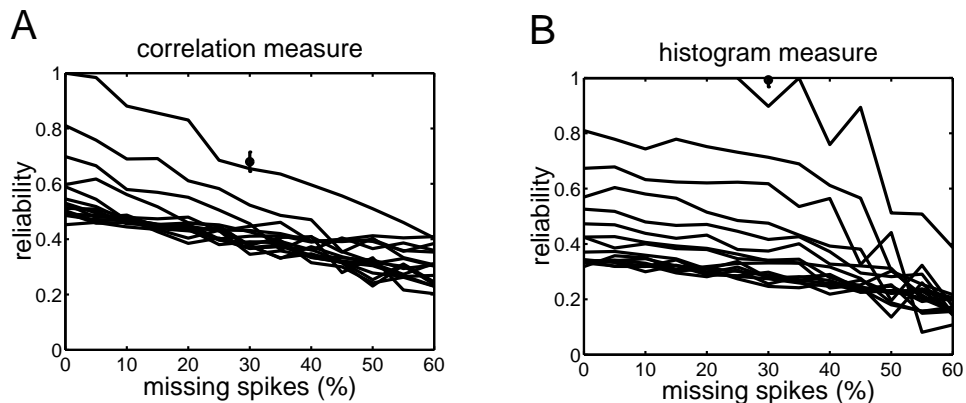
Figure A.4: **A** Correlation-based reliability as a function of missing spikes (σ_c=5 ms). Different curves correspond to different levels of extra spikes (increasing from 0 % to 30 % from top to bottom). **B** Histogram-based reliability as a function of missing spikes ($\tau_h = 5$ ms, $\text{bin}_h = 2$ ms, $\theta_h = 1500$ Hz). Different curves correspond to different levels of extra spikes (0 % to 30 % from top to bottom). The error bars in both panels are based on 25 different rastergrams (30 % missing event-spikes, no extra spikes).

Dependence on the number of trials: The estimate of spike timing reliability depends on the number of trials, N. The higher the number of trials, the smaller the (average) error in the estimate of reliability. Based on 208 surrogate data sets with extra and missing spikes (0 to 30 % extra spikes, 0 to 60 % missing spikes), we compare the errors in the reliability estimate between the histogram measure and the correlation measure as a function of the number of trials per data set, N. An error free reliability estimate would be based on an infinite number of trials; however, for practical reasons, we assume the estimate based on 35 trials to be the reference value for a given data set. The error for estimates based on fewer than 35 trials ($N < 35$) was the standard deviation of the reliability values based on N trials chosen randomly out of the full 35 trials. Fig. A.5 depicts the average error as a function of the number of trials. The error rapidly decreases with increasing N for both reliability measures. However, the error in the correlation-based reliability estimate is less than half of the error in the histogram-based estimate. Hence, fewer trials need to be recorded in an experiment in order to obtain a good reliability estimate.

A.1.4 The influence of the filter width

Both, missing and additional spikes on the one hand and temporal jitter of spikes on the other hand, decrease reliability. The only parameter of the correlation-based measure, the filter width σ_t of the Gaussian used to smooth the spike trains, determines the relative contribution of both "symptoms" of unreliability. If σ_t is on the order of one ms or below, even a small temporal jitter of only a few ms will substantially lower reliability. If σ_t is large, temporal jitter causes
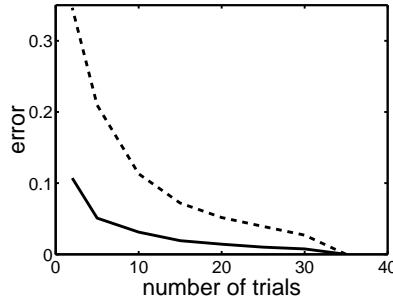
Figure A.5: The average error in reliability for the correlation-based measure (solid line, $sigma_c = 5\,ms$) and the histogram-based measure (dashed line, $\theta_h = 1500/35 \cdot N$) as a function of the number of trials, N. The error in the correlation-based estimate was always more than a factor of two lower than the error in the histogram-based estimate.

a significantly smaller decrease in the reliability estimate. Decreases in reliability then mainly reflect additional and missing spikes. Note that in the limit of $\sigma_t \to \infty$, reliability will always approach 1, as long as each response trial contains at least one spike.

Thus the analysis of the correlation-based reliability, R, as a function of σ_t can give useful information about the relevant temporal dimensions of a response. Fig. A.6 illustrates the dependences of R on the filter width σ_t for three response sets of different spike jitter.
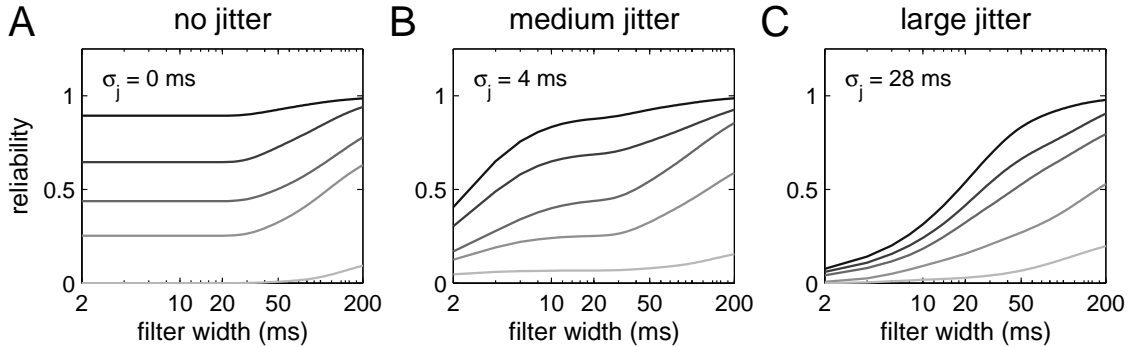
*Figure A.6: Reliability as a function of the filter width, σ_t. Reliability is quantified on the basis of surrogate rastergrams with six spiking events (at 100, 200, 400, 500, 700, and 800 ms). Different curves correspond to different temporal jitter in the events (quantified by σ_j) and a different fraction of missing spikes (10, 30, 50, 70, or 90 % from top to bottom, dark solid curves to light solid curves). **A** In the case of no temporal jitter, reliability is constant over a broad range of filter widths, until the time scale of ISIs is approached. **B** Responses with medium jitter show two inflection points; the first is indicative of the time scale of the temporal jitter. **C** For large temporal jitter only one inflection point is visible.*

For all levels of jitter and missing spikes large values of σ_t (here $\sigma_t > 50\,ms$), the filtered spike trains overlap significantly (because the distance between events is on the order of 100 ms). The reliability estimate is in this range of σ_t more indicative of the average firing rate than of the precision of individual spikes. Consequently, for practical reasons one should

chose the filter width σ_t small enough to avoid this effect.

For smaller values of σ_t, however, the reliability estimate reflects jitter and missing spikes. Interestingly, the reliability curves can show several inflection points, depending on the amount of jitter and missing spikes. In the medium jitter range, a plateau in between two inflection points is visible (Fig. A.6B). The first inflection point here characterizes the time scale where the filter width is on the order of the temporal jitter. The second inflection point relates to the time scale of the average ISI, when the filter width causes overlap between spikes in different events. In accordance with this interpretation, responses with no temporal jitter show only the second inflection point (Fig. A.6A), while the two inflection points merge to one point for responses with very large temporal jitter (Fig. A.6C). In the latter case the jitter is on the order of the ISI time scale and it is difficult to conceptually distinguish between jitter and missing spikes.

Thus the analysis of reliability as a function of the filter width provides additional information about intrinsic time scales of the responses. The shape of such curves allows to distinguish the contribution of temporal jitter from that of missing spikes. Additional plateaus may appear, if the ISI distribution of the responses is multi-modal (data not shown). Note, however, that the calculation of reliability as a function of filter width is computationally intense. In many cases, information about the temporal structure of spike trains may be obtained by simpler means, as the analysis of the raw PSTH.

A.2   Clustering

In the last section of this appendix we show that the correlation of smoothed pairs of spike trains can also be used to sort spike trains according to their temporal patterns. Stimuli can possibly give rise to two or more different spiking patterns (Tiesinga et al., 2002; Fellous et al., 2004). Reliability when assessed on the basis of all responses is likely to be low, because different temporal structures result in spikes at fixed times that are not present in all events. Within each class of patterns, however, spike timing reliability can be high.

Correlation of smoothed pairs of spike trains gives a good estimate of similarity between individual spike trains and can therefore be used to identify temporal patterns. Fig. A.7 illustrates an example. In panel A (artificially produced) spike trains are shown in random sequence, as they would be obtained in a recording. The responses seem very unreliable. The pairwise correlation of the smoothed spike trains, however, shows very low and very high values for different pairs (Fig. A.7B), indicating that some responses are very similar, while others are not.

Application of clustering algorithms to the correlation matrix of smoothed spike trains allows to sort the spike patterns apart. Fig. A.7C shows the spike trains reordered according to similarity after clustering. Efficient reordering of the sequence of spike trains allows to identify three different patterns, which before could not be identified by naked eye. The spike timing reliability within each pattern is larger than the reliability estimated across all trials. In the matrix of pairwise correlations (Fig. A.7D) the reordering is expressed in continuous areas of high similarity; similar spike trains are now grouped together.

The clustering algorithm applied is a simple K-mean algorithm, which assigns each row
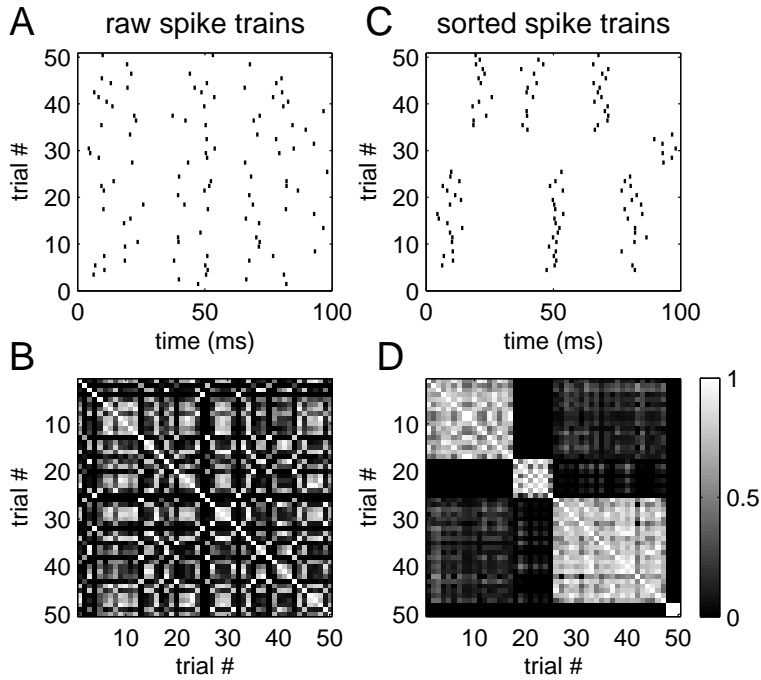
Figure A.7: Clustering of spike trains. **A** *Spike rastergram in the sequence of recording (surrogate data).* **B** *The corresponding matrix of correlations between pairs of smoothed spike trains* ($\sigma_t=4\,\text{ms}$). **C** *The reordered spike trains from (A) after application of a K-means clustering algorithm. Three different firing patterns can now easily be distinguished.* **D** *The reordered correlation matrix. Four clusters are visible (one trial with no spikes was assigned to a fourth cluster).*

vector to one of M_{clus} cluster centers.[2] M_{clus} is specified in advance (here $M_{\text{clus}}=5$). An iterative procedure alternates between updates of the membership of correlation vectors to clusters and assignment of new cluster centers (as the mean of all its current members). The objective is to minimize the squared Euclidean distance within members of the same cluster.

K-means algorithms usually converge to local optima. Therefore it is advisable to perform the clustering algorithms several times and to chose the most optimal result. The results in this thesis are based upon 50 runs of the clustering algorithm. It has proven useful to calculate two values: the average correlation of pairs belonging to the same clusters and the average correlation of pairs belonging to different clusters. The best clustering result is identified on the basis of the maximal difference between these values, which corresponds to the difference between the average values within the light and dark areas in Fig. A.7D.

Clustering of spike trains according to the principles described here is applied in Chapter 5, where different response patterns to given stimuli are identified.

---

[2]Because of the symmetry of the correlation matrix it is equivalent to cluster the column vectors.

Appendix B

Conductance-based model cells

This appendix gives the details on the conductance-based model neurons. All of these are comprised of one-compartmental, isopotential, cylindrical spheres (diameter and length measuring $89.2\,\mu m$). Spatial aspects of signal integration are neglected. As in many experimental studies, the stimulus is "injected" as current into the cells, i.e. synaptic transmission is not modeled explicitly. The mean level of depolarization can be set via the direct current component of the stimulus (I_{DC}). In order to simulate intrinsic noise, a random zero-mean current of small amplitude (usually of standard deviation σ_{n} =0.02 nA) is injected. This noise current is generated from a Gaussian distribution and is filtered with an alpha function of 3 ms time constant. In Chapter 3, specifically, σ_{n} is adjusted to yield voltage fluctuations of similar variance as those observed in the cells of layer II and III in entorhinal cortex.

The conductance-based model neurons were implemented in NEURON (Hines, 1993) and solved numerically, with a resolution of 0.1 ms (with the exception of Chapter 3, where the resolution was 0.125 ms to match the experimental procedure). The kinetics of all currents were adjusted to 36 °C. The reversal potentials were E_{Na}=55 mV, E_{K}=-90 mV, E_{L}=-80 mV, and E_{H}=-43 mV. The value of the capacitance was C_{m}=1 μF/cm^2.

B.1   Model equations

The kinetics of five currents (Na, $\mathrm{K_{dr}}$, L, $\mathrm{K_s}$, and $\mathrm{Na_P}$) are based on a model of a cortical neuron introduced by Golomb and Amitai (1997).

Sodium current, I_{Na}:

$$I_{\mathrm{Na}}(V,h) = \bar{g}_{\mathrm{Na}} m_{\infty}^3(V) h(V - E_{\mathrm{Na}}) \tag{B.1}$$

$$\frac{dh}{dt} = [h_{\infty}(V) - h]/\tau_h(V) \tag{B.2}$$

$$m_{\infty}(V) = \{1 + \exp[-(V - \theta_{\mathrm{m}})/\sigma_{\mathrm{m}}]\}^{-1} \tag{B.3}$$

$$h_{\infty}(V) = \{1 + \exp[-(V - \theta_{\mathrm{h}})/\sigma_{\mathrm{h}}]\}^{-1} \tag{B.4}$$

$$\tau_{\mathrm{h}}(V) = 0.37 + 2.78 \times \{1 + \exp[-(V - \theta_{\mathrm{ht}})/\sigma_{\mathrm{ht}}]\}^{-1} \tag{B.5}$$

where θ_{m}=-30 mV, σ_{m}=9.5 mV, θ_{h}=-53 mV, σ_{h}=-7 mV, θ_{ht}=-40.5 mV, and σ_{ht}=-6 mV.

Persistent sodium current, I_{NaP}:

$$I_{\text{NaP}}(V, h) = \bar{g}_{\text{NaP}} p_{\infty}(V)(V - E_{\text{Na}}) \tag{B.6}$$
$$p_{\infty}(V) = \{1 + \exp[-(V - \theta_{\text{p}})/\sigma_{\text{p}}]\}^{-1} \tag{B.7}$$
$$\tag{B.8}$$

with θ_{p}=-40 mV and σ_{p}=5.0 mV.

Delayed rectifier potassium current, I_{Kdr}:

$$I_{\text{Kdr}}(V, n) = \bar{g}_{\text{Kdr}} n^4 (V - E_{\text{K}}) \tag{B.9}$$
$$\frac{dn}{dt} = [n_{\infty}(V) - n]/\tau_{\text{n}}(V) \tag{B.10}$$
$$\tau_{\text{n}}(V) = 0.37 + 1.85 \times \{1 + \exp[-(V - \theta_{\text{nt}})/\sigma_{\text{nt}}]\}^{-1} \tag{B.11}$$
$$n_{\infty}(V) = \{1 + \exp[-(V - \theta_{\text{n}})/\sigma_{\text{n}}]\}^{-1} \tag{B.12}$$

where θ_{n}=-30 mV, σ_{n}=10 mV, θ_{nt}=-27 mV, and σ_{nt}=-15 mV.

Slow potassium current, I_{Ks}:

$$I_{\text{Ks}}(V, z) = \bar{g}_{\text{Ks}} z (V - E_{\text{K}}) \tag{B.13}$$
$$\frac{dz}{dt} = [z_{\infty}(V) - z]/\tau_{\text{z}} \tag{B.14}$$
$$z_{\infty}(V) = \{1 + \exp[-(V - \theta_{\text{z}})/\sigma_{\text{z}}]\}^{-1} \tag{B.15}$$

where θ_{z}=-39 mV, σ_{z}=5 mV, and τ_{z}=75 ms.

Leak current, I_{L}:

$$I_{\text{L}} = \bar{g}_{\text{L}}(V - E_{\text{L}}). \tag{B.16}$$

Slow noninactivating muscarinic potassium current, I_{M}:

$$I_{\text{M}} = \bar{g}_{\text{M}} n (V - E_{\text{K}}) \tag{B.17}$$
$$\frac{dn}{dt} = (n_{\infty} - n)/\tau_{\text{n}} \tag{B.18}$$

$$n_\infty = \{1 + \exp(-(V - \theta_n)/\sigma_n)\}^{-1} \qquad \text{(B.19)}$$

$$\tau_n = 1000\{3.3(\exp((V - \theta_{\tau_n})/\sigma_{1\tau_n}) + \exp(-(V - \theta_{\tau_n})/\sigma_{2\tau_n}))\}^{-1}/T_{adj} \qquad \text{(B.20)}$$

$$T_{adj} = 3.0^{(T-22^\circ C)/10^\circ C}, \qquad \text{(B.21)}$$

where θ_n =-35 mV, σ_n =10 mV, θ_{τ_n} =-35 mV, $\sigma_{1\tau_n} = 40$ mV, and $\sigma_{2\tau_n} = 20$ mV. For reference see (Yamada et al., 1989; Storm, 1990; Barkai et al., 1994; Gutfreund et al., 1995). Technically, values of τ_n <0.001 were set to 0.001. Exponentials with arguments larger than 50 were set to $\exp(50)$.

H current, I_H:

$$I_H = \bar{g}_H(0.8h_1 + 0.2h_2)(V - E_H) \qquad \text{(B.22)}$$

$$\frac{h_1}{dt} = (h_\infty - h_1)/\tau_1 \qquad \text{(B.23)}$$

$$\frac{h_2}{dt} = (h_\infty - h_2)/\tau_2 \qquad \text{(B.24)}$$

$$h_\infty = \{1 + \exp((V + \theta_H)/7)\}^{-1}, \qquad \text{(B.25)}$$

where θ_H= 82 mV, τ_1=40 ms, and τ_2=300 ms. The equations are based on (Spain et al., 1987), see also (Bernander et al., 1994; Hutcheon et al., 1996a).

Calcium-dependent potassium current, I_{Kca}:

$$I_{Kca} = \bar{g}_{Kca}n^2(V - E_K) \qquad \text{(B.26)}$$

$$\frac{dn}{dt} = (n_\infty - n)/\tau_n \qquad \text{(B.27)}$$

$$T_{adj} = 3^{(T-22^\circ C)/10^\circ C} \qquad \text{(B.28)}$$

$$n_\infty = \frac{[Ca]_i^2}{\theta_{Kca}^2 + [Ca]_i^2} \qquad \text{(B.29)}$$

$$\tau_n = \{\beta_n(1 + ([Ca]_i/\theta_{Kca})^2)\}^{-1}/T_{adj}, \qquad \text{(B.30)}$$

where $[Ca]_{i0}$ =2.4e-04 mM (initial intracellular calcium concentration), β_n =0.03 Hz (backward rate constant), and θ_{Kca} =5.0e-04 mM (mid activation concentration). For reference also see (Destexhe et al., 1994). If τ_n <0.1 ms, then τ_n was set to 0.1 ms. The calcium dependent potassium current, I_{Kca}, thus is a nonvoltage-dependent potassium channel, activated by intracellular calcium.

The functionality of K_{ca} requires intracellular calcium, whose dynamics include pumping of calcium ions and internal buffering, as well as a (voltage-dependent) calcium channel, Ca_L.

L-type calcium current, I_{Ca}:

$$I_{Ca} = \bar{g}_{Ca} u^2 z (V - E_{Ca}) \tag{B.31}$$

$$E_{Ca} = 12.5 \, \text{mV} \, \log([Ca]_o / [Ca]_i) \tag{B.32}$$

$$\frac{du}{dt} = (u_\infty - u)/\tau_u \tag{B.33}$$

$$\frac{dz}{dt} = (z_\infty - z)/\tau_z \tag{B.34}$$

$$V_x = -0.031(V + 37.1 \, \text{mV}) \tag{B.35}$$

$$V_u = V + 24.6 \, \text{mV} + c_u \tag{B.36}$$

$$V_z = V + 12.6 \, \text{mV} + c_z \tag{B.37}$$

$$u_\infty = \{1 + \exp(-(V_u/\sigma_u))\}^{-1} \tag{B.38}$$

$$\tau_u = 2.5 \, \text{ms} \, \{\exp(V_x/\sigma_x) + \exp(-V_x/\sigma_x)\}^{-1} \tag{B.39}$$

$$z_\infty = \{1 + \exp(V_z/\sigma_z)\}^{-1} \tag{B.40}$$

where $\bar{g}_{Ca}$ =0.1 mS/cm^2 (maximum conductance of Ca$_L$), τ_z = 5040 ms, σ_x=1 mV, σ_u=11.3 mV, σ_z =18.9 mV. If $\text{abs}(V_u)$ <1e-04 mV then c_u was set to c_u =0.00001 mV, else c_u=0 mV. If $\text{abs}(V_z)$ <1e-04 mV then c_z was set to c_z=0.00001 mV, else c_z =0 mV.

The removal of intracellular calcium dynamics was accomplished by an ATPase pump.

Calcium pump:

$$w_{ch} = -5000 I_{Ca} / F$$

$$w_{pump} = -K_{pump} \frac{[Ca]_i - ca_\infty}{[Ca]_i - ca_\infty + K_{eq}}$$

$$\frac{d[Ca]_i}{dt} = w_{ch} + w_{pump} + (ca_\infty - [Ca]_i)/\tau_r$$

where w_{pump} is the calcium drive through the pump, w_{ch} the calcium drive through the calcium channel Ca$_L$, ca_∞ =2.4e-04 mM (equilibrium intracellular calcium concentration), and τ_r =1e10 ms (time constant of calcium removal by buffering). The time constant τ_r was designed to model a first order removal of intracellular calcium, which we neglected by setting τ_r to a very large value. K_{pump} =4e-04 mM/ms (time constant of the ATPase), K_{eq} =0.02 mM (equilibrium value for the ATPase), and F =96485.309 Cmol^{-1} (Faraday constant). If w_{ch} was smaller than 0 then w_{ch} was set to 0 (no inward pumping). For reference see (Destexhe et al., 1993).

B.2 Parameter sets

The following three tables summarize the parameters of the peak conductances. The parameters used in the Chapters 2 to 5 are (in mS/cm^2):

	$\bar{g}_{\text{Na}}$	$\bar{g}_{\text{Kdr}}$	$\bar{g}_{\text{L}}$	$\bar{g}_{\text{NaP}}$	$\bar{g}_{\text{Ks}}$	$\bar{g}_{\text{M}}$	$\bar{g}_{\text{H}}$
Fig. 2.3A	24	3	0.06	—	—	—	0.2
Fig. 2.3B	24	3	0.02	0.06	—	0.4	—
Fig. 2.3C, 4.8	24	3	0.02	0.03	—	0.4	0.2
Fig. 3.2G + all Chapter 3 (stellate)	24	3	0.04	0.02	—	0.4	0.25
Fig. 3.2H + all Chapter 3 (pyramidal)	24	3	0.07	0.02	—	—	—
Fig. 4.1, 4.2, 4.3, 4.4A, 4.5A, and 4.9A	24	3	0.02	0.2	—	1	0.04
Fig. 4.4B, 4.5B, 4.7, 4.9B	24	3	0.02	0.2	—	1	—
Fig. 4.6, 4.9C	24	3	0.04	0.02	0.1	—	—
Fig. 5.1, 5.3, 5.4	24	3	0.02	0.07	1	—	—

The analysis in Chapter 5 is based on the parameter set of the reference cell, as given in the table above for Fig. 5.1. For the figures, where individual conductance values deviate from the reference cell, the parameters are summarized in the following table (in mS/cm^2). The second column states the parameter values used for the firing rate analysis:

	variation of individual conductances (Fig. 5.5, Fig. 5.6A, Fig. 5.6B, and Fig. 5.9)	firing rate analysis (Fig. 5.7A)
$\bar{g}_{\text{Na}}$	10, 15, 30, 50, 70, 100	$(1, 2, 3, \ldots, 10) \cdot 10$
$\bar{g}_{\text{NaP}}$	0, 0.07, 0.2, 0.3, 0.4	$(0, 1, 2, \ldots, 10) \cdot 0.04$
$\bar{g}_{\text{L}}$	0, 0.005, 0.01, 0.015, 0.02, 0.025, 0.03, 0.035, 0.04	$(0, 1, 2, 3, 4) \cdot 0.01$
$\bar{g}_{\text{Ks}}$	0.05, 0.1, 0.15, 0.2, 0.3, 0.4, 0.6, 1.0, 1.5, 2.0	$(0, 1, 2, \ldots, 10) \cdot 0.2$
$\bar{g}_{\text{Kdr}}$	1.5, 2, 3, 6, 10, 15, 20, 25, 30	$(1, 2, 3, \ldots, 10) \cdot 3$
$\bar{g}_{\text{M}}$	0.05, 0.1, 0.15, 0.2, 0.25, 0.3, 0.35, 0.4	not used
$\bar{g}_{\text{Kca}}$	0.02, 0.03, 0.04, 0.05, 0.07, 0.1, 0.2, 0.4, 0.5	not used

The conductance values were chosen such that conductance changes from the reference cell (parameters as for Fig. 5.1) resulted in regular spiking electrical responses to $I_{\text{DC}} = 0.3\,\text{nA}$, where the peak voltage of spikes was smaller than 50 mV, and no bursting was observed. No conductance was increased by more than a factor of 10 from the reference cell. The conductance parameters of the four examples shown in Fig. 5.7B are (in mS/cm^2):

	$\bar{g}_{\text{Na}}$	$\bar{g}_{\text{NaP}}$	$\bar{g}_{\text{L}}$	$\bar{g}_{\text{Ks}}$	$\bar{g}_{\text{Kdr}}$
Na varied	varied	0	0.01	0.4	3
Na$_{\text{P}}$ varied	30	varied	0.03	0.4	6
L varied	20	0.04	varied	0.2	6
K$_{\text{dr}}$ varied	40	0.08	0.03	0.2	varied

All model cells in Chapter 7 have the parameters of the reference cell, apart from the individual parameters that are varied. These are indicated in the figures of that chapter.

B.3   Firing rate analysis

For the firing rate analysis, as presented in (Fig. 5.7), the parameter space of Na, Na_P, K_{dr}, K_s, and L conductances was analyzed. DC firing rates were obtained for all possible parameter combinations within this parameter space. The maximum change in firing rate achievable by one ion channel type was characterized (for each combination of the other four conductances) as the difference between the maximum and minimum (non-zero) firing rates achievable by variation of the ion channel conductance of interest, keeping the other four conductances fixed. If a cell never fired despite variation in one conductance, it was excluded from the parameter space (less than 5 % of the total four-dimensional conductance space for any channel type tested). The distribution of maximum changes in firing rate achievable by variation of the density of one ion channel type over all combinations of the other four densities is presented in Fig. 5.7A.

   Though limited to the descriptive level, the following principles can be extracted: K_{dr} can modify preferred frequency over several tens of Hz if K_s is not present or present only in small amounts. Na_P can cause a large frequency shift if both potassium conductances, K_{dr} and K_s, are low. Na is potent in changing the frequency if both potassium conductances and Na_P are low. Its influence in these cases weakens further with a higher density of leak channels. Leak channel variation also gives rise to higher frequency shifts if both potassium conductances are low and the sodium conductances are not too large. In general, higher densities of leak channels tend to lower the minimum achievable frequency.

Appendix C

Morris-Lecar model neurons

This appendix defines the full Morris-Lecar model and describes its linearization. In addition, characteristics of the electrical impedance, such as the resonance frequency and the Q-value, are derived analytically for the general linearized system of two coupled differential equations. Finally, a relation between the bifurcation type and the existence of a subthreshold resonance at threshold is established for models of two dimensions.

C.1   The model

In order to describe the voltage dynamics of the muscle fibers of barnacles, Morris and Lecar developed a set of three coupled differential equations (neglecting spatial dependencies) based on two ionic currents: an outward noninactivating potassium current and an inward noninactivating calcium current. Following Rinzel and Ermentrout (1998), we assume that the calcium current is always in equilibrium for the time scales considered. The assumption is justified, because the Ca^{2+} current responds much faster than the K^+ current. Thus the dynamics of the Ca^{2+} current can be neglected and the number of equations is reduced to two. The equations are

$$C_{\mathrm{m}}\frac{dV}{dt} = -\bar{g}_{\mathrm{Ca}}m_\infty(V)(V - E_{\mathrm{Ca}}) - \bar{g}_{\mathrm{K}}\mathrm{w}(V - \mathrm{E_K}) - \bar{g}_{\mathrm{L}}(V - \mathrm{E_L}) + \mathrm{I}_{\mathrm{ext}} \qquad (C.1)$$

$$\frac{d\mathrm{w}}{dt} = \Phi\frac{\mathrm{w}_\infty(\mathrm{V}) - \mathrm{w}}{\tau_{\mathrm{w}}(V)}, \qquad (C.2)$$

where w is the activation variable for potassium, $\bar{g}_{\mathrm{Ca}}$ is the Ca^{2+} peak conductance, and E_{Ca} is the calcium reversal potential. The calcium and potassium voltage-dependent activation curves are

$$m_\infty(V) = 0.5\left[1 + \tanh\{(\mathrm{V} - \mathrm{V_1})/\mathrm{V_2}\}\right], \qquad (C.3)$$

$$\mathrm{w}_\infty(\mathrm{V}) = 0.5\left[1 + \tanh\{(\mathrm{V} - \mathrm{V_3})/\mathrm{V_4}\}\right], \qquad (C.4)$$

and the potassium time constant is

$$\tau_{\mathrm{w}}(V) = 1/\cosh\{(\mathrm{V} - \mathrm{V_3})/2\mathrm{V_4}\}. \qquad (C.5)$$

The parameters are C_m=1μF/cm^2, V_1=-1 mV, V_2=15 mV, $\bar{g}_\mathrm{Ca}$=1.1 mS/cm^2, $\bar{g}_\mathrm{K}$=2.0 mS/cm^2, g_L=0.5 mS/cm^2, E_Ca=100 mV, E_K=-70 mV, and E_L=-50 mV.

An advantage of the Morris-Lecar model is that it can exhibit type I as well as type II neuronal dynamics (depending on only few parameters). The other parameter values used for the model neurons in Chapters 4 and 6 are V_3=10 mV, V_4=14 mV, Φ =1/3 (type I), and V_3=0 mV, V_4=30 mV, Φ =1/5 (type II). Chapter 6 also uses additional values for these parameters, which are given by a linear interpolation between the type I and type II parameters stated here.

Although the Morris-Lecar system has only two dimensions, it is still highly nonlinear and in general, exact analytical solutions are not possible. The data for spike timing reliability are therefore obtained numerically. If the voltage responses are constrained to the subthreshold regime, however, linearization of the system proves useful for small-amplitude stimuli and responses can be approximated analytically.

C.2 Linearization of the Morris-Lecar model

If the full Morris-Lecar system (Eq. C.1 and Eq. C.2) is represented in the following form,

$$\frac{d}{dt}\begin{pmatrix} V \\ \mathrm{w} \end{pmatrix} = \begin{pmatrix} f(V,\mathrm{w}) \\ g(V,\mathrm{w}) \end{pmatrix} + \begin{pmatrix} I_\mathrm{ext} \\ 0 \end{pmatrix}, \tag{C.6}$$

the linearized system (with new variables $x_1 = V - V_\mathrm{st}$ and $x_2 = \mathrm{w} - \mathrm{w}_\mathrm{st}$) is given by

$$\frac{d}{dt}\begin{pmatrix} x_1 \\ x_2 \end{pmatrix} = \begin{pmatrix} \frac{\partial f}{\partial V} & \frac{\partial f}{\partial \mathrm{w}} \\ \frac{\partial g}{\partial V} & \frac{\partial g}{\partial \mathrm{w}} \end{pmatrix}_{V_\mathrm{st}} \begin{pmatrix} x_1 \\ x_2 \end{pmatrix}. \tag{C.7}$$

The steady state values of the original variables, V_st and w_st, at a given value of $I_\mathrm{ext} = \mathrm{const}$ have to be obtained numerically by solution of the equations $dV/dt = 0$ and $d\mathrm{w}/dt = 0$. The coefficients of the linearized Morris-Lecar system read

$$\left.\frac{\partial f}{\partial V}\right|_{V_\mathrm{st}} = \frac{1}{C_\mathrm{m}}\left\{-\bar{g}_\mathrm{Ca}\left[(V_\mathrm{st} - E_\mathrm{Ca})\left.\frac{\partial m_\infty}{\partial V}\right|_{V_\mathrm{st}} + m_\infty(V_\mathrm{st})\right] - \bar{g}_\mathrm{K}\mathrm{w}_\infty(V_\mathrm{st}) - g_\mathrm{L}\right\} \tag{C.8}$$

$$\left.\frac{\partial f}{\partial \mathrm{w}}\right|_{V_\mathrm{st}} = -\frac{\bar{g}_\mathrm{K}}{C_\mathrm{m}}(V_\mathrm{st} - E_\mathrm{K}) \tag{C.9}$$

$$\left.\frac{\partial g}{\partial V}\right|_{V_\mathrm{st}} = \frac{1}{\tau_\mathrm{w}(V_\mathrm{st})}\left.\frac{\partial \mathrm{w}_\infty}{\partial V}\right|_{V_\mathrm{st}} \tag{C.10}$$

$$\left.\frac{\partial g}{\partial \mathrm{w}}\right|_{V_\mathrm{st}} = -\frac{1}{\tau_\mathrm{w}(V_\mathrm{st})}, \tag{C.11}$$

with

$$\left.\frac{\partial m_\infty}{\partial V}\right|_{V_\mathrm{st}} = \frac{1}{2V_2 \cosh^2\left(\frac{V_\mathrm{st} - V_1}{V_2}\right)} \tag{C.12}$$

$$\left.\frac{\partial \mathrm{w}_\infty}{\partial V}\right|_{V_\mathrm{st}} = \frac{1}{2V_4 \cosh^2\left(\frac{V_\mathrm{st} - V_3}{V_4}\right)}. \tag{C.13}$$

C.3 Resonance frequency and impedance

The subthreshold resonance frequency for linearized two-dimensional model neuron systems, including the linearized Morris-Lecar model, can be derived analytically. We consider linearized systems of the form

$$\frac{d}{dt}\begin{pmatrix} x_1 \\ x_2 \end{pmatrix} = \begin{pmatrix} a & b \\ c & d \end{pmatrix}\begin{pmatrix} x_1 \\ x_2 \end{pmatrix} + \begin{pmatrix} I_1(t) \\ I_2(t) \end{pmatrix}. \tag{C.14}$$

The eigenvalues, λ_1 and λ_2, are

$$\lambda_{1/2} = \frac{a+d}{2} \pm \sqrt{\frac{(a+d)^2}{4} - (ad - bc)}. \tag{C.15}$$

The solution of the system based upon variation of constants allows to describe the response to sine wave stimuli of fixed amplitude ($I_1(t) = \sin(\omega t)$, while $I_2(t) = 0$). The corresponding voltage response is again a sine wave, whose amplitude is proportional to the electrical impedance at the frequency $f = \omega/2\pi$. Except for a constant factor, the impedance is therefore determined by

$$Z(\omega) = \sqrt{\frac{d^2 + \omega^2}{b^2c^2 + 2bc(\omega^2 - ad) + (a^2 + \omega^2)(d^2 + \omega^2)}}. \tag{C.16}$$

The resonance frequency, f_{res}, is determined by the values of ω where the condition $dZ(\omega)/d\omega = 0$ is fulfilled. Consequently, the resonance frequency reads

$$f_{\mathrm{res}} = \frac{1}{2\pi}\sqrt{-d^2 + \sqrt{b^2c^2 - 2abcd - 2bcd^2}}. \tag{C.17}$$

The Q-value, is defined as the ratio of impedance at the resonance frequency and the impedance at 0 Hz, i.e. $Q = Z(2\pi f_{\mathrm{res}})/Z(0)$ with $Z(0) = |d|/|ad - bc|$.

For the Morris-Lecar model the linear coefficients are given by

$$\begin{pmatrix} a & b \\ c & d \end{pmatrix} = \begin{pmatrix} \frac{\partial f}{\partial V} & \frac{\partial f}{\partial \mathrm{w}} \\ \frac{\partial g}{\partial V} & \frac{\partial g}{\partial \mathrm{w}} \end{pmatrix}_{V_{st}}, \tag{C.18}$$

as presented in the previous section.

C.4 Bifurcation type and subthreshold resonance

In order for oscillations to emerge in a bifurcation, as it is the case for spiking neurons, the bifurcation type in two-dimensional systems has to be either a Hopf bifurcation (type I) or a

saddle-node bifurcation (type II) (Izhikevich, 2000). The bifurcation type in these systems is tied to the existence (or nonexistence) of a subthreshold resonance at the threshold (i.e. at the bifurcation point), as we will show in the following. If the fixed point loses stability in a Hopf bifurcation, the system shows a subthreshold resonance at threshold and *vice versa*. If on the other hand, the fixed point loses stability in a saddle-node bifurcation, it follows that no subthreshold resonance exists at threshold and *vice versa*.

Given that the decision whether the bifurcation type of the nonlinear system (with emerging oscillations) is a Hopf or a saddle-node can be made on the basis of the linearized system, as can the decision whether a resonance exists at threshold or not, we briefly prove these statements on the basis of the linearized systems.

In order to have a subthreshold resonance, the resonance frequency, f_{res}, (as stated in Eq. C.17) has to be real and positive.

Hopf bifurcation:

At a Hopf bifurcation two conditions hold:

$$a \;=\; -d \qquad \text{and} \qquad\qquad \text{(C.19)}$$
$$\Delta = -d^2 - bc = -d^2 + |bc| \;>\; 0, \qquad\qquad \text{(C.20)}$$

where Δ denotes the determinant of the matrix of eigenvalues,

$$\begin{pmatrix} \lambda_1 & 0 \\ 0 & \lambda_2 \end{pmatrix}. \qquad\qquad \text{(C.21)}$$

The first condition (Eq. C.19) results from the fact that at the point of Hopf bifurcation the trace of the matrix of eigenvalues is 0 (or in other words, the real value of the eigenvalues is 0). The second (Eq. C.20) is the consequence of the first condition and a positive determinant, $\Delta > 0$ at the Hopf bifurcation. The latter also guarantees that $|bc| = -bc$.

From these conditions and Eq. C.17 it follows that $w_{\mathrm{res}} = \sqrt{-d^2 + |bc|} = \sqrt{\Delta}$ and therefore w_{res} real and $w_{\mathrm{res}} > 0$. If the bifurcation at the neuronal threshold is of type Hopf, a subthreshold resonance exists.

Saddle-node bifurcation:

A saddle-node bifurcation fulfills the following conditions:

$$a + d < 0 \qquad \text{and} \qquad\qquad \text{(C.22)}$$
$$\Delta = ad - bc = 0. \qquad\qquad \text{(C.23)}$$

If the bifurcation at threshold is a saddle node, the neuron does not exhibit a resonance at threshold. The prove is led indirectly. Let us assume that a neuron with a saddle-node bifurcation had a resonance (i.e. a real, positive w_{res}), then the expression under the outer

square root in Eq. C.17, as well as the expression under the inner square root would have to be positive and real. Taking Eq. C.23 into account,

$$\sqrt{(-a^2 - 2ad)d^2} > d^2 \tag{C.24}$$

would follow from the outer square root. Because both sides of the inequality are positive ($d^2 > 0$ and the inner square root of Eq. C.17 is real and positive), squaring would give

$$-a^2 - 2ad - d^2 = -(a + d)^2 > 0, \tag{C.25}$$

which is a contradiction for all values of $a, d \in$R. Thus a saddle-node bifurcation cannot exhibit a subthreshold resonance at the bifurcation point.

Because a neuron can only cross threshold in a saddle-node or a Hopf bifurcation, the derived relations are equivalent. I.e. the existence of a resonance at threshold also determines the bifurcation type.

Appendix D

Experimental Methods

The electrophysiological methods used for the recordings in layer II and II neurons of the entorhinal cortex (Chapter 3) and for the dynamic patch-clamp recordings in cells of prefrontal cortex (Chapter 5) are described here. The experiments in the entorhinal cortex were done by Irina Erchova (at Humboldt-University Berlin/Charité), the experiments in the prefrontal cortex were done by Jean-Marc Fellous (The Salk Institute, La Jolla, USA).[1]

D.1   Recordings in entorhinal cortex

Slice preparation: Horizontal hippocampal slices (400μm) were prepared from adult Wistar rats (2.5-4 months, 350-400g) of both sexes after decapitation under deep ether induced anesthesia in accordance with animal care regulations. Slices were maintained at room temperature in a submerged-style holding chamber until transferred one by one to the recording chamber (36.7 °C). Slices were superfused with artificial cerebrospinal fluid (ACSF) containing (mM): 129 NaCl, 3 KCl, 1.25 NaH_2PO_4, 1.8 $MgSO_4$, 1.6 $CaCl_2$, 21 $NaHCO_3$ and 10 glucose, pH 7.4; bubbled with carbogen gas 95 % O_2 − 5 % CO_2.

Recording conditions: Intracellular recordings in medial entorhinal cortex were done using sharp glass micropipets (electrode puller P-87, Shutter Instruments, USA), filled with 2M potassium acetate, 2 % biocytin, 75-85 $M\Omega$, in current clamp mode. Data were amplified (NeroData IR 183, NY, USA), low-pass filtered at 3 KHz and digitized with an IO-card (DAQ card AI16E4 National Instruments Inc, TX, USA) at a sampling rate of 8 KHz. For stimulus generation and data acquisition LabView (National Instruments Inc, TX, USA) was used. All recordings were done at 36.7 °C, synaptic transmission was blocked by (μM): 30 CNQX, 60 APV, 5 bicucculine, and 1 CGP55845A (3-N-[1-(s)-(3,4-dichlorophenyl)ethyl]amino-2-(s)-hydroxypropyl-P-benzyl-phosphinic acid, a GABA B blocker, kind gift from Novartis, Basel, Switzerland). All other chemicals were obtained from Sigma-Aldrich, Deisenhofen, Germany.

Histology: For staining slices were stored in 4 % paraformaldehyde, shortly left in sucrose 30 % and cut at 50μm. Biocytin was revealed by standard procedure (Horikawa and Armstrong, 1988) using fluorescent marker Alexa 466 coupled to avidin (Molecular probes, Leijden, The Netherlands).

---

[1]The appendix is adapted from Schreiber *et al.* (2004a) and Schreiber *et al.* (2004b).

D.2   Recordings in prefrontal cortex

Coronal slices of rat prelimbic and infralimbic areas of prefrontal cortex were obtained from 2 - 4 weeks old Sprague-Dawley rats. Rats were anesthetized with Isoflurane (Abbott Laboratories, IL) and decapitated. Their brain were removed and cut into 350 μm thick slices using standard techniques. Patch-clamp was performed under visual control at 30-32 °C. In most experiments Lucifer Yellow (RBI, 0.4 %) or Biocytin (Sigma, 0.5 %) was added to the internal solution. In all experiments, synaptic transmission was blocked by D-2-amino-5-phosphonovaleric acid (D-APV; 50 μM), 6,7-dinitroquinoxaline-2,3, dione (DNQX; 10 μM), and Biccuculine methiodide (Bicc; 20 μM). All drugs were obtained from RBI or Sigma, freshly prepared in ACSF and bath applied. Whole cell patchclamp recordings were achieved using glass electrodes (4-10 MΩ) containing (in mM): KMeSO$_4$, 140; Hepes, 10; NaCl, 4; EGTA, 0.1; MgATP, 4; MgGTP, 0.3; phosphocreatine 14. Data were acquired in current clamp mode using an Axoclamp 2A amplifier (Axon Instruments, Foster city, CA).

Data were acquired using two computers. The first computer was used for standard data acquisition and current injection. Programs were written using Labview 6.1 (National Instrument, Austin, TX), and data were acquired with a PCI16E1 data acquisition board (National Instrument, Austin, TX). Data acquisition rate was either 10 or 20 kHz. The second computer was dedicated to dynamic clamp. Programs were written using either a Labview RT 5.1 (National Instrument, Austin, TX) or a Dapview (Microstar Laboratory, Bellevue, WA) front-end and a C language backend. Dynamic clamp (Hughes *et al.* 1998; Jaeger and Bower 1999; Sharp *et al.* 1993) was implemented using a DAP5216a board (Microstar Laboratory, Bellevue, WA) at a rate of 10 kHz. A dynamic clamp was achieved by implementing a rapid (0.1 ms) acquisition/injection loop in current clamp mode. All experiments were carried in accordance with animal protocols approved by the N.I.H.

Stimuli consisted of sine waves of 30 different frequencies (1 to 30 Hz) presented for 2 seconds. Only one amplitude was tested. No additional noise was injected. The first 500 ms were discarded for analysis of reliability.

References

Abeles, M. (1991). *Corticonics.* Cambridge University Press, Cambridge.

Acker, C. D., Kopell, N., and White, J. A. (2003). Synchronization of strongly coupled excitatory neurons: Relating network behavior to biophysics. *J Comp Neurosci*, 15:71–90.

Adrian, E. D. A. (1928). *The basis of sensation, the action of the sense organs.* Norton, New York.

Alonso, A. and Klink, R. (1993). Differential electroresponsiveness of stellate and pyramidal-like cells of medial entorhinal cortex layer II. *J Neurophysiol*, 70:128–143.

Alonso, A. and Llinás, R. R. (1989). Subthreshold Na^+-dependent theta-like rhythmicity in stellate cells of entorhinal cortex layer II. *Nature*, 342:175–177.

Attwell, D. and Laughlin, S. B. (2001). An energy budget for signalling in the grey matter of the brain. *J Cereb Blood Flow Metab*, 21:1133–1145.

Axmacher, N. and Miles, R. (2004). Intrinsic cellular currents and the temporal precision of EPSP - action potential coupling in CA1 pyramidal cells. *J Physiol*, 555:713–725.

Bair, W. (1999). Spike timing in the mammalian visual system. *Curr. Opin. Neurobiol.*, 9:447–453.

Bair, W. and Koch, C. (1996). Temporal precision of spike trains in extrastriate cortex of the behaving macaque monkey. *Neural Comput.*, 8:1185–1202.

Barkai, E., Bergman, R. E., Horwitz, G., and Hasselmo, M. E. (1994). Modulation of associative memory function in a biophysical simulation of rat piriform cortex. *J Neurophysiol*, 72(2):659–77.

Beierholm, U., Nielsen, C. D., Ryge, J., Alstrom, P., and O, K. (2001). Characterization of reliability of spike timing in spinal interneurons during oscillating inputs. *J Neurophysiol*, 86(4):1858–68.

Benda, J. and Herz, A. V. M. (2003). A universal model for spike-frequency adaptation. *Neural Comput*, 15:2523–2564.

Berger, H. (1929). Über den zeitlichen Verlauf der negativen Schwankung des Nervenstroms. *Arch Ges Physiol*, 1:173.

Bernander, O., Koch, C., and Douglas, R. (1994). Amplification and linearization of distal synaptic input to cortical pyramidal cells. *J Neurophysiol*, 72:2743–2753.

Berry, M. J., Warland, D. K., and Meister, M. (1997). The structure and precision of retinal spike trains. *Proc Natl Acad Sci USA*, 94(10):5411–5416.

Bi, G. Q. and Poo, M. M. (1998). Synaptic modifications in cultured hippocampal neurons: dependence on spike timing, synaptic strength, and postsynaptic cell type. *J Neurosci*, 18:10464–10472.

Bland, B. H. and Colom, L. V. (1993). Extrinsic and intrinsic properties underlying oscillation and synchrony in limbic cortex. *Prog Neurobiol*, 41:157–208.

Brette, R. and Guigon, E. (2003). Reliability of spike timing is a general property of spiking model neurons. *Neural Comput*, 15:279–308.

Britten, K. H., Shadlen, M. N., Newsome, W. T., and Movshon, J. A. (1992). The analysis of visual motion: a comparison of neuronal and psychophysical performance. *J. Neurosci.*, 12:4745–65.

Buzsaki, G. (2002). Theta oscillations in the hippocampus. *Neuron*, 33:325–340.

Buzsaki, G., Leung, L. W., and Vanderwolf, C. H. (1983). Cellular bases of hippocampal EEG in the behaving rat. *Brain Res*, 287:139–171.

Cecchi, G. A., Sigman, M., Alonso, J. M., Martinez, L., Chialvo, D. R., and Magnasco, M. O. (2000). Noise in neurons is message dependent. *Proc Natl Acad Sci U S A*, 97:5557–5561.

Chi, Z. and Margoliash, D. (2001). Temporal precision and temporal drift in brain and behavior of zebra finch song. *Neuron*, 32:899–910.

Chrobak, J. and Buzsaki, G. (1998). Gamma oscillations in the entorhinal cortex of the freely behaving rat. *J Neurosci*, 18:388–398.

Cole, K. (1968). *Membranes, iones and impulses.* University of California Press, Berkeley and Los Angeles.

Connors, B. and Gutnick, M. (1990). Intrinsic firing patterns of diverse neocortical neurons. *Trends Neurosci*, 13(9):365–6.

Coombes, S. and Bressloff, P. C. (1999). Mode locking and Arnold tongues in integrate-and-fire neural oscillators. *Phys Rev E*, 60:2086–2096.

Dayan, P. and Abbott, L. F. (2001). *Theoretical Neuroscience: Computational and mathematical modeling of neural systems.* MIT Press, Cambridge.

de Ruyter van Steveninck, R. R., Lewen, G. D., Strong, S. P., Koberle, R., and Bialek, W. (1997). Reproducibility and variability in neural spike trains. *Science*, 275:1805–1808.

deCharmes, R. C. and Zador, A. (2000). Neural representation and the cortical code. *Annu Rev Neurosci*, 23:613–647.

DeFelice, L. J. (1981). *Introduction to channel noise.* Plenum Press.

Destexhe, A., Babloyantz, A., and Sejnowski, T. J. (1993). Ionic mechanisms for intrinsic slow oscillations in thalamic relay neurons. *Biophys J*, 65:1538–52.

Destexhe, A., Contreras, D., and Sejnowski, T. J. (1994). A model of spindle rhythmicity in the isolated thalamic reticular nucleus. *J Neurophys*, 72:803–18.

Destexhe, A. and Sejnowski, T. J. (2001). *Thalamocortical assemblies.* Oxford University Press.

Destexhe, A. and Sejnowski, T. J. (2003). Interactions between membrane conductances underlying thalamocortical slow-wave oscillations. *Physiol Rev*, 83:1401–1453.

Dickson, C., Magistretti, J., Shalinsky, M., Fransen, E., Hasselmo, M., and Alonso, A. (2000a). Properties and role of I(h) in the pacing of subthreshold oscillations in entorhinal cortex layer II neurons. *J Neurophysiol*, 83(5):2562–79.

Dickson, C. T., Magistretti, J., Shalinsky, M. H., Hamam, B., and Alonso, A. (2000b). Oscillatory activity in entorhinal neurons and circuits. Mechanisms and function. *Ann N Y Acad Sci*, 911:127–50.

Dobrunz, L. E. and Stevens, C. F. (1997). Heterogeneity of release probability, facilitation, and depletion at central synapses. *Neuron*, 18:995–1008.

Dorval, A. D., Christini, D. J., and White, J. A. (2001). Real-time linux dynamic clamp: A fast and flexible way to construct virtual ion channels in living cells. *Annals of biomed. engineering*, 29 (10):897–907.

Erchova, I., Kreck, G., Heinemann, U., and Herz, A. V. M. (2004). Dynamics of rat entorhinal cortex layer II-III cells: characteristics of membrane potential resonance at rest predict oscillation properties near threshold. *J Physiol, Submitted.*

Ermentrout, B. (1996). Type I membranes, phase resetting curves, and synchrony. *Neural Comput*, 8:979–1001.

Falk, G. and Fatt, P. (1964). Linear electrical properties of striated muscle fibres observed with intracellular electrode. *Proc R Soc*, B160:69–123.

Fellous, J. M., Houweling, A. R., Modi, R. H., Rao, R. P., Tiesinga, P. H., and Sejnowski, T. J. (2001). Frequency dependence of spike timing reliability in cortical pyramidal cells and interneurons. *J Neurophysiol.*, 85(4):1782–7.

Fellous, J. M., Tiesinga, P. H. E., Thomas, P. J., and Sejnowski, T. J. (2004). Discovering spike patterns in neuronal responses. *J Neurosci, in Press.*

Fishman, H. M., Poussart, D. J. M., Moore, L. E., and Siebenga, E. (1977). K^+ conduction description from low-frequency impedance and admittance of squid axon. *J Memb Biol*, 32:255–290.

Franz, A. and Ronacher, B. (2002). Temperature dependence of temporal resolution in an insect nervous system. *J Comp Physiol A*, 188:261–271.

Fricker, D. and Miles, R. (2000). EPSP amplification and the precision of spike timing in hippocampal neurons. *Neuron*, 28:559–69.

Fricker, D. and Miles, R. (2001). Interneurons, spike timing, and perception. *Neuron*, 32:771–774.

Gimbarzevsky, B., Miura, R., and Puil, E. (1984). Impedance profiles of peripheral and central neurons. *Can J Physiol Pharmacol*, 62:460–462.

Gloveli, T., Schmitz, D., Empson, R., and Heinemann, U. (1997). Frequency-dependent information flow from the entorhinal cortex to the hippocampus. *J Neurophysiol*, 78:3444–3449.

Goldman, M. S., Golowasch, J., Marder, E., and Abbott, L. F. (2001). Global structure, robustness, and modulation of neuronal models. *J Neurosci*, 21(14):5229–38.

Golomb, D. and Amitai, Y. (1997). Propagating neuronal discharges in neocortical slices: computational and experimental study. *J Neurophysiol*, 78:1199–1211.

Gray, C. M., Konig, P., Engel, A. K., and Singer, W. (1989). Oscillatory responses in cat visual cortex exhibit inter-columnar synchronization which reflects global stimulus properties. *Nature*, 338:334–337.

Gutfreund, Y., Yarom, Y., and Segev, I. (1995). Subthreshold ocsillations and resonant frequency in guinea pig cortical neurons – physiology and modeling. *J Physiol London*, 483(3):621–40.

Gutkin, B., Ermentrout, G., and Rudolph, M. (2003). Spike generating dynamics and the conditions for spike-time precision in cortical neurons. *J Comput Neurosci*, 15:91–103.

Haas, J. S. and White, J. A. (2002). Frequency selectivity of layer II stellate cells in the medial entorhinal cortex. *J Neurophys*, 88:2422–9.

Hansel, D., Mato, G., and Meunier, C. (1995). Synchrony in excitatory neural networks. *Neural Comput*, 7:307–337.

Hasselmo, M. E., Fransen, E., Dickson, C., and Alonso, A. A. (2000). Computational modelling of entorhinal cortex. *Ann NY Acad Sci*, 911:418–446.

Heinemann, U., Schmitz, D., Eder, C., and Gloveli, T. (2000). Properties of entorhinal cortex projection cells to the hippocampal formation. *Ann N Y Acad Sci*, 911:112–126.

Hetka, R., Rundfeldt, C., Heinemann, U., and Schmitz, D. (1999). Retigabine strongly reduces repetitive firing in rat entorhinal cortex. *Eur J Pharmacol*, 386:165–171.

Hille, B. (2001). *Ion channels of excitable membranes.* Sinauer Associates Inc., Sunderland, Massachusetts USA, 3rd edition.

Hines, M. (1993). Neuron – a program for simulation of nerve equations. *In: Neural Systems: Analysis and Modeling, edited by F. Eeckman. Norwell, MA: Kluwer*, pages 127–36.

Hodgkin, A. (1948). The local electric changes associated with repetitive action in a non-medullated axon. *J Physiol*, 107:165–181.

Hodgkin, A. and Huxley, A. (1952). A quantitative description of membrane current and its application to conduction and excitation in nerve. *J Physiol*, 117:500–544.

Horikawa, K. and Armstrong, W. (1988). A versatile means of intracellular labeling: injection of biocytin and its detection with avidin conjugates. *J Neurosci Methods*, 25:1–11.

Hu, H., Vervaeke, K., and Storm, J. (2002). Two forms of electrical resonance at theta frequencies, generated by M-current, h-current and persistent Na^+ current in rat hippocampal pyramidal cells. *J Physiol*, 545:783–805.

Hudspeth, A. J. and Lewis, R. S. (1988). A model for electrical resonance and frequency tuning in saccular hair cells of the bull-frog, rana catesbeiana. *J. Physiol.*, 400:275–97.

Hunter, J. D. and Milton, G. (2003). Amplitude and frequency dependence of spike timing: implications for dynamic regulation. *J Neurophysiol*, 90:387–394.

Hunter, J. D., Milton, J. G., Thomas, P. J., and Cowan, J. D. (1998). Resonance effect for neural spike time reliability. *J. Neurophysiol.*, 80:1427–1438.

Hutcheon, B., Miura, R., and Puil, E. (1996a). Models of subthreshold membrane resonance in neocortical neurons. *J Neurophysiol*, 76:698–714.

Hutcheon, B., Miura, R., and Puil, E. (1996b). Subthreshold membrane resonance in neocortical neurons. *J Neurophysiol*, 76:683–697.

Hutcheon, B., Miura, R. M., Yarom, Y., and Puil, E. (1994). Low-threshold calcium current and resonance in thalamic neurons: a model of frequency-preference. *J Neurophysiol*, 71:583–594.

Hutcheon, B. and Yarom, Y. (2000). Resonance, oscillation and the intrinsic frequency preferences of neurons. *TINS*, 23 (5):216–22.

Ikegaya, Y., Aaron, G., Cossart, R., Aronov, D., Lampl, I., Ferster, D., and Yuste, R. (2004). Synfire chains and cortical songs: Temporal modules of cortical activity. *Science*, 304:559–564.

Izhikevich, E. (2001). Resonate-and-fire neurons. *Neural Netw*, 14:883–894.

Izhikevich, E. M. (2000). Neural excitability, spiking and bursting. *International Journal of Bifurcation and Chaos*, 10:1171–1266.

Jaeger, D. and Bower, J. M. (1999). Synaptic control of spiking in cerebellar purkinje cells: dynamic current clamp based on model conductances. *J Neurosci*, 19(14):6090–101.

Jansen, H. and Karnup, S. (1994). A spectral analysis of the integration of artificial synaptic potentials in mammalian central neurons. *Brain Res*, 666:9–20.

Jensen, R. V. (1998). Synchronization of randomly driven nonlinear oscillators. *Phys Rev E*, 58:6907–6910.

Jentsch, T. J. (2000). Neuronal KCNQ potassium channels: physiology and role in disease. *Nature Rev Neurosci*, 1:21–30.

Kamondi, A., Acsady, L., Wang, X. J., and Buzsaki, G. (1998). Theta oscillations in somata and dendrites of hippocampal pyramidal cells in vivo: Activity-dependent phase-precession of action potentials. *Hippocampus*, 8:244–261.

Kandel, E. R., Schwartz, J. H., and Jessel, T. M., editors (2000). *Principles of neural science.* McGraw-Hill, 4 edition.

Keener, J., Hoppensteadt, F., and Rinzel, J. (1981). Integrate-and-fire models of nerve membrane response to oscillatory input. *SIAM J. Appl. Math.*, 41:503–517.

Knight, B. W. (1972). The relationship between the firing rate of a single neuron and the level of activity in a population of neurons. Experimental evidence for resonant enhancement in the population response. *J. Gen. Physiol.*, 59:767–778.

Koch, C. (1999). *Biophysics of computation: information processing in single neurons.* Oxford University Press, New York, Oxford.

Kreiman, G., Krahe, R., Metzner, W., Koch, C., and Gabbiani, F. (2000). Robustness and variability of neuronal coding by amplitude-sensitive afferents in the weakly electric fish Eigenmannia. *J Neurophysiol*, 84:189–204.

Kretzberg, J., Warzecha, A.-K., and Egelhaaf, M. (2001). Neural coding with graded membrane potential changes and spikes. *J. Computat. Neurosci.*, 11:153–164.

Lampl, I. and Yarom, Y. (1997). Subthreshold oscillations and resonant behavior: two manifestations of the same mechanism. *Neuroscience*, 78:325–341.

Lestienne, R. (2001). Spike timing, synchronization and information processing on the sensory side of the central nervous system. *Prog Neurobiol*, 65:545–591.

Leung, L. and Yu, H. (1998). Theta-frequency resonance in hippocampal CA1 neurons in vitro demonstrated by sinusoidal current injection. *J Neurophysiol*, 79:1592–1596.

Maccaferri, G. and Dingledine, R. (2002). Control of feedforward dendritic inhibition by NMDA receptor-dependent spike timing in hippocampal interneurons. *J Neurosci*, 22:5462–5472.

Machens, C. K., Schutze, H., Franz, A., Kolesnikova, O., Stemmler, M. B., Ronacher, B., and Herz, A. V. M. (2003). Single auditory neurons rapidly discriminate conspecific communication signals. *Nat Neurosci*, 6:341–342.

Machens, C. K., Stemmler, M. B., Prinz, P., Krahe, R., Ronacher, B., and Herz, A. V. M. (2001). Representation of acoustic communication signals in insect auditory receptors. *J Neurosci*, 21:3215–3227.

Magee, J. C. (2002). A prominent role for intrinsic neuronal properties in temporal coding. *TINS*, 26(1):14–16.

Main, M. J., Cryan, J. E., Dupere, J. R. B., Cox, B., Clare, J. J., and Burbidge, S. A. (2000). Modulation of KCNQ2/3 potassium channels by the novel anticonvulsant retigabine. *Mol Pharmacol*, 58:253–262.

Mainen, Z. and Sejnowski, T. (1995). Reliability of spike timing in neocortical neurons. *Science*, 168:1503–1506.

Manwani, A. and Koch, C. (1999). Detecting and estimating signals in noisy cable structure, I: neuronal noise sources. *Neural Comput.*, 11(8):1797–829.

Manwani, A., Steinmetz, P. N., and Koch, C. (2002). The impact of spike timing variability on the signal-encoding performance of neural spiking models. *Neural Comput*, 14:347–367.

Marder, E., Abbott, L. F., Turrigiano, G. G., Liu, Z., and Golowasch, J. (1996). Memory from the dynamics of intrinsic membrane currents. *Proc Natl Acad Sci USA*, 93(24):13481–6.

Markram, H., Lubke, J., Frotscher, M., and Sakmann, B. (1997). Regulation of synaptic efficacy by coincidence of postsynaptic APs and EPSPs. *Science*, 275:178–179.

Mauro, A., Conti, F., Dodge, F., and Schor, R. (1970). Subthreshold behavior and phenomenological impedance of squid giant axon. *J Gen Physiol*, 55(4):497–523.

McCormick, D., Connors, B., Lighthall, J., and DA, P. (1985). Comparative electrophysiology of pyramidal and sparsely stellate neurons of the neocortex. *J Neurophysiol*, 54:782–805.

Mehta, M. R., Lee, A. K., and Wilson, M. A. (2002). Role of experience and oscillations in transforming a rate code into a temporal code. *Nature*, 417(6):741–746.

Moore, L. E. and Christensen, B. N. (1985). White noise analysis of cable properties of neuroblastoma cells and lamprey central neurons. *J Neurophysiol*, 53:636–651.

Morris, D. and Lecar, H. (1981). Voltage oscillations in the barnacle giant muscle fiber. *Biophys J*, 193:193–213.

Néda, Z., Ravasz, E., Brechet, Y., Vicsek, T., and Barabási, A.-L. (2000). Self-organizing processes: The sound of many hands clapping. *Nature*, 403:849–850.

Nelson, P. and Lux, H. (1970). Some electrical measurements of motoneuron parameters. *Biophys J*, 10:55–73.

Nowak, L. G., Sanchez-Vives, M. V., and McCormick, D. A. (1997). Influence of low and high frequency inputs on spike timing in visual cortical neurons. *Cerebral Cortex*, 7:487–501.

O'Keefe, J. and Nadel, L. (1978). *The hippocampus as a cognitive map.* Clarendon Press, Oxford.

Pape, H.-C. and Driesang, R. B. (1998). Ionic mechanisms of intrinsic oscillations in neurons of the basolateral amygdaloid complex. *J Neurophysiol*, 79:217–226.

Pei, X., Wilkens, L., and Moss, F. (1996). Noise-mediated spike timing precision from aperiodic stimuli in an array of Hodgkin-Huxley-type neurons. *Phys Rev Lett*, 77:4679–4682.

Pfeuty, B., Mato, G., Golomb, D., and Hansel, D. (2003). Electrical synapses and synchrony: The role of intrinsic currents. *J Neurosci*, 23(15):6280–94.

Pike, F., Goddard, R., Suckling, J., Ganter, P., Kasthuri, N., and Paulsen, O. (2000). Distinct frequency preferences of different types of rat hippocampal neurones in response to oscillatory input currents. *J Physiol*, 529:205–213.

Puil, E., Gimbarzevsky, B., and Miura, R. M. (1986). Quantification of membrane properties of trigeminal root ganglion neurons in guinea pig. *J. Neurophysiol.*, 55:995–1016.

Puil, E., Gimbarzevsky, B., and Spigelman, I. (1988). Primary involvement of K^+ conductance in membrane resonance of trigeminal root ganglion neurons. *J. Neurophysiol.*, 59(1):77–89.

Puil, E., Meiri, H., and Yarom, Y. (1994). Resonant behavior and frequency preferences of thalamic neurons. *J Neurophysiol*, 71:575–582.

Reich, D. S., Victor, J. D., Knight, B. W., Ozaki, T., and Kaplan, E. (1997). Response variability and timing precision of neuronal spike trains in vivo. *J Neurophysiol*, 77:2836–2841.

Reinagel, P. and Reid, R. C. (2000). Temporal coding of visual information in the thalamus. *J. Neurosci.*, 20:5392–5400.

Reinagel, P. and Reid, R. C. (2002). Precise firing events are conserved across neurons. *J. Neurosci.*, 22(16):6837–6841.

Rescigno, A., Stein, R., Purple, R., and Poppele, R. (1970). A neuronal model for the discharge patterns produced by cyclic inputs. *Bull. Math. Biophys.*, 32:337–353.

Richardson, M. J., Brunel, N., and Hakim, V. (2003). From subthreshold to firing-rate resonance. *J Neurophysiol*, 89:2538–2554.

Richter, H., Heinemann, U., and Eder, C. (2000). Hyperpolarization-activated cation currents in stellate and pyramidal neurons of rat entorhinal cortex. *Neurosci Lett*, 281:33–36.

Rieke, F., Warland, D., de Ruyter van Steveninck, R. R., and W, B. (1997). *Spikes: Exploring the neural code.* MIT Press, Cambridge (Massachusetts).

Rinzel, J. and Ermentrout, B. (1998). *Analysis of neural excitability and oscillations*, pages 251–292. In: Methods in neural modeling. MIT Press.

Rundfeldt, C. and Netzer, R. (2000). The novel anticonvulsant retigabine activates m-currents in chinese hamster ovary-cells tranfected with human KCNQ2/3 subunits. *Neurosci Lett*, 282:73–76.

Saganich, M. J., Machado, E., and Rudy, B. (2001). Differential expression of genes encoding subthreshold-operating voltage-gated K^+ channels in brain. *J Neurosci*, 21(3):4609–24.

Salinas, E. and Abbott, L. (1994). Vector reconstruction from firing rates. *J Comput Neurosci*, 1:89–107.

Schmitz, D., Gloveli, T., Behr, J., Dugladze, T., and Heinemann, U. (1998). Subthreshold membrane potential oscillations in neurons of deep layers of the entorhinal cortex. *Neuroscience*, 85(4):999–1004.

Schneidman, E., Freedman, B., and Segev, I. (1998). Ion channel stochasticity may be critical in determining the reliability and precision of spike timing. *Neural Comput.*, 10:1679–1704.

Schreiber, S., Erchova, I., Heinemann, U., and Herz, A. V. M. (2004a). Subthreshold resonance explains the frequency-dependent integration of periodic as well as random stimuli in the entorhinal cortex. *J Neurophys, Article in Press:* 10.1152/jn.01116.2003.

Schreiber, S., Fellous, J.-M., Tiesinga, P. H. E., and Sejnowski, T. J. (2004b). Influence of ionic conductances on spike timing reliability of cortical neurons for suprathreshold rhythmic inputs. *J Neurophys*, 91:194–205.

Schreiber, S., Fellous, J.-M., Whitmer, D., Tiesinga, P. H. E., and Sejnowski, T. J. (2003). A new correlation-based measure of spike timing reliability. *Neurocomputing*, 52-4:925–931.

Schreiber, S., Machens, C. K., Herz, A. V. M., and Laughlin, S. B. (2002). Energy efficient coding with discrete stochastic events. *Neural Comput*, 14(6):1323–46.

Shadlen, M. N. and Newsome, W. T. (1994). Noise, neural codes and cortical organization. *Curr Opin Neurobiol*, 4:569–579.

Sharp, A. A., O'Neil, M. B., Abbott, L. F., and Marder, E. (1993). Dynamic clamp: computer-generated conductances in real neurons. *J Neurophysiol*, 69(3):992–5.

Softky, W. R. and Koch, C. (1993). The highly irregular firing of cortical cells is inconsistent with temporal integration of random EPSPs. *J Neurosci*, 13:334–350.

Spain, W., Schwindt, P., and Crill, W. (1987). Anomalous rectification in neurons from cat sensorimotor cortex in vitro. *J Neurophysiol*, 57:1555–1576.

Steriade, M. (2003). The corticothalamic system in sleep. *Front Biosci*, 8:D878–D899.

Storm, J. F. (1990). Potassium currents in hippocampal pyramidal cells. *Prog Brain Res*, 83:161–87.

Strogatz, S. H. (1994). *Nonlinear dynamics and chaos: with applications in physics, biology, chemistry, and engineering.* Perseus Books, Cambridge.

Svirskis, G. and Rinzel, J. (2003). Influence of subthreshold nonlinearities on signal-to-noise ratio and timing precision for small signals in neurons: minimal model analysis. *Network*, 14:137–150.

Tanabe, M., Gahwiler, B. H., and Gerber, U. (1998). L-type Ca^{2+} channels mediate the slow Ca^{2+}-dependent afterhyperpolarization current in rat CA3 pyramidal cells in vitro. *J Neurophysiol*, 80(5):2268–73.

Theunissen, F. and Miller, J. P. (1995). Temporal encoding in nervous systems: a rigorous definition. *J Comput Neurosci*, 2:149–162.

Tiesinga, P. H. E. (2002). Precision and reliability of periodically and quasiperiodically driven integrate-and-fire neurons. *Phys Rev E*, 65:041913.

Tiesinga, P. H. E., Fellous, J.-M., and Sejnowski, T. J. (2002). Attractor reliability reveals deterministic structure in neuronal spike trains. *Neural Comput*, 14:1629–1650.

Turrigiano, G., Abbott, L. F., and Marder, E. (1994). Activity-dependent changes in the intrinsic properties of cultured neurons. *Science*, 264(5161):974–7.

Van Rossum, M. C. (2001). The transient precision of integrate and fire neurons: effect of background activity and noise. *J Comput Neurosci*, 10:303–311.

Vanderwolf, C. H. (1969). Hippocampal electrical activity and voluntary movement in the rat. *Electroencephalogr Clin Neurophysiol*, 26:407–418.

Victor, J. and Purpura, K. (1996). Nature and precision of temporal coding in visual cortex: A metric-space analysis. *J. Neurophysiol.*, 76(2):1310–1326.

Warzecha, A.-K., Kretzberg, J., and Egelhaaf, M. (1998). Temporal precision of the encoding of motion information by visual interneurons. *Curr Biol*, 8:359–368.

Wehr, M. and Laurent, G. (1996). Odour encoding by temporal sequences of firing in oscillating neural assemblies. *Nature*, 384:162–166.

Wehr, M. and Zador, A. M. (2003). Balanced inhibition underlies tuning and sharpens spike timing in auditory cortex. *Nature*, 426:442–446.

White, J. A., Budde, T., and Kay, A. R. (1995). A bifurcation analysis of neuronal subthreshold oscillations. *Biophys J*, 69:1203–1217.

White, J. A., Klink, R., Alonso, A., and Kay, A. R. (1998). Noise from voltage-gated ion channels may influence neuronal dynamics in the entorhinal cortex. *J Neurophysiol*, 80:262–269.

Yamada, Y., Nakazato, Y., and Ohga, A. (1989). Ouabain distinguishes between nicotinic and muscarinic receptor-mediated catecholamine secretions in perfused adrenal-glands of cat. *Brit J Pharmacol*, 96(2):470–9.

Deutschsprachige Zusammenfassung

Netzwerke von Neuronen in unserem Gehirn nehmen fortlaufend Informationen verschiedener Sinnesmodalitäten aus der Umgebung auf, leiten diese Informationen weiter, verarbeiten sie und bestimmen so schließlich unser Verhalten. Die makroskopischen Eigenschaften dieser Netzwerke, wie die Beschaffenheit und Anzahl der Verbindungen zwischen den Neuronen und zwischen verschiedenen Netzwerken, sind wichtig, um eine optimale Verarbeitung und Speicherung der Informationen zu ermöglichen. Grundlegend für die Funktionsweise der Netzwerke sind jedoch auch der Aufbau und die Funktionsweise einzelner Neuronen. So wird zum Beispiel die Fähigkeit eines neuronalen Netzwerkes sich zu synchronisieren, die sich in den im Elektro-Enzephalogramm (EEG) detektierbaren Rhythmen widerspiegelt, auch von den Eigenschaften einzelner Neuronen beeinflusst. Dies wurde durch erste Studien belegt, die einen Zusammenhang zwischen den biophysikalischen Eigenschaften einzelner Zellen und dem Synchronisierungs-Zustand des Gesamtnetzwerks herstellen (Pfeuty et al., 2003; Acker et al., 2003).

Von besonderer Bedeutung für die Signalverarbeitung sind die Eigenschaften einzelner Zellen im Hinblick auf die Frequenz-Selektivität der Signalverarbeitung und die Robustheit neuronaler Antworten gegenüber neuronalem Rauschen. Frequenz-Selektivität beschreibt, wie die unterschiedlichen Komponenten der Spannungsantwort – zum Beispiel ihre Amplitude – von der Frequenz des Eingangssignales abhängen. Die Robustheit neuronaler Antworten wird dadurch charakterisiert, wie reproduzierbar eine Spannungsantwort bei wiederholter Präsentation eines Stimulus ist. Dabei kann die Zuverlässigkeit der Spannungsantwort dadurch herabgesetzt sein, dass nicht bei jeder Präsentation des Stimulus alle Aktionspotentiale auftreten, oder aber dadurch, dass die zeitliche Präzision der Aktionspotentiale vermindert ist.[2] Experimentelle Studien belegen, dass die Zuverlässigkeit der Aktionspotentiale stark vom Zelltyp abhängt. Der Grad der Zuverlässigkeit wird dabei zum einen durch die Größe des neuronalen Rauschens bestimmt, welches zum Beispiel durch die stochastische Ausschüttung von Vesikeln in der synaptischen Übertragung hervorgerufen wird. Zum anderen sind es die intrinsischen biochemischen und biophysikalischen Eigenschaften der Zellen, die einen großen Einfluss auf die zeitliche Präzision haben. Die Mechanismen, welche die Frequenz-Selektivität und die Zuverlässigkeit von Aktionspotentialen auf der Ebene einzelner Zellen bestimmen, sind zentraler Gegenstand der vorliegenden Arbeit. Besondere Aufmerksamkeit gilt der Frage, wie einzelne Neurone, zum Beispiel durch eine Regulation der Zusammensetzung der Ionenkanäle in ihrer Membran, diese Mechanismen modulieren können, um die Signalübertragung zu optimieren.

Die Untersuchungen basieren auf Simulationen und werden auf der Grundlage von leitfähigkeits-basierten Modellneuronen mit unterschiedlicher Ionenkanal-Ausstattung durchgeführt.

---

[2]In der vorliegenden Arbeit werden beide Erscheinungen unter dem Begriff "Spike Timing Reliability" zusammengefasst.

Wie in vielen elektrophysiologischen Studien, werden die Stimuli in Form eines Stromes "injiziert". Es werden sowohl Rauschstimuli als auch sinusförmige Stimuli verschiedener, zum Teil zeitlich veränderlicher Frequenzen verwendet. Das intrinsische Rauschen wird über eine additive Stromkomponente simuliert. Zusätzlich zur theoretischen Analyse der Modellneuronen können Teilergebnisse der Studie auch durch Auswertung von Daten aus dem entorhinalen und präfrontalen Cortex bestätigt werden.[3] Wie im Folgenden beschrieben, gliedert sich die Arbeit in drei Teile.

Im ersten Teil steht die unterschwellige Resonanz als Mechanismus der Frequenz-Selektivität für Signale, die graduierte Spannungsantworten hervorrufen (und daher keine Aktionspotentiale beinhalten), im Vordergrund. Dieses Phänomen wird durch Eigenschaften der neuronalen Membran und der Ionenkanäle hervorgerufen und resultiert für sinusförmige Stimuli in maximalen Antwort-Amplituden bei einer bevorzugen Stimulus-Frequenz. In Kapitel 2 und 3 zeigen wir, dass diese Frequenz-Selektivität, die auf der Grundlage der Antworten zu periodischen Stimuli beschrieben wird, auf nicht-periodische Stimuli übertragbar ist. Sowohl die experimentellen als auch die theoretischen Ergebnisse widerlegen damit die Hypothese aus einer vorhergehenden Studie (Haas and White, 2002), welche nahelegte, dass sich die Integration nicht-periodischer Stimuli nicht auf der Grundlage der unterschwelligen Resonanz erklären lässt. Wir zeigen ferner, dass sich die Frequenz-Selektivität der graduierten Signale auch auf neuronale Antworten mit Aktionspotentialen auswirkt. Damit gibt es Grund zur Annahme, dass unterschwellige Resonanzen gezielt zur frequenz-abhängigen Steuerung des Informationsflusses genutzt werden, wie es von Gloveli *et al.* (1997) vorgeschlagen wurde.

Der zweite Teil der Arbeit beschäftigt sich mit den Mechanismen, die zu einer Abhängigkeit der Zuverlässigkeit von Aktionspotentialen von der Stimulus-Frequenz führen. Unsere Untersuchungen ergeben, dass zwei Stimulus-Bereiche klar unterschieden werden müssen: Stimuli, deren Mittelwerte unterhalb der Feuerschwelle liegen, und Stimuli, deren Mittelwerte oberhalb der Feuerschwelle liegen. In Kapitel 4 belegen wir, dass im ersten Fall der Mechanismus der unterschwelligen Resonanz nicht nur in einer bevorzugten Stimulus-Frequenz mit maximaler Antwortamplitude resultiert, sondern dass bei dieser bevorzugten Frequenz auch die Zuverlässigkeit von Aktionspotentialen am größten ist. Wir diskutieren den Einfluss von Nichtlinearitäten, die bei größeren Stimulus-Amplituden auftreten, ebenso wie die Abhängigkeit der Zuverlässigkeit vom Mittelwert des Stimulus.

Für Eingangssignale, deren Mittelwert oberhalb der Feuerschwelle liegt, wurde bereits 1998 von Hunter *et al.* ein Resonanz-Effekt vorgeschlagen, der die Frequenz-Abhängigkeit der Zuverlässigkeit von Aktionspotentialen bestimmt. Hunter *et al.* zeigten anhand von elektrophysiologischen Ableitungen der Neuronen der Meeresschnecke Aplysia, dass die mittlere Feuerrate die Stimulus-Frequenz bestimmt, bei der die Aktionspotentiale am zuverlässigsten sind. Diesen Effekt können wir in Kapitel 5 und 6 für leitfähigkeits-basierte Modellneurone bestätigen. Zusätzlich identifizieren wir für dieses Stimulus-Regime Ionenkanäle, bei denen die Änderung der Gesamtleitfähigkeit in einer Modulation der bevorzugten Frequenz resultiert. Als Ergebnis der Untersuchung kann festgehalten werden, dass die bevorzugte Frequenz besonders effizient durch Veränderungen in der Gesamtleitfähigkeit der Kaliumkanäle mit langsamer Kinetik moduliert werden kann. Dies ist besonders im Hinblick auf die Tatsache interessant, dass zahlreiche

---

[3]Für die Durchführung der experimentellen Untersuchungen danke ich Irina Erchova (Humboldt-Universität zu Berlin/Charité) und Jean-Marc Fellous (The Salk Institute, USA).

Neuromodulatoren bekannt sind, die diese Ionenkanäle in ihrer Funktionsweise beeinflussen. Damit eröffnet sich die Möglichkeit der dynamischen Regulation der Zuverlässigkeit neuronaler Antworten.

Es ist jedoch wichtig zu erkennen, dass Änderungen der Zuverlässigkeit, wenn sie auf dem Resonanz-Effekt beruhen, immer auch an eine Änderung der mittleren Feuerrate gekoppelt sind. Dass jedoch eine Regulierung der Zuverlässigkeit auch ohne Veränderung der mittleren Feuerrate möglich ist, wird im dritten Teil der Arbeit demonstriert. Wir beschreiben in Kapitel 7 erstmals die Möglichkeit, mittels bestimmter Ionenkanäle die Robustheit der neuronalen Antworten gegenüber Rauschen zu erhöhen. Die Modifikation der Gesamtleitfähigkeit von langsamen Kaliumkanälen oder ihrer Kinetik sowie die Modifikation der Gesamtleitfähigkeit von persistenten Natriumkanälen beeinflusst direkt die Auswirkungen von Rauschen auf die Zuverlässigkeit.

Insgesamt zeigt diese Arbeit, wie die Dynamik der einzelnen Zellen durch die zell-intrinsischen Eigenschaften, insbesondere die Zusammensetzung der Leitfähigkeiten in der neuronalen Membran, bestimmt wird. Wir identifizieren Mechanismen, die die Frequenz-Selektivität und die Zuverlässigkeit von neuronalen Antworten beeinflussen. Gleichzeitig belegen wir, dass diese Mechanismen dynamisch durch Veränderung der Zusammensetzung der neuronalen Leitfahigkeiten, zum Beispiel über Neuromodulatoren, angepasst werden können. Die vorliegende Untersuchung beschränkt sich auf einzelne Neurone; das Verständnis der Signalverarbeitung in einzelnen Zellen erlaubt jedoch auch Rückschlüsse auf die Dynamik von Netzwerken.

Veröffentlichungen

Artikel in Fachzeitschriften

S. Schreiber, I. Erchova, U. Heinemann, A.V.M. Herz, (2004): Subthreshold resonance explains the frequency-dependent integration of periodic as well as random stimuli in the entorhinal cortex. J Neurophysiol. *Articles in Press:* 10.1152/jn.01116.2003.

S. Schreiber, J.-M. Fellous, P.H.E. Tiesinga, T.J. Sejnowski, (2004): Influence of ionic conductances on spike timing reliability of cortical neurons for suprathreshold rhythmic inputs. J. Neurophysiol. 91: 194-205.

S. Schreiber, J.-M. Fellous, D. Whitmer, P.H.E. Tiesinga, T.J. Sejnowski, (2003): A new correlation-based measure of spike timing reliability. Neurocomputing, 52-54:925-931.

S. Schreiber, C.K. Machens, A.V.M. Herz, and S.B. Laughlin, (2002). Energy-efficient coding with discrete stochastic events. Neural Comput. 14(6):1323-46.

K. John, S. Schreiber, J. Kubelt, A. Herrmann, and P. Mueller (2002): Transbilayer movement of phospholipids at the main phase transition of lipid membranes: Implications for rapid flip-flop in biological membranes. Biophys J, 83(6):3315-3323.

S. Schreiber, K. Ludwig, A. Herrmann, and H.-G. Holzhütter, (2001): Stochastic simulation of hemagglutinin-mediated fusion pore formation. Biophys J., 81(3):1360-72.

Buchkapitel

S. Schreiber, K. Ludwig, H.-G. Holzhütter, A. Herrmann: Stochastic model of influenza virus fusion. *In: Function and regulation of cellular systems: Experiments and models. Birkhäuser, 2003.*

Selbständigkeitserklärung

Hiermit erkläre ich, die vorliegende Arbeit selbständig ohne fremde Hilfe verfaßt und nur die angegebene Literatur und Hilfsmittel verwendet zu haben.

Susanne Schreiber   14. Mai 2004